Applied Computational Electromagnetics Society

Journal

January 2011 Vol. 26 No. 1

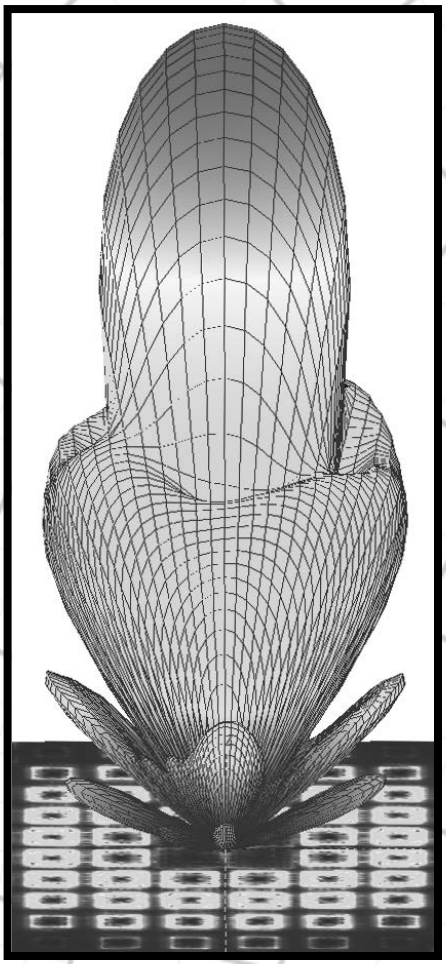

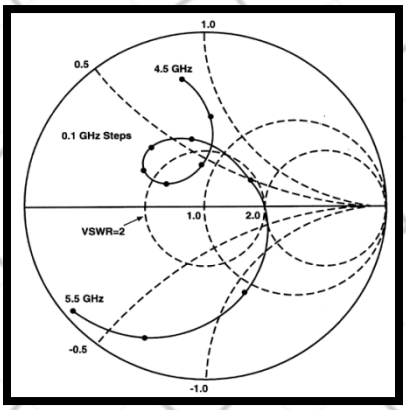

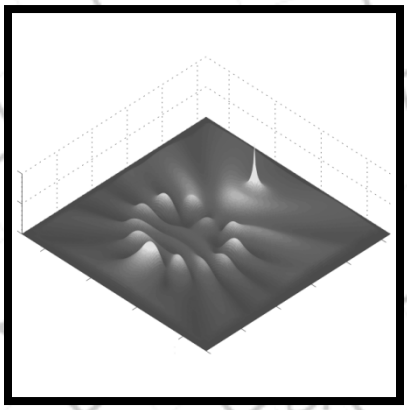

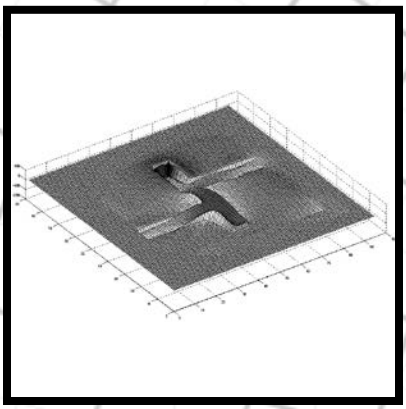

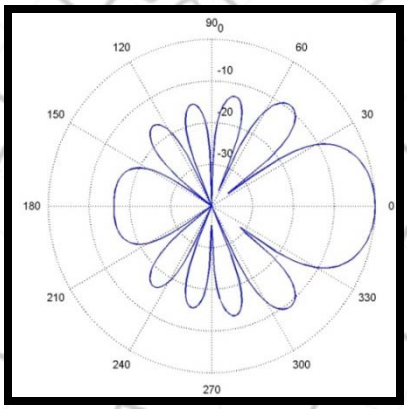

ISSN 1054-4887

GENERAL PURPOSE AND SCOPE: The Applied Computational Electromagnetics Society ***(ACES)*** Journal hereinafter known as the ***ACES Journal*** is devoted to the exchange of information in computational electromagnetics, to the advancement of the state-of-the art, and the promotion of related technical activities. The primary objective of the information exchange is to inform the scientific community on the developments of new computational electromagnetics tools and their use in electrical engineering, physics, or related areas. The technical activities promoted by this publication include code validation, performance analysis, and input/output standardization; code or technique optimization and error minimization; innovations in solution technique or in data input/output; identification of new applications for electromagnetics modeling codes and techniques; integration of computational electromagnetics techniques with new computer architectures; and correlation of computational parameters with physical mechanisms.

SUBMISSIONS: The ***ACES Journal*** welcomes original, previously unpublished papers, relating to applied computational electromagnetics. Typical papers will represent the computational electromagnetics aspects of research in electrical engineering, physics, or related disciplines. However, papers which represent research in applied computational electromagnetics itself are equally acceptable.

Manuscripts are to be submitted through the upload system of ***ACES*** web site http://aces.ee.olemiss.edu See "Information for Authors" on inside of back cover and at ***ACES*** web site. For additional information contact the Editor-in-Chief:

Dr. Atef Elsherbeni
Department of Electrical Engineering
The University of Mississippi
University, MS 386377 USA
Phone: 662-915-5382
Email: atef@olemiss.edu

SUBSCRIPTIONS: All members of the Applied Computational Electromagnetics Society are entitled to access and download the ***ACES Journal*** any published journal article available at http://aces.ee.olemiss.edu. Printed issues of the ***ACES Journal*** are delivered to institutional members. Each author of published papers receives a printed issue of the ***ACES Journal*** in which the paper is published.

Back issues, when available, are $50 each. Subscription to ***ACES*** is through the web site. Orders for back issues of the ***ACES Journal*** and change of address requests should be sent directly to ***ACES*** office at:

Department of Electrical Engineering
The University of Mississippi
University, MS 386377 USA
Phone: 662-915-7231
Email: aglisson@olemiss.edu

Allow four weeks advance notice for change of address. Claims for missing issues will not be honored because of insufficient notice, or address change, or loss in the mail unless the ***ACES*** office is notified within 60 days for USA and Canadian subscribers, or 90 days for subscribers in other countries, from the last day of the month of publication. For information regarding reprints of individual papers or other materials, see "Information for Authors".

LIABILITY. Neither ***ACES***, nor the ***ACES Journal*** editors, are responsible for any consequence of misinformation or claims, express or implied, in any published material in an ***ACES Journal*** issue. This also applies to advertising, for which only camera-ready copies are accepted. Authors are responsible for information contained in their papers. If any material submitted for publication includes material which has already been published elsewhere, it is the author's responsibility to obtain written permission to reproduce such material.

APPLIED COMPUTATIONAL ELECTROMAGNETICS SOCIETY JOURNAL

January 2011
Vol. 26 No. 1
ISSN 1054-4887

The ACES Journal is abstracted in INSPEC, in Engineering Index, DTIC, Science Citation Index Expanded, the Research Alert, and to Current Contents/Engineering, Computing & Technology.

The illustrations on the front cover have been obtained from the research groups at the Department of Electrical Engineering, The University of Mississippi.

JANUARY 2011 REVIEWERS

Iftikhar Ahmed
Gokhan Apaydin
Mohamed Bakr
Sami Barmada
Gerard Berginc
Deb Chatterjee
William Davis
Khaled ElMahgoub
Mohamed Essaaidi
Dimitra Kaklamani
Nikolaos Kantartzis
Fadi Khalil
Fernando Las-Heras
Xiuping Li
Ricardo Matias
Antonino Musolino
Lorena Lozano Plata
Hassan Ragheb
Vince Rodriguez
Usman Saeed
Christopher Trueman
Korkut Yegin
Theodoros Zygiridis

THE APPLIED COMPUTATIONAL ELECTROMAGNETICS SOCIETY

JOURNAL

Vol. 26 No. 1 January 2011

TABLE OF CONTENTS

A Subgridding Scheme Based on the FDTD Method and HIE-FDTD Method

Juan Chen and Anxue Zhang

School of Electronic and Information Engineering
Xi'an Jiaotong University, Xi'an 710049, China
anxuezhang@mail.xjtu.edu.cn

Abstract- To reduce the computer memory and time of the finite-difference time-domain (FDTD) method when the problems are simulated with fine structural features, the subgridding scheme that applies higher resolution only around critical areas is often used. In this paper, a new subgridding scheme is proposed which is based on the hybrid implicit-explicit finite-difference time-domain (HIE-FDTD) method and FDTD algorithm. The field components in fine local grids are updated using the HIE-FDTD method, and in the coarse main grids conventional FDTD method is utilized. Due to the weakly conditional stability of the HIE-FDTD method, the technique achieves the same time marching step in the whole domain as employed in the coarse FDTD scheme, and the need for the temporal interpolation of the fields in the fine grids is obviated, hence, the hybrid HIE-FDTD subgridding scheme is less time consuming and easy to implement. Practical application of hybrid algorithm in the simulation of the shielding effectiveness of an enclosure is reported.

Index Terms- FDTD method, HIE-FDTD method, subgridding scheme, weakly conditional stability.

I. INTRODUCTION

The finite-difference time-domain (FDTD) method [1] has been proven to be an effective means that provides accurate predictions of field behaviors for varieties of electromagnetic interaction problems. When there exists a fine structural feature compared with other parts in the computational domain, the intuitive approach is to discretize the whole computational domain with a very fine spatial increment in order to achieve enough spatial resolution. This will lead to excessive use of computation resources including computer memory and CPU time.

To circumvent this problem, the subgridding method for local mesh refinement is proposed as an efficient tool to enhance the FDTD algorithm [2-7].The subgridding method uses a fine mesh only in the geometrically critical or electrically small areas and a coarse mesh elsewhere. Inside the fine grid region, the temporal step size must be adjusted to a smaller value in order to meet the stability criterion. Therefore, to synchronize the timing between the two regions, many time steps need to be executed in the fine grid region within a time step of the coarse grid region.

A novel subgridding scheme using the hybrid implicit-explicit finite-difference time-domain (HIE-FDTD) method [8-12] to process the fine grid region is proposed in this article. The HIE-FDTD method is weakly conditionally stable, such the step size in the fine grid region can be set equal to that in the coarse grid region to speed up the computation. Temporal interpolation at the fine and coarse grids interface is no longer necessary. Accuracy of the proposed approach is verified by comparing with FDTD method and HIE-FDTD using a fine spatial increment for the total computational domain, and the memory requirements of all these methods are compared. Practical application of the hybrid subgridding algorithm in the simulation of the shielding effectiveness of an enclosure is reported.

II. THEORY

A. HIE-FDTD method

Without loss of generality, assume that the fine mesh is along the z-direction. Figure 1 shows the interface between the fine and coarse grid regions and the corresponding field components in each region. The ratio between spatial increments in the two regions is denoted by $m = \Delta Z / \Delta Z_f$, where Δz and Δz_f are the spatial increments along the

z-axis in the coarse grid region, and in the fine grid region, respectively. The ratio m is set to 3 as an illustrating example in Figure 1. E_z, E_x, and H_y represent field components in the coarse grid region, and E_{zf}, E_{xf}, and H_{yf} represent field components in the fine grid region.

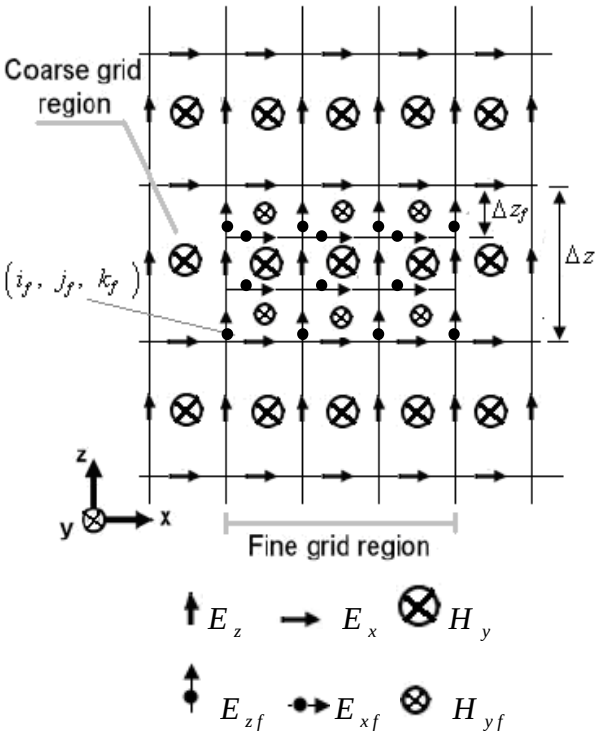

Fig. 1. The field components around the fine and coarse grid interface.

The HIE-FDTD scheme is employed in the fine grid region to update the field components where n and Δt are the index and size of time-step, Δx and Δy are the spatial increments respectively in x- and y-directions, ε and μ are the permittivity and permeability of the surrounding media, respectively. The E_{xf} and H_{yf} components in the HIE-FDTD method are expressed in equations (1) and (2).

Updating of the E_{xf} component, as shown in eq. (1), needs the unknown H_{yf} component at the same time, thus the E_{xf} component has to be updated implicitly. By substituting (2) into (1), the equation for E_{xf} field can be represented by equation (3).

$$
\begin{aligned}
E_{xf}^{n+1}\left(i+\frac{1}{2},j,k\right) &= E_{xf}^{n}\left(i+\frac{1}{2},j,k\right) \\
&+\frac{\Delta t}{\varepsilon\Delta y}H_{zf}^{n+\frac{1}{2}}\left(i+\frac{1}{2},j+\frac{1}{2},k\right) \\
&-\frac{\Delta t}{\varepsilon\Delta y}H_{zf}^{n+\frac{1}{2}}\left(i+\frac{1}{2},j-\frac{1}{2},k\right) \\
&-\frac{\Delta t}{2\varepsilon\Delta z_f}H_{yf}^{n+1}\left(i+\frac{1}{2},j,k+\frac{1}{2}\right) \\
&+\frac{\Delta t}{2\varepsilon\Delta z_f}H_{yf}^{n+1}\left(i+\frac{1}{2},j,k-\frac{1}{2}\right) \\
&-\frac{\Delta t}{2\varepsilon\Delta z_f}H_{yf}^{n}\left(i+\frac{1}{2},j,k+\frac{1}{2}\right) \\
&+\frac{\Delta t}{2\varepsilon\Delta z_f}H_{yf}^{n}\left(i+\frac{1}{2},j,k-\frac{1}{2}\right), \qquad (1)
\end{aligned}
$$

$$
\begin{aligned}
H_{yf}^{n+1}\left(i+\frac{1}{2},j,k+\frac{1}{2}\right) &= H_{yf}^{n}\left(i+\frac{1}{2},j,k+\frac{1}{2}\right) \\
&+E_{zf}^{n+\frac{1}{2}}\left(i+1,\ j,k+\frac{1}{2}\right) \\
&-\frac{\Delta t}{\mu\Delta x}E_{zf}^{n+\frac{1}{2}}\left(i,\ j,k+\frac{1}{2}\right) \\
&-\frac{\Delta t}{2\mu\Delta z_f}E_{xf}^{n+1}\left(i+\frac{1}{2},\ j,k+1\right) \\
&+\frac{\Delta t}{2\mu\Delta z_f}E_{xf}^{n+1}\left(i+\frac{1}{2},\ j,k\right) \\
&-\frac{\Delta t}{2\mu\Delta z_f}E_{xf}^{n}\left(i+\frac{1}{2},\ j,k+1\right) \\
&+\frac{\Delta t}{2\mu\Delta z_f}E_{xf}^{n}\left(i+\frac{1}{2},\ j,k\right), \qquad (2)
\end{aligned}
$$

$$
\left[1+2s_1\right]E_{xf}^{n+1}\left(i+\frac{1}{2},j,k\right)
$$

$$
\begin{aligned}
&-s_1\left[E_{xf}^{n+1}(i+\frac{1}{2},j,k+1)+E_{xf}^{n+1}(i+\frac{1}{2},j,k-1)\right]\\
&=E_{xf}^{n}\left(i+\frac{1}{2},j,k\right)+\frac{\Delta t}{\varepsilon\Delta z_f}H_{yf}^{n}\left(i+\frac{1}{2},j,k+\frac{1}{2}\right)\\
&-\frac{\Delta t}{\varepsilon\Delta z_f}H_{yf}^{n}\left(i+\frac{1}{2},j,k-\frac{1}{2}\right)\\
&-s_2\begin{bmatrix}E_{zf}^{n+\frac{1}{2}}\left(i+1,j,k+\frac{1}{2}\right)-E_{zf}^{n+\frac{1}{2}}\left(i,j,k+\frac{1}{2}\right)\\-E_{zf}^{n+\frac{1}{2}}\left(i+1,j,k-\frac{1}{2}\right)+E_{zf}^{n+\frac{1}{2}}\left(i,j,k-\frac{1}{2}\right)\end{bmatrix}\\
&+s_1\begin{bmatrix}E_{xf}^{n}\left(i+\frac{1}{2},j,k+1\right)-2E_{xf}^{n}\left(i+\frac{1}{2},j,k\right)\\+E_{xf}^{n}\left(i+\frac{1}{2},j,k-1\right)\end{bmatrix}\\
&-\frac{\Delta t}{\varepsilon\Delta y}\begin{bmatrix}H_{zf}^{n+\frac{1}{2}}\left(i+\frac{1}{2},j+\frac{1}{2},k\right)\\-H_{zf}^{n+\frac{1}{2}}\left(i+\frac{1}{2},j-\frac{1}{2},k\right)\end{bmatrix},
\end{aligned}
\tag{3}
$$

where, $s_1=\dfrac{\Delta t^2}{4\varepsilon\mu\Delta z_f{}^2}, s_2=\dfrac{\Delta t^2}{2\mu\varepsilon\Delta x\Delta z_f}$.

The HIE-FDTD method is weakly conditionally stable. The time step size in the HIE-FDTD method is determined as follows:

$$\Delta t \le 1\Big/\left(c\sqrt{\left(1/\Delta x\right)^2+\left(1/\Delta y\right)^2}\right), \tag{4}$$

here, c is the light velocity in the medium.

In the coarse grid region, field components are updated using Yee's FDTD expressions, thus, in the whole domain, the time step size can be set as that in the FDTD scheme, namely,

$$\Delta t \le 1\Big/\left(c\sqrt{\left(1/\Delta x\right)^2+\left(1/\Delta y\right)^2+\left(1/\Delta z\right)^2}\right).$$

Temporal synchronization is then easily achieved, and only spatial interpolation is needed to be taken care of at the interface.

B. Spatial interpolation at the interface

Field components in the fine and coarse grid regions are updated using different schemes. For nodes located near the fine and coarse grid interface, proper care must be taken in order to avoid the discontinuity in fields which will lead to instability of the computation. Suppose the interface is set at $i=i_f$, $j=j_f$, and $k=k_f$, as shown in Figure 1.

In Figure 1, the coarse and fine grid ratio *m* is equal to 3. At the interface $j=j_f$, electric field $E_z\left(i_f+n,j_f,k_f+\frac{1}{2}\right)$ ($0\le n\le 3$)is obtained from E_{zf} at each time step through a simple interpolation as:

$$
\begin{aligned}
&E_z\left(i_f+n,j_f,k_f+\frac{1}{2}\right)\\
&=\frac{\sum_{m=0}^{2}E_{zf}\left(i_f+n,j_f,k_f+m+\frac{1}{2}\right)\Delta z_f\left(k_f+m\right)}{\sum_{m=0}^{2}\Delta z_f\left(k_f+m\right)}\\
&\left(0\le n\le 3\right).
\end{aligned}
\tag{5}
$$

The E_{zf} components at the interfaces $i=i_f$ and $j=j_f$ are calculated as follows:

$$
\begin{aligned}
&E_{zf}^{n+1}\left(i_f,j_f,k_f+m+\frac{1}{2}\right)\\
&=E_{zf}^{n}\left(i_f,j_f,k_f+m+\frac{1}{2}\right)\\
&+\frac{\Delta t}{\varepsilon\Delta x}H_{yf}^{n}\left(i_f+\frac{1}{2},j_f,k_f+m+\frac{1}{2}\right)
\end{aligned}
$$

$$-\frac{\Delta t}{\varepsilon \Delta x} H_y^n\left(i_f-\frac{1}{2}, j_f, k_f+\frac{1}{2}\right)$$
$$-\frac{\Delta t}{\varepsilon \Delta y} H_{xf}^n\left(i_f, j_f+\frac{1}{2}, k_f+m+\frac{1}{2}\right)$$
$$+\frac{\Delta t}{\varepsilon \Delta y} H_x^n\left(i_f, j_f-\frac{1}{2}, k_f+\frac{1}{2}\right)$$
$$\left(0 \le m \le 2\right). \tag{6}$$

Similarly, at the interface $j = j_f$, the magnetic field $H_y\left(i_f+n+\frac{1}{2}, j_f, k_f+\frac{1}{2}\right)$ $(0 \le n \le 2)$ is obtained from H_{yf} at each time step as:

$$H_y\left(i_f+n+\frac{1}{2}, j_f, k_f+\frac{1}{2}\right)$$
$$=\frac{\sum_{m=0}^{2} H_{yf}\left(i_f+n+\frac{1}{2}, j_f, k_f+m+\frac{1}{2}\right)\Delta z_f\left(k_f+m\right)}{\sum_{m=0}^{2}\Delta z_f\left(k_f+m\right)}$$
$$\left(0 \le n \le 2\right). \tag{7}$$

The H_{yf} components are updated by using eq. (2).

The flowchart of the algorithm procedure is shown in Figure 2.

It should be noted that, the scheme above is only suitable to the question with fine mesh along z-direction. If the fine mesh is along y (or/and x)-direction, the scheme can be derived by following the same analysis.

III. SIMULATION RESULTS

To demonstrate the accuracy and efficiency of the proposed subgridding method, a simulation of the shielding effectiveness of an enclosure is employed. The geometric configuration of the enclosure is shown in Figure 3. The length, width, and height of the enclosure are 30 cm, 30 cm, and 12 cm, respectively. A thin slot is cut on the front side of the enclosure. The length and width of the slot are 20 cm and 3 cm. A uniform plane electromagnetic wave, polarized in the $\hat{z}$ direction and traveling along the $\hat{y}$ direction, incident on the aperture. The time dependence of the excitation function is as follows,

$$E_{in}^z(t) = \exp[-\alpha(t-t_0)^2], \tag{8}$$

where α and t_0 are constants. Here, we choose $\alpha = 0.31\times 10^{19}$ s^{-2}, and $t_0 = 2.0\times 10^{-9}$ s. In such a case, the highest frequency of interest is 1 GHz.

To model the slot precisely, a fine mesh must be utilized in the region around the slot, as shown in Figure 4. Here, we choose $\Delta x = \Delta y = 3$ cm., $\Delta z = 2.25$cm, $\Delta z_f = 0.6$cm. To satisfy the stability condition of the FDTD algorithm, the time-step size for the FDTD in the fine grid region is $\Delta t \le 19.24$ ps. To improve the computation efficiency, we utilize the HIE-FDTD method in the fine grid region, thus, the step size in the fine grid region can be set equal to that in the coarse grid region, that is, $\Delta t = 51.45$ ps. Six perfectly matched layers are used to terminate all six sides of the lattice.

Applying the new subgridding scheme to compute the electric field component E_z and the shielding effectiveness (SE) at the central point of the enclosure, the results are shown in Figures 5 and 6. For the sake of comparison, we also present the results at the same position obtained by using the FDTD method and the HIE-FDTD method, respectively. In the FDTD method and the HIE-FDTD method, only the fine space increment is used. The time step sizes in the FDTD, HIE-FDTD, and sungridding schemes are 19.24 ps, 70.71 ps, and 51.45 ps, respectively. It can be seen from Figures 5 and 6 that, the results calculated by using these three methods agree well with each other, which shows that the subgidding scheme has high accuracy.

The computation time and the memory requirements of the FDTD, HIE-FDTD, and subgridding scheme in this simulation are shown in Table 1. Apparently, the proposed subgridding scheme consumes less computer memory and much less computation time compared to the conventional FDTD method and HIE-FDTD method which discretize the whole computation domain with a fine grid.

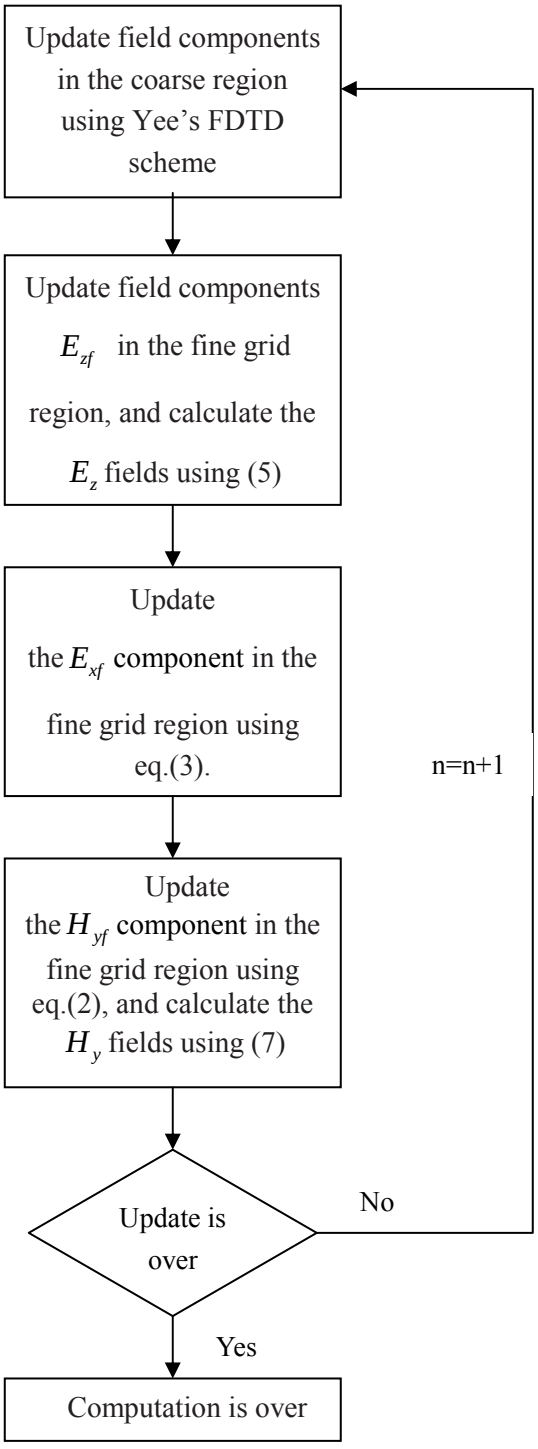

Fig. 2. The flowchart of the subgridding scheme.

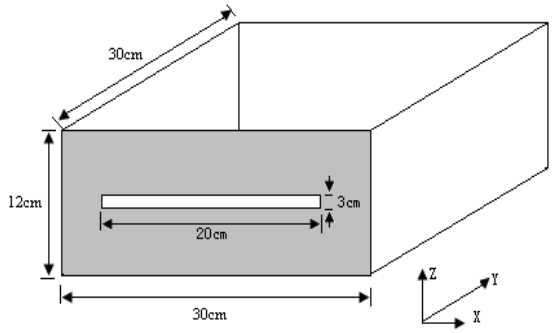

Fig. 3. Geometric configuration of the numerical simulation.

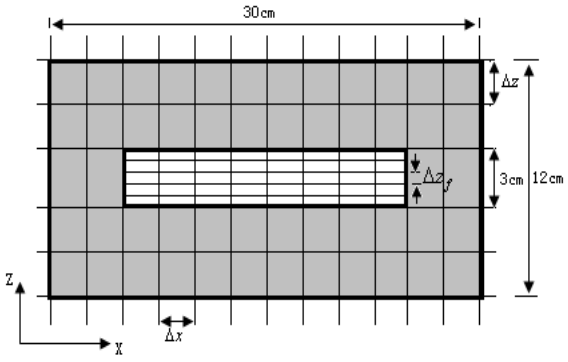

Fig. 4. Spatial increments of the front side of the enclosure.

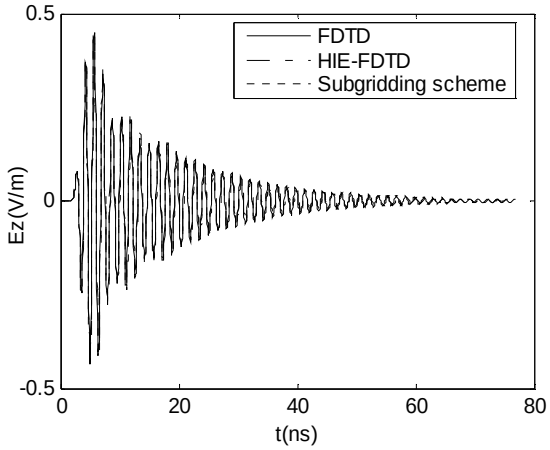

Fig. 5. Comparison of E_z component calculated by different methods.

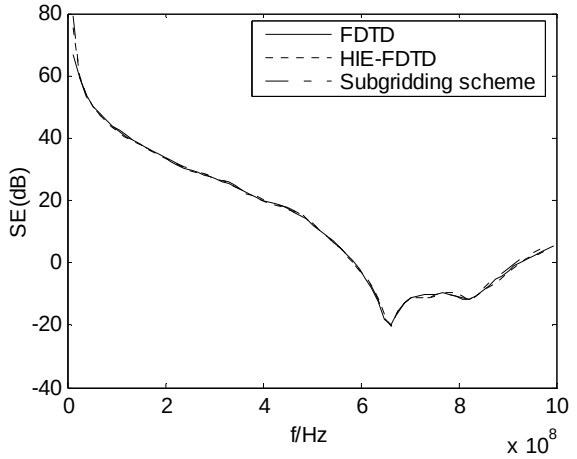

Fig. 6. Comparison of SE calculated by different methods.

Table 1: The computation time and the memory requirements of three methods

Sample	FDTD	HIE-FDTD	Subgridding Scheme
time (s)	1072.92	647.74	353.47
Memory (Mb)	16.85	18.30	15.14

To demonstrate the accuracy of the proposed subgridding method further, the relationship between the relative error and the grid size ratio *m* is shown in Figure 7. For the sake of comparison, the relative error of hybrid alternating direction implicit (ADI)-FDTD subgridding scheme [5] is also shown in this figure. Relative error is defined as,

$$err(\%) = \frac{\sum_{t=0}^{T} \left| E_z^{'}(t) - E_z(t) \right|}{T}, \qquad (9)$$

here, $E_z^{'}(t)$ is the result calculated by the proposed subgridding method or hybrid ADI-FDTD subgridding scheme; $E_z(t)$ is the result calculated by the FDTD method; T is the total time steps.

It can be seen from Figure 7 that, as the increase of the ratio *m*, the errors both of the proposed subgridding method and the hybrid ADI-FDTD subgridding scheme are decreased, and the accuracy of the proposed subgridding method is higher than that of hybrid ADI-FDTD

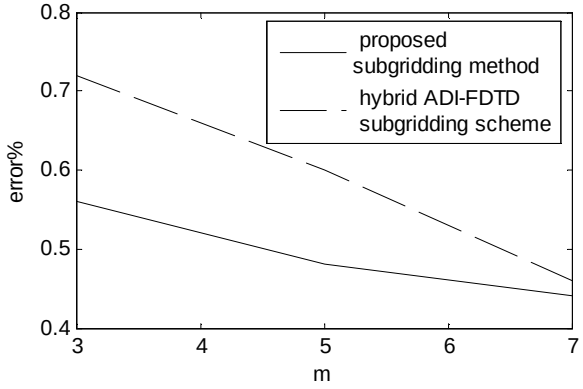

Fig. 7. The relationship between the error and the grid size ratio.

subgridding scheme. It is due to that the accuracy of HIE-FDTD method is over the ADI-FDTD method [9].

IV. CONCLUSION

A novel subgridding scheme combining the HIE-FDTD method and the conventional FDTD method is presented. The HIE-FDTD scheme is used for the subgridding regions and the FDTD scheme is employed for the coarse grid regions. With the weakly conditional stability of the HIE-FDTD algorithm, the subgridding scheme achieves the same time-step size in the entire computational domain. Hence, this technique is very simple to implement and saves considerable simulation time. The hybrid HIE-FDTD subgridding scheme can be used to all those cases where the conventional subgridding FDTD method is applicable, but with less computer memory and much less computation time.

ACKNOWLEDGMENT

This work was supported by the National Natural Science Foundations of China (No. 61001039 and 60501004), and also supported by the Research Fund for the Doctoral Program of Higher Education of China (20090201120030).

REFERENCES

[1] K. S. Yee, "Numerical Solution of Initial Boundary Value Problems Involving Maxwell's Equations in Isotropic Media,"

IEEE Trans. Antennas Propagat., vol. 14, pp. 302-307, May 1966.

[2] D. T. Prescott and N. V. Shuley, "A Method for Incorporating Different Sized Cells Into the Finite-Difference Time-Domain Analysis Technique," *IEEE Microwave Guided Wave Lett.*, vol. 2, pp. 434-436, Nov. 1992.

[3] M. W. Chevalier, R. J. Luebbers, and V. P. Cable, "FDTD Local Grid with Material Traverse," *IEEE Trans. Antennas Propagat*, vol. 45, pp. 411-421, Mar. 1997.

[4] M. Okoniewski, E. Okoniewska, and M. A. Stuchly, "Three-Dimensional Subgridding Algorithm for FDTD," *IEEE Trans. Antennas Propagat.*, vol. 45, pp. 422-429, Mar. 1997.

[5] I. Ahmed and Z. Chen, "A Hybrid ADI-FDTD Subgridding Scheme for Efficient Electromagnetic Computation," *International Journal of Numerical Modeling, Electronic networks, devices and fields*, vol. 17, pp. 237-249, Jan. 2004.

[6] A. Monorchio and R. Mittra, "Time-Domain (FE/FDTD) Technique for Solving Complex Electromagnetic Problems," *IEEEE Microwave Guided Wave Lett*., vol. 8, pp. 93-95, Feb. 1998.

[7] S. Wang, "Numerical Examinations of the Stability of FDTD Subgridding Schemes," *The Applied Computational Electromagnetics Society (ACES) Journal,* vol. 22, pp. 189-194, 2007.

[8] J. Chen and J. Wang, "A 3-D Hybrid Implicit-Explicit FDTD Scheme with Weakly Conditional Stability," *Microwave Opt. Technol. Lett.*, vol. 48, pp. 2291-2294, Nov. 2006.

[9] J. Chen and J. Wang, "Comparison between HIE-FDTD Method and ADI-FDTD Method," *Microwave Opt. Technol. Lett.,* vol. 49, pp. 1001-1005, May 2007.

[10] J. Chen and J. Wang, "A Three-Dimensional Semi-Implicit FDTD Scheme for Calculation of Shielding Effectiveness of Enclosure with Thin Slots," *IEEE Trans. Electromagn. Compat.*, vol. 49, pp. 419-426, Feb. 2007.

[11] I. Ahmed and E. Li, "Conventional Perfectly Matched Layer for Weakly Conditionally Stable Hybrid Implicit and Explicit-FDTD Method," *Microwave Opt. Technol. Lett.,* vol. 49, pp. 3106-3109, Dec. 2007.

[12] J. Chen and J. Wang, "Numerical Simulation using HIE–FDTD Method to Estimate Various Antennas with Fine Scale Structures," *IEEE Trans. Antennas Propagat.*, vol. 55, pp. 3603-3612, Dec. 2007.

Finite Element Analysis of Switched Reluctance Generator under Fault Condition Oriented Towards Diagnosis of Eccentricity Fault

Ebrahim Afjei and Hossein Torkaman

Department of Electrical and Computer Engineering
Shahid Beheshti University, G.C., Tehran, Iran
E-Afjei@sbu.ac.ir; H_Torkaman@sbu.ac.ir

Abstract ─ In this paper, a novel two phase double layer switched reluctance generator (DLSRG) under static eccentricity fault is introduced and analyzed. The proposed generator consists of two magnetically independent stator and rotor layers. There is a stationary reel, which has the field coils wrapped around it and is placed between the two-stator sets. This paper then continues with modeling this generator in the field assisted mode for healthy condition as well as motor with static rotor eccentricity utilizing three-dimensional finite element analysis (3-D FEA). The results of the numerical analysis for a (4/2)×2 DLSRG including flux linkages, mutual inductances per phase in each layer and radial force for various eccentric generator conditions by considering the end effects and axial fringing fields for simulating reliable model are obtained and compared. Consequently, Fourier analysis is carried out to study the variations of mutual inductance as a diagnosis index. The obtained results present useful information as good candidates for fault indicators as well as the amount of eccentricity fault and the direction of fault occurrence.

Index Terms ─ Eccentricity, fault diagnosis, switched reluctance generator (SRG), 3-D finite element method.

I. INTRODUCTION

Switched reluctance generators (SRG) have been gradually engaged in variable-speed applications due to its fundamental advantages of low manufacturing cost, simple and rigid structure, easiness of maintenance, excellent speed regulation, simple converter circuit, no rotor windings or permanent magnet, and easy cooling feature, etc [1-3]. The SRG has been proved as a good alternative for some applications like wind turbine generator, battery charger, and as an alternator for automotive applications [4-6].

On the other side, one of the most common types of fault in electrical machines is the eccentricity fault. Eccentricity exists in a machine when there is an uneven air gap between the stator and the rotor [7, 8]. Static eccentricity is caused by different factors such as, weight of the rotor/load or interconnecting rotor belt. The end result can cause electrically induced vibration that reduces the life of bearings and also increases the potential for stator/ rotor rubbing and damages to the insulation systems.

The effect of eccentricity fault on the torque profile of an SR motor with 2-D FEM has been considered in [9] and the result shows the static torque does not change much with relative eccentricity up to 50%. It is also shown with an increase in the eccentricity; there will be an increase in the fundamental, 8th, 10th, 14th, and 15th torque components. In [10], it is shown that with the increase in eccentricity, the average overall torque increases along with an increase in all of ripple contents. Dorrell *et al*. in [11] have investigated the effect of eccentricity on torque profile with respect to the switching angle. A method is presented in [12] for computing the radial magnetic forces in SR motor which includes iron saturation and eccentricity. Also, the unbalanced forces were evaluated using three different methods, namely static 2-D FEM, an analytical model, and a simplified analytical model. In [13], a dynamic response of motor under static and dynamic eccentricities has been studied using coupled 2-D FE in Matlab environment.

In the previous works, the authors have analyzed the SRG [14, 15] and SRM [16] under healthy mode utilizing 2-D and 3-D FEM. In [17], [7], and [18], the static, dynamic, and mixed eccentricity faults in the SRM are considered, respectively. Afterward, the intervals for different modes of motor operations (normal and faulty) are calculated by hybrid method in [8]. In this paper, static eccentricity in SRG is considered, for the new generator configuration.

The eccentricity fault has been studied in other generators and different applications such as [19-21], while almost there is no literature for considering the effects of eccentric rotor on the performance of SRG. This paper is an attempt to achieve this purpose.

This paper is organized as follows: the DLSRG modeling and geometrical parameters of implemented generator are presented in Section II. Section III discusses the definition of static eccentricity in generator operation. In Section IV, the finite element results of the generator profiles under normal and eccentricity fault are obtained and discussed. Results of harmonic components analysis utilizing fast Fourier transform for various eccentricities are presented in Section V. Consequently, some concluding remarks are provided in Section VI.

II. FINITE ELEMENT MODELING OF DLSRG

Accurate modeling of electrical systems is necessary in performance prediction and verification of the systems, hence to evaluate properly the generator performance a reliable model is required. The finite element method can be one of the best choices for the providing precise model for such a purpose. Therefore, a three dimensional finite element analysis is being used to determine the magnetic field distribution in and around the generator. In order to present the operation of the motor and to determine the main machine profiles at different rotor positions, the field solutions are obtained.

It has been shown that the 3-D FE approach is a precise and realistic method in comparison with the 2-D FE approach from the results obtained by the authors in [16]. The variations between 3-D/2-D FE results are due to the consideration of the end effects and also the axial fringing field in 3-D FE analysis.

The field analysis has been performed based on the variational energy minimization technique to solve for the electric vector potential. In this method, electric vector potential known as $T - \Omega$ formulation was explained by authors in [8].

The proposed generator for this study consists of two magnetically dependent stator and rotor sets (layers). The two layers are exactly symmetrical with respect to a plane perpendicular to the middle of the motor shaft. Where each stator set includes four salient poles having 45º arc length with windings wrapped around them (Fig. 1a) while, the rotor comprises of two salient poles that have different arc lengths (Fig. 1b) without any windings. The arc of each rotor pole is the same as stator pole (45º) in one side and twice as much in the other side. The side view of complete generator assembly is depicted in Fig. 1c.

There is a stationary reel, which has the field coils wrapped around it and is placed between the two-stator sets over the rotor shaft which is named as an assisted field. The motor shaft passes through a hole in the middle of the stationary reel and acts as a core for the field coil assembly.

In this format, the developed magnetic field produced by the field travels from the motor shaft to the rotor then to the stator assembly and finally completes its path via the generator housing. The cut view of the generator system with the flux path is depicted in Fig. 2 that will be analyzed using the three dimensional finite elements.

The proposed DLSR generator dimensions are listed in Table I.

The significant features in the new configuration of SR generator that make it distinct from other types of SRG are: a) the new DLSRG consist of two layers to produce South poles in one layer and the North Pole in the other layer; b) the new rotor comprises of two salient poles with different arc lengths. The rotor is shaped in such a way to produce starting torque as well as having rising inductance in all of 90º rotor arc length; c) existence of a field assisted coil on the stationary reel between two layers produces an independent field; d) due to existence of assisted field, this generator can produce higher output power than a standard self excited SRG.

It has been assumed that each analysis is carried out with four-node tetrahedral blocks for the present study.

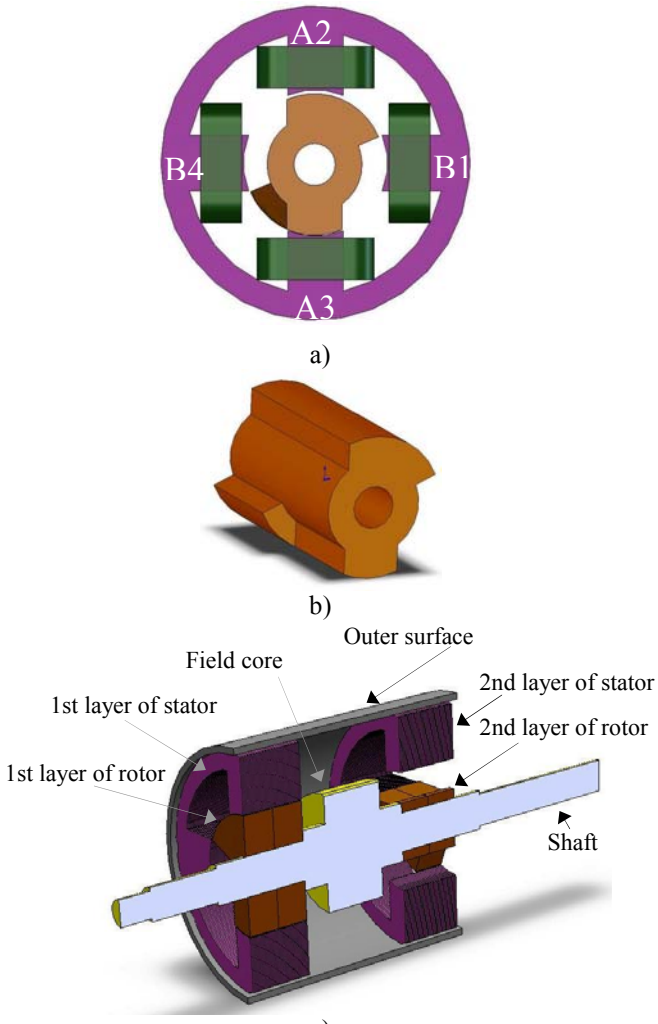

Fig. 1. a) Front view of 1st layer in DLSRG, b) rotor shape, c) a side view of DLSRG assembly (without coils).

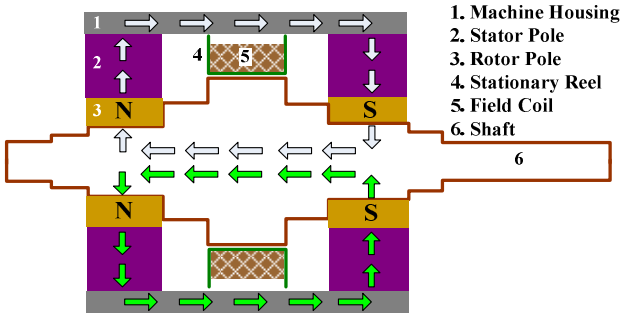

Fig. 2. A cut view of DLSRG with the flux path.

The schematic figure showing the meshes in the simulation study is illustrated in Fig. 3. In this analysis, the usual assumptions such as the magnetic field outside of an air box in which the generator is placed, is considered to be zero. Also, the analysis includes a 360 degree rotation of the rotor for the analysis of SRG behavior at the different rotor positions. Due to symmetrical behavior of the field in and around the generator, only the rotor movement of the 1st layer from unaligned to unaligned position is considered. The rotor of 2nd layer moves from fully unaligned to fully aligned position as well; therefore, all machine parameters for these points and the points in between can be computed. In this study, assisted field winding consists of 300 turns with a current magnitude of 0.5 A.

Layer one of the machine includes coils 1, 2, 3, and 4 in which coils 2, 3 belong to phase A, and coils 1, 4 belong to phase B. In layer two coils 5, 7 belong to phase A, and coils 6, 8 belong to phase B.

Table 1: DLSR generator dimensions

Parameter	Value
Stator core outer diameter	72mm
Stator core inner diameter	62mm
Stator arc	45deg
Air gap	0.25mm
Rotor core outer diameter	39.5mm
Rotor shaft diameter	10mm
Rotor larger arc	90deg
Rotor smaller arc	45deg
Stack length	35mm
Number of turns per pole	110
Number of turns for field coil	300

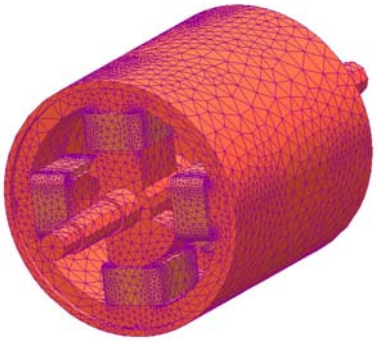

Fig. 3. Finite element mesh for the DLSRG.

III. STATIC ECCENTRICITY DEFINITION

In this type of eccentricity, the air gap distribution around the rotor is not uniform, and is

time-independent. It occurs when the rotational axis of the rotor is identical to its symmetrical axis but has been displayed with respect to the stator symmetrical axis. The degree of static eccentricity or relative eccentricity is defined as follows

$$\varepsilon_S = \left(\frac{r}{g}\right) \times 100\ (\%), \tag{1}$$

where, ε_S is the percentage eccentricity between the stator and rotor axes, g is the radial air gap length in the case of uniform air gap in healthy generator or with no eccentricity, and r is the displacement of the rotor in the horizontal direction to the excited stator poles in aligned position.

Manufacturers normally keep the total eccentricity level as low as possible in order to minimize unbalanced magnetic pull (UMP) as well as the reduction of vibration and noise. An air gap eccentricity of up to 10% is permissible as mentioned in the references. Also, due to the collision of the rotor pole with the stator pole, the relative eccentricity of more than 60% is not considered in this study.

IV. NUMERICAL RESULTS AND ANALYSIS OF DLSRG UNDER ECCENTRIC CONDITION

The reluctance variation of the generator has an important role on the performance; hence, an accurate knowledge of the flux distribution inside the generator for different excitation currents and rotor positions are essential for the prediction of machine performance.

In order to evaluate these characteristics and also investigate the effects of static eccentricity on the two-phase switched reluctance generator behavior, the generator is simulated utilizing the 3-D finite element analysis. In this analysis, the static eccentricity fault is considered in phase A direction. Hence, the rotor pole is closer to coil 3 and further away from coil 2.

A. Influence of eccentricity upon DLSR generator radial force

The eccentricity fault leads to a radial force on the rotor which tries to pull it even further away from the stator bore center. On the other hand, this phenomenon causes an unbalanced electromagnetic force in the generator. Figure 4 shows the normal radial force exerted on the rotor poles from unaligned to fully aligned and then to unaligned positions for different eccentricities.

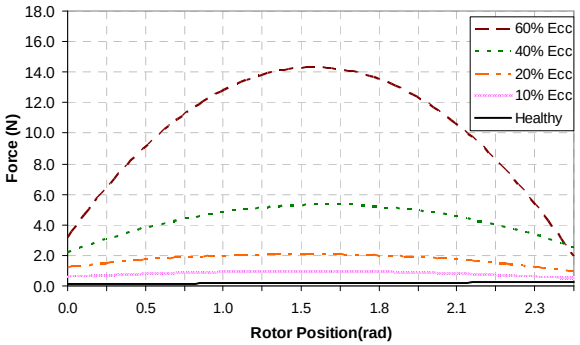

Fig. 4. Radial force in pole 2 from phase A in field assisted mode.

As shown in Fig. 4, the radial force is almost zero in healthy mode due to the magnetic pull compensation of the opposite poles.

Figure 4 shows about 140 times larger radial force when 60% eccentricities are occurred in comparison with healthy mode. Also, the radial force has increased by a factor of 3 when the eccentricity has changed from 40% to 60%. It has also been shown that, the maximum force is produced when the rotor poles are fully aligned with the stator poles. It is also evident from the figure, when the amount of eccentricity fault increases, the exerted force will also go up as well.

B. Influence of eccentricity upon DLSR generator mutual flux

In the field assisted mode of operation, the stationary reel that is placed between the two-stator layers is set at 0.6A, and the stator coils are not excited. In this format, the developed magnetic field from the stator poles travels to the rotor then to the shaft and finally completes its path via the generator housing. In this mode of operation, the power generation is obtained by energizing the proper stator coils during the negative inductance periods. Therefore, the flux linkage of phase A and B are calculated from unaligned to fully aligned and then to unaligned positions (the fully aligned position is at 1.57 radian). Regarding to the occurrence of fault in direction of phase A, the variations of flux in coils 1 and 4 from phase B are

negligible, while, the variation of flux in coils 2,3 of phase A are noticeable, Fig. 5 and Fig. 6 show the flux variations for a healthy generator and a generator with various eccentricities. In these figures, the flux data points have been estimated with second order functions using least squares method, for better illustration.

The non-uniformity of air gap is time invariant when static eccentricity exists; therefore, the distribution of air gap does not change as the rotor turns. Hence, the flux for each phase is repeated identically in every cycle.

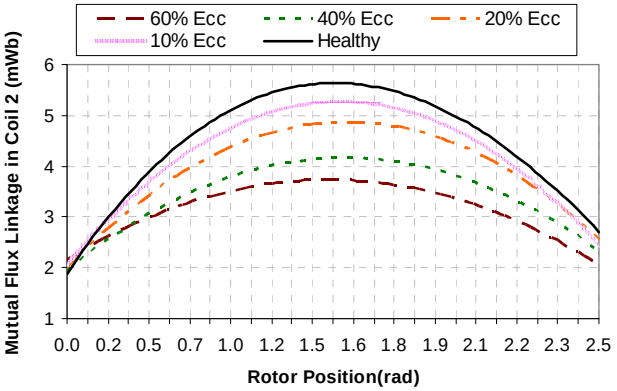

Fig. 5. Mutual flux linkage in coil 2 from phase A in field assisted mode.

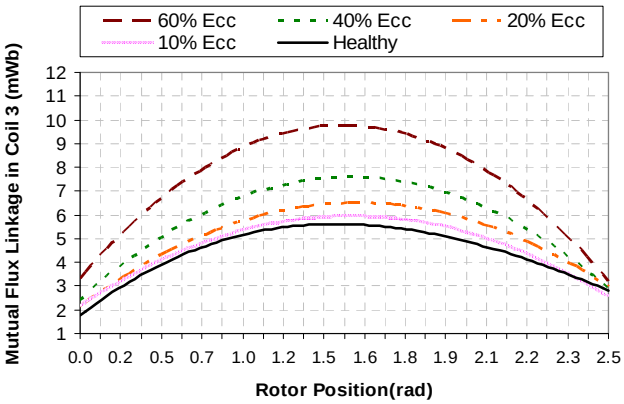

Fig. 6. Mutual flux linkage in coil 3 from phase A in field assisted mode.

C. Influence of eccentricity upon DLSR generator mutual inductance

It is imperative to look at the field coil inductance curve at this point to see how it varies as the rotor turns. It can provide useful information for explaining the influence of fault in generator operation.

The so called "effective" mutual inductance has been defined as the ratio of each phase flux linkages to the exciting current of assistant field ($\lambda(\theta)/I_f$). Based on this definition, the mutual inductance value of coil 2 in phase A versus rotor position is presented in Fig. 7 for healthy motor as well as the motor with a range of eccentricity faults. In Fig. 7, the shape of mutual inductance from aligned position to unaligned position (1.57 rad-2.5 rad) is depicted and also linear approximation is utilized for more accuracy and clarity.

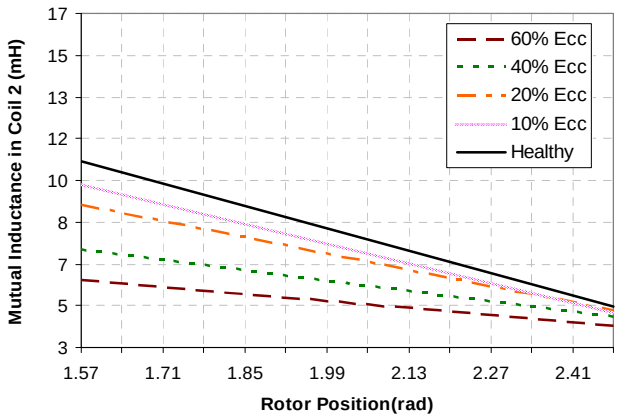

Fig. 7. Mutual inductance in coil 2 from phase A in field assisted mode.

As seen from curves in Fig. 7, the slopes of mutual inductance decrease when the eccentricity levels go up, and also the magnitudes of mutual inductance for each eccentricity level reduces, as the rotor move into the unaligned position. It is also observed that amplitude of mutual inductance of the A-2 has 45%, 32%, 18%, and 9% reduction with 60%, 40%, 20%, and 10% eccentricities compared with healthy generator in fully aligned position, respectively as shown in Fig. 7. Also, as shown in this figure, the slopes of mutual inductance in A-2 for 60%, 40%, 20%, and 10% fault is about 2.2, 1.8, 1.3, and 0.5 times lower than the slope of mutual inductance in a healthy generator.

These reductions are due to air gap length increases between the stator and rotor poles in front of coil 2. On the other hand, the eccentricity phenomenon caused to reduce the difference between maximum and minimum mutual

inductance values in coil 2. Since the produced torque and induced voltage in SR machines are directly proportional to the variation of inductance with respect to rotor position, then the torque and voltage production profiles in motoring and generating modes of operation will vary accordingly. The following formulas for the SR machine in the linear mode of operation will prove the above statement.

$$T = \frac{1}{2} i^2 \frac{dL}{d\theta} \tag{2}$$

$$e_{ind} = \omega \frac{d\lambda}{d\theta} \tag{3}$$

where, T is the torque, i is phase current, L is phase inductance, θ is rotor position, e_{ind} is generated voltage and ω is angular speed.

Figure 8 shows the calculated mutual inductance versus rotor position obtained by the ratio of flux linking coil 3 to the field current.

As depicted in this figure, the magnitude of mutual inductance has been increased, for each rotor position. As the eccentricity levels go up, the slope of mutual inductance will also change noticeably. The slopes of mutual inductance in A-3 for eccentric generator under 60%, 40%, 20%, and 10% fault has almost 47%, 36%, 16%, and 8% higher value than the slope of mutual inductance in a healthy generator.

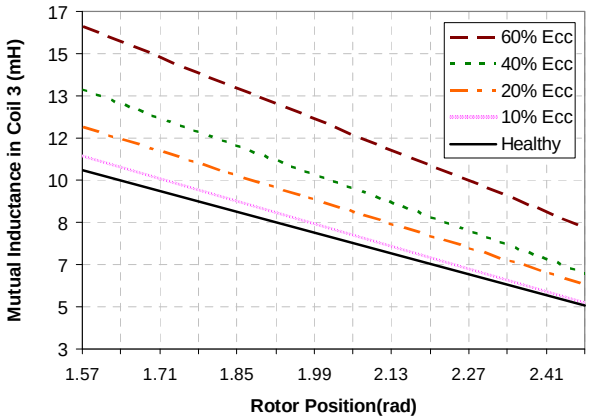

Fig. 8. Mutual inductance in coil 3 from phase A in field assisted mode.

Also, as demonstrated in this figure, amplitude of mutual inductance of the A-3 has 56%, 28%, 16%, and 4.8% increase with 60%, 40%, 20%, and 10% eccentricity compared with a healthy generator in the fully aligned position, respectively as shown in Fig. 8. These changes are due to the decrease in the air gap length between the stator and rotor poles in front of coil 3.

Therefore, variation of mutual inductances, as well as the area under their curves can be addressed as a fine index for eccentricities diagnosis.

The mutual inductance in other coils such as 1, 4 do not experience noticeable changes. The calculated results and the shape of mutual inductance in Fig. 7 and Fig. 8 point to two fundamental achievements: first, the variations of each coil and its magnitude present the fault occurrence and the level of eccentricity. Second, the increased mutual inductance magnitude of coil 2 and the reduction of mutual inductance magnitude of coil 3 shows that the rotor pole is near coil 3 and further away from coil 2, therefore the direction of fault can also be detected in this manner.

V. Fourier Analysis of Mutual Inductance/Rotor Angular Position Characteristics

The fast Fourier transform (FFT) is a classical spectral estimation technique which is an efficient algorithm and one of the most robust ones. Therefore, the analysis based on FFT has been proposed to extract frequency information from the mutual inductance as a diagnostic index in order to detect the rotor misplacement.

Results of the harmonic components analysis for the mutual inductance profile in phase A (faulty phase) in the field assisted mode using 3-D FEM for various eccentricities are presented in Fig. 9 and Fig. 10. As depicted in Fig. 9 with an increase in the eccentricity level, there is a decrease in the fundamental harmonic and other components of mutual inductances in coil 2. These changes obtained from the mutual inductance curve behavior in time domain. As shown in this figure, the amplitude of the fundamental component in coil 2 for healthy motor is almost 1.5 times higher than those of fundamental components in a faulty motor with 60% eccentricity. Also, in eccentric motor with 10%, 20%, and 40% faults, these components are faced with 7%, 12%, and 25% drop in their amplitudes. It is observed that variations of other components are also the same as the fundamental component.

Figure 10 illustrates that the fundamental harmonic as well as other harmonic components of mutual inductance in coil 3 have increased with raising the eccentricity level. These changes are due to reduction of the corresponding air gap size in the time domain, which affects the amplitude of the frequency components. As shown in this figure, the amplitude of fundamental component in coil 3 for faulty generator with 60% eccentricity is almost 1.5 times higher than those of fundamental component in a healthy motor. In addition, this component experiences 4.5%, 16.7%, and 29.6% rise in its magnitude in eccentric motor with 10%, 20%, and 40% faults. It is also observed that the variations of other frequency components are the same as the fundamental component.

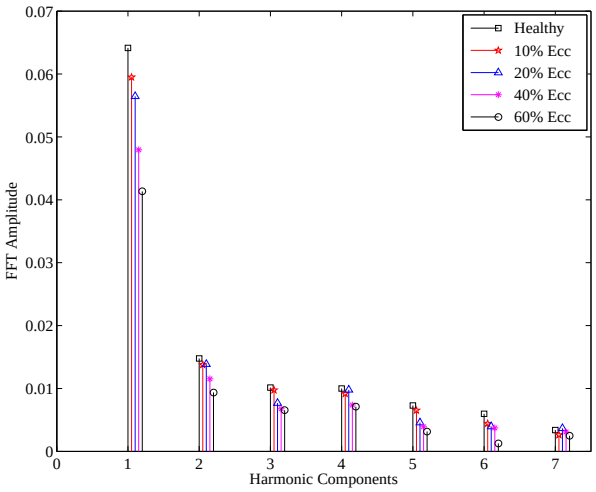

Fig. 9. FFT of mutual inductance in coil 2 from phase A for 3-D FEM in healthy motor and motor with various eccentricities.

VI. CONCLUSION

This paper analyzes the eccentricity fault diagnosis in a new two phase switched reluctance generator. For this purpose, the static eccentricity was modeled and analyzed using 3-D-FEM by considering the end effects and axial fringing fields for implementation of a reliable model. With occurrence of fault, it is observed that the amplitude of mutual inductance of coils 2 and 3 from faulty phase (A) with 60% eccentricity will show 45% reduction and 56% increase compared with a healthy generator in the fully aligned position. Also, the slopes of the mutual inductance in coils 2 and 3 from faulty phase (A) for 60% fault are about 2.2 times lower and 0.47 times higher than the slope of mutual inductance in a healthy generator.

The amplitude and slope of mutual inductance in time domain and its amplitude of a fundamental component in frequency domain were used for fault diagnosis and then proposed as a diagnostic index. Regarding to the fault detection in DLSRG, useful results can be obtained by just evaluating only one of the phases from each layer, moreover this procedure and diagnosis can be applied to other types of SRG as well. On the other side, the calculated results show that the direction of static eccentricity fault can be effectively detected by evaluation of this index from two coils in one phase.

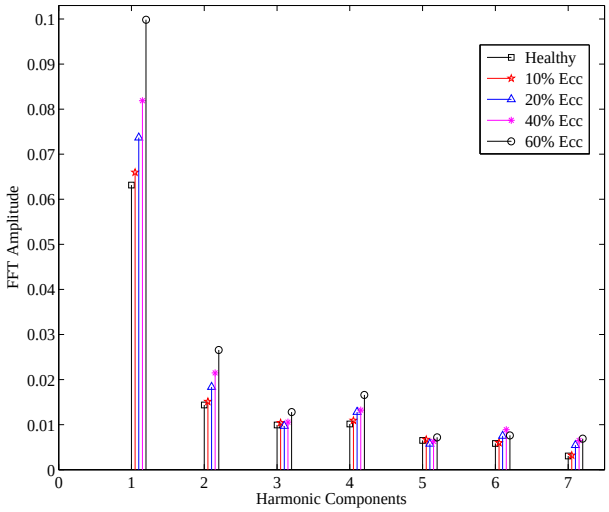

Fig. 10. FFT of mutual inductance in coil 3 from phase A for 3-D FEM in healthy motor and motor with various eccentricities.

ACKNOWLEDGMENT

This work was supported by vice-presidency of research and technology of Shahid Beheshti University.

REFERENCES

[1] Y. Chang, and C. Liaw, "On the Design of Power Circuit and Control Scheme for Switched Reluctance Generator," *IEEE Transactions on Power Electronics*, vol. 23, no. 1, pp. 445-454, 2008.

[2] E. Afjei, and H. Torkaman, "Comparison of Two Types of Dual Layer Generator in Field Assisted Mode Utilizing 3-D-FEM and Experimental Verification," *Progress in*

Electromagnetics Research B, vol. 23, pp. 293-309, 2010.

[3] D. Torrey, "Switched Reluctance Generators and Their Control," *IEEE Transaction on Industrial Electronic,* vol. 49, no. 1, pp. 3-14, 2002.

[4] D. McSwiggan, L. Xu, and T. Littler, "Modelling and Control of a Variable Speed Switched Reluctance Generator based Wind Turbine," in 42nd International Universities Power Engineering Conference, pp. 459-463, 2007.

[5] L. Moreau, M. Machmoum, and M. E. Zaïm, "Design of Low-Speed Slotted Switched Reluctance Machine for Wind Energy Applications," *Electric Power Components and Systems, Taylor and Francis,* vol. 34, no. 10, pp. 1139-1156, 2006.

[6] A. Martinez, and *et al*., "Use of an AC Self-Excited Switched Reluctance Generator as a Battery Charger," in 13th Power Electronics and Motion Control Conference, pp. 845–849, 2008.

[7] H. Torkaman and E. Afjei, "Magnetio Static Field Analysis Regarding the Effects of Dynamic Eccentricity in Switched Reluctance Motor," *Progress in Electromagnetics Research M, PIER,* vol. 8, pp. 163-180, 2009.

[8] H. Torkaman and E. Afjei, "Hybrid Method of Obtaining Degrees of Freedom for Radial Air Gap Length in SRM under Normal and Faulty Conditions Based on Magnetiostatic Model," *Progress In Electromagnetics Research, PIER,* vol. 100, pp. 37-54, 2010.

[9] N. K. Sheth and K. R. Rajagopal, "Effects of Nonuniform Air Gap on the Torque Characteristics of a Switched Reluctance Motor," *IEEE Transactions on Magnetics,* vol. 40, no. 4, pp. 2032-2034, 2004.

[10] N. K. Sheth and K. R. Rajagopal, "Variations in Overall Developed Torque of a Switched Reluctance Motor with Air Gap Nonuniformity," *IEEE Transactions on Magnetics,* vol. 41, no. 10, pp. 3973-3975, 2005.

[11] D. G. Dorrell, I. Chindurza, and C. Cossar, "Effects of Rotor Eccentricity on Torque in Switched Reluctance Machines," *IEEE Transactions on Magnetics,* vol. 41, no. 10, pp. 3961-3963, 2005.

[12] I. Husain, A. Radun, and J. Nairus, "Unbalanced Force Calculation in Switched-Reluctance Machines," *IEEE Transactions on Magnetics,* vol. 36, no. 1, pp. 330-338, 2000.

[13] J. R. Briso-Montiano, R. Karrelmeyer, and E. Dilger, "Simulation of Faults by Means of Finite Element Analysis in a Switched Reluctance Motor," in Multiphysics Conference, pp. 1-6, Frankfurt, 2005.

[14] E. Afjei and H. Torkaman, "The Novel Two Phase Field-Assisted Hybrid SRG: Magnetio Static Field Analysis, Simulation, and Experimental Confirmation," *Progress in Electromagnetics Research B, PIER,* vol. 18, pp. 25-42, 2009.

[15] E. Afjei and H. Torkaman, "Comparison of Two Types of Hybrid Motor/Generator," in 20th International Symposium on Power Electronics, Electrical Drives, Automation and Motion (SPEEDAM), pp. 982-986, Pisa, Italy, 2010.

[16] H. Torkaman and E. Afjei, "Comprehensive Study of 2-D and 3-D Finite Element Analysis of a Switched Reluctance Motor," *Journal of Applied Sciences,* vol. 8, no. 15, pp. 2758-2763, 2008.

[17] H. Torkaman and E. Afjei, "Comprehensive Magnetic Field-Based Study on Effects of Static Rotor Eccentricity in Switched Reluctance Motor Parameters Utilizing Three-Dimensional Finite Element," *Electromagnetics, Taylor and Francis,* vol. 29, no. 5, pp. 421 - 433, 2009.

[18] E. Afjei and H. Torkaman, "Air Gap Eccentricity Fault Diagnosis in Switched Reluctance Motor," in 1st Power Electronic and Drive Systems and Technologies Conference, PEDSTC, Tehran, Iran, 2010, pp. 284-289.

[19] R. Perers, U. Lundin, and M. Leijon, "Saturation Effects on Unbalanced Magnetic Pull in a Hydroelectric Generator With an Eccentric Rotor," *IEEE Transactions on Magnetics,* vol. 43, no. 10, pp. 3884-3890, 2007.

[20] S. Keller, M. T. Xuan, J.-J. Simond, and A. Schwery, "Large Low-Speed Hydro-Generators Unbalanced Magnetic Pulls and Additional Damper Losses in Eccentricity Conditions," *IET Electric Power*

Applications, vol. 1, no. 5, pp. 657 - 664, 2007.

[21] C. Bruzzese, E. Santini, V. Benucci, *et al.*, "Model-Based Eccentricity Diagnosis for a Ship Brushless-Generator Exploiting the Machine Voltage Signature Analysis," in IEEE International Symposium on Diagnostics for Electric Machines, Power Electronics and Drives, pp. 1-7, 2009.

Hybrid UV/MLFMA Analysis of Scattering by PEC Targets above a Lossy Half-Space

Mengmeng Li[1], Hua Chen[1], Chunyan Li[1], Rushan Chen[1], and Chong-Jing Ong[2]

[1] Department of Communication Engineering
Nanjing University of Science and Technology, China
david2000abc@126.com, eechenrs@mail.njust.edu.cn

[2] Corporate Engineering, Micron Technology, Inc., Boise, ID 83707 USA
ong_chong_jin@hotmail.com

Abstract ─ An efficient hybrid UV method and the multilevel fast multipole algorithm (MLFMA) is proposed for the analysis of scattering by arbitrary three-dimensional(3-D) perfect electric conductor (PEC) targets above a lossy half-space. The proposed method modifies the MLFMA based on the real-image representation of the half-space dyadic Green's function. Unlike the original MLFMA, the interaction matrix of the UV/MLFMA is split into the "near" terms, the "intermediate" terms, and the "far" terms. The "near" terms are handled via the method of moments (MoM), the "intermediate" terms are handled via the UV method, and the "far" terms are handled via the MLFMA. The error arising from the approximation to the half-space dyadic Green's function via the real-image representation in the "intermediate" terms can be avoided by using the UV matrix compression. The memory requirement and computational time of the "near" terms are also decreased significantly compared with the original MLFMA.

Index Terms ─ Half-space, multilevel UV method, MLFMA, and real-image.

I. INTRODUCTION

There is much interest in scattering from conducting objects situated above a lossy half-space, as there are many applications such as communications, target identification, and remote sensing. The MoM is the preferred method, since by using the integral equation (IE) and the half-space dyadic Green's functions, it only discretizes the metallic surface, which leads to a relatively small number of unknowns. The most challenging aspect of such a problem is the evaluation of the spatial domain half-space dyadic Green's functions which are expressed in terms of the Sommerfeld integrals (SI's). There is much research to solve the SI's, including the steepest-descent path (SDP) approach [1], and the discrete complex image method (DCIM) [2].

The implementation of the MoM requires $O(N^3)$ operations and $O(N^2)$ memory storage, where N is the number of unknowns. The size of the MoM matrix increases so rapidly that the computation will be intractable for a large number of unknowns. The difficulty can be overcome by use of Krylov iterative methods, and the required matrix-vector multiplication can be accelerated by the MLFMA [3-6]. The MLFMA is based on the addition theorem and the plane wave expansion, which are primarily in the context of the free space Green's function. It is not directly applicable to the half-space problem due to the complex form of the spatial domain Green's functions of half-space. In [7], a steepest-descent fast multipole method (SDFMM) was proposed for analysis of the quasi-planar structures whose transverse dimensions are much larger than the height. The SDFMM relies on a representation of the 3-D Green's functions to a steepest-descent integral coupled with a two-dimensional (2-D) fast multipole method. Therefore, it was applied to solve the problems concerning quasi-static structures such as scattering from the rough surface [8] and radiation from the microstrip antennas [9] etc efficiently. In [10-11], the MLFMA has been extended for general targets in the presence of a lossy half

space. Since the "far" interactions between distant groups are less sensitive to accurate evaluation, the spatial domain Green's functions are approximated by both the direct-radiation term and the radiation term from a single real-image [10-11]. Then the computation of the "far" terms can be accelerated by the MLFMA. Due to the advantage of this technique, the MLFMA based on real-image approximation is extended to analyze the EM scattering by the arbitrary chiral objects above a lossy half-space [12].

The real-image representation of the Green's function is appropriate for expansion when the source and observation points are separated by a wavelength or more [13]. This determines the large minimum group size of the MLFMA, which leads to a low efficiency, as the minimum group size of the MLFMA at mid frequency in free space is around 0.2 wavelength. In [11], a higher order approximation for efficient evaluation of the half-space Green's function based on the large-argument approximation of Bessel function and Taylor series expansion is considered. The method can analyze targets in direct contact with the interface of a lossy half-space. However, the formula is complex and complicated to implement. In [14], the half-space dyadic Green's function is split into a term representing the "direct" radiation between source and observation points and a remaining "reflect" term accounting for interactions with the interface. The expansion coefficients of the "reflect" term are obtained by the sampling points in the source and observation groups. This approximation is easy to implement. However, the error of the approximation may be uncontrollable, since it is difficult to determine the appropriate sampling points.

The drawback of the MLFMA is its dependence on the integral kernel. For complex Green's functions, the application of the MLFMA is much more involved than in the free space. Thus, a large number of fast integral equation algebraic methods have already been developed. The matrix decomposition based methods such as IES^3 (ice cube) [15], hierarchical (H) matrices method [16], adaptive cross approximation (ACA) [17], and UV method [18] are kernel function independent. They are easy to be applied in the existing MoM code without a large change of the algorithms. However, the above methods are only efficient for moderate size problems, for large scale problems or at a high level of the tree structure in the algorithms the actual complexity is higher [19]. Therefore, in this paper, the multilevel UV method [16] is only used in the "intermediate" terms to overcome the difficulties for the approximation to the half-space Green's function and to avoid the higher computational complexity in the "far" terms. The computational complexity and memory requirement of the multilevel UV method is $O(rN\log N)$, where r is the typical (average) rank at the largest level [16, 18]. The half-space Green's function in the "intermediate" terms is evaluated via DCIM rigorously, and the multilevel UV method needs to only deal with the final low-ranked interaction matrix. Thus, the approximation error is controllable via the threshold in the UV matrix compression [16]. Since we focused on the analysis of the PEC targets by the hybrid UV/MLFMA, the MLFMA based on the real image approximation will not be described in this paper. The details can be found in references [8-10].

The remainder of the paper is organized as follows. Section II describes the essential algorithms for the analysis of the PEC targets above a lossy half-space. The half-space MoM formulation is described in Section II-A; the multilevel UV method based on the octree structure is described in Section II-B and the hybrid UV/MLFMA is described in Section II-C. Numerical results in Section III demonstrate the validity of the proposed method. Finally, a brief final conclusion is given in Section IV.

II. THEORY

A. Integral equation and half-space MoM formulation

For solving scattering by a PEC target located above a lossy half-space, the electric-field integral equation (EFIE) is utilized:

$$j\omega u_1 \int_s \left(\bar{\bar{\mathbf{I}}} + \frac{\nabla\nabla'}{k_1^2} \right) \bullet \bar{\bar{G}}^A \bullet \mathbf{J} dS' = \mathbf{E}^i(\mathbf{r}), \qquad (1)$$

where $\bar{\bar{G}}^A$ is the spatial domain dyadic Green's function and can be expressed as follows:

$$\bar{\bar{G}}^A = G_{xx}^A(\hat{x}\hat{x} + \hat{y}\hat{y}) + G_{zx}^A \hat{z}\hat{x} + G_{zy}^A \hat{z}\hat{y} + G_{zz}^A \hat{z}\hat{z}. \qquad (2)$$

The spatial expressions of the above Green's functions are often expressed in terms of SI's. In this paper, DCIM combined with the two-level generalized-pencil of function method (GPOF) [20] is employed to evaluate efficiently the Greens' function for a half space.

B. Multilevel UV method

The multilevel UV method is a rank-based method. Generally, the interaction matrix is full-ranked when the observation groups are in the near field of the source group, while the interaction matrix between them is low-ranked when the observation groups are in the far field. Application of the UV decomposition to the low-ranked impedance matrix will result in significant memory and computational time savings. The classification of the interaction groups in this paper is based on the octree structure. A three level octree structure is demonstrated in Fig. 1.

Considering a 2-D target locating within a square region as an example (for the 3-D targets, it will be located within a cube, and the principle of classification of the interaction groups is the same as the 2-D). The square region is spitted into levels using the octree algorithm until there are some dozens of RWG functions in the minimum groups. For the observation block (block 1) at level-1, the impedance matrix can be decomposed into P sparse matrices, where P is the number of levels.

$$\mathbf{Z} = \mathbf{Z}_0 + \mathbf{Z}_1 + \cdots + \mathbf{Z}_{p-1}. \tag{3}$$

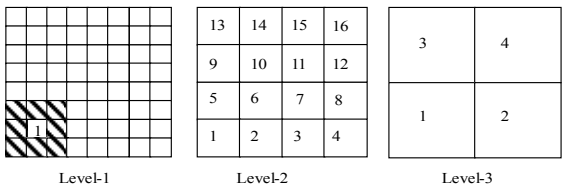

Fig. 1. A three level octree structure.

$\mathbf{Z}_0$ is the impedance matrix for the interactions of self and neighboring blocks (the hatched blocks and the self interaction block in Fig. 1) at level-1. The region of $\mathbf{Z}_0$ is defined as the near field of block 1 at level-1. $\mathbf{Z}_1$ and so forth are the impedance matrices for the interactions of the far field which is defined as the parent block's near field and the current block's far field. As shown in Fig. 1, for level-1, the far field of block 1 at level-1 is the region of blocks 5, 6, 2 at level-2 with the region of the near field of block-1 at level-1 excluded, since the block 1 at level-2 is the parent block of block 1 at level-1 and the blocks 5, 6, 2 are the neighbors of block 1 at level-2. Similarly, for level-2, the far field of block 1 at level-1 is the region of blocks 3, 4, 2 at level-3. Accordingly, all the interactions to block 1 at level-1 can be computed.

$\mathbf{Z}_0$ is full-ranked and is stored directly. For $\mathbf{Z}_1$ and so forth, the matrices are operated in two different ways according to their size when applying the UV method. When the size of the matrix is small, it will be computed directly and its rank is evaluated by singular value decomposition (SVD), after which the U and V matrices can be obtained. When the size of the matrix is large, column and row sampling according to rank estimates is performed and SVD on the sampled matrix is implemented instead. The $m \times n$ matrix is then decomposed into $\mathbf{U}_{(m\times r)}$ and $\mathbf{V}_{(r\times n)}$ matrices, which leads to significant time and memory savings when the matrix is low-ranked [21, 22]. It should be note that the process of the rank estimation spends no extra time compared with the process of the rank-revealing process of the ACA [17], since the **U** and **V** matrices are formed simultaneously within the SVD process.

C. The hybrid multilevel UV method and MLFMA

In this paper, the UV method is used to evaluate the "intermediate" terms to avoid the real-image representation of the half-space Green's function in this region. The UV/MLFMA method is similar to the multilevel UV method in that the impedance matrix is decomposed into P sparse matrices, where P is the number of levels

$$\mathbf{Z} = \mathbf{Z}_0 + \mathbf{Z}_1 + \cdots \mathbf{Z}_q + \cdots + \mathbf{Z}_{p-1}. \tag{4}$$

The hybrid method classifies the impedance matrix to the "near" terms, the "intermediate" terms, and the "far" terms as shown in Fig. 2. The "near" terms ($\mathbf{Z}_0$) are the same as described in section 2.2 and are evaluated by MoM. The "intermediate" terms are between the near terms and the half wavelength group size in the tree structure ($\mathbf{Z}_1$ to $\mathbf{Z}_q$), and are evaluated by the multilevel UV method. The half-space Green's functions in the above two terms are evaluated

rigorously by the DCIM [2]. The "far" terms are the region where the group size is larger than half a wavelength ($\mathbf{Z}_{q+1}$ and so forth), and are evaluated by the MLFMA based on real-image approximation technique.

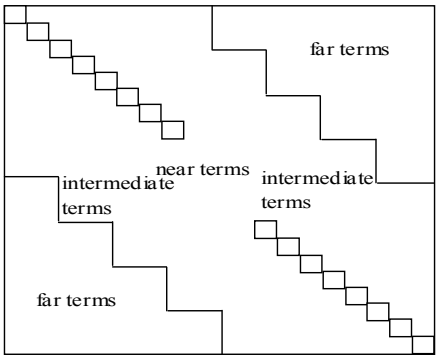

Fig. 2. The classification of the impedance matrix in the UV/MLFMA.

III. RESULTS AND DISCUSSIONS

Some numerical results of the PEC targets above a lossy half-space are shown in this section. The double floating point precision is used in the code to enhance the accuracy of the simulated results. All the numerical examples are computed on an Intel® CoreTM 2 with 3.0 GHz CPU's (the results are computed by only one processor) and 4 GB RAM. In this section the label "MoM" represents the simulated results by MoM rigorously, the "MLFMA" represents the simulated results by MLFMA based on the real image approximation, and the "UV/MLFMA" represents the simulated results by hybrid UV/MLFMA proposed in this paper. First, we analyze the scattering from a conducting sphere located at 0.7m above the lossy half-space characterized by $\varepsilon_{half} = (5.0, -0.2)$, $\mu_{half} = 1.0$ and $\sigma_{half} = 0.$ The radius of the sphere is 0.5m and 2, 656 triangle patches are used to discretize its surface [14]. The incident and scattered directions are ($\theta^i = 0^\circ, \varphi^i = 0^\circ$) and ($0^\circ \le \theta^s \le 90^\circ, \varphi^s = 0^\circ$), respectively. The frequency of the incident plane wave is 300MHz. Figures 3 and 4 show the bistatic RCS computed by the MoM, the proposed method (one level UV method), and the MLFMA. The minimum group size for the octree structure is 0.5 λ_0 and 0.25 λ_0 , respectively. It can be found that when the minimum group size is 0.5 λ_0 , the results simulated by the MLFMA and the hybrid UV/MLFMA agree well with the results obtained by the MoM. But, when the minimum group size is minimized to 0.25 λ_0 , the results simulated by the hybrid UV/MLFMA agree better with the results obtained by the MoM than the results obtained by the MLFMA. Thus, the proposed method has a clear advantage of reducing the region of the "near" interactions that must be evaluated rigorously using the MoM. The total solution time for the MoM is 304.6 s, while the total solution time for the UV/MLFMA and MLFMA is 284.3 s and 97.3 s respectively. The proposed UV/MLFMA is more accurate than MLFMA when the minimum group size is smaller than 0.25 λ_0 .

Figure 5 shows the bistatic RCS of a PEC cylinder of height 3m and diameter 1m situated 20cm above Yuma soil of 10% water content. The metallic surface is discretized with 10, 404 triangle patches and the number of unknowns is 15, 606. The incident and scattered directions are ($\theta^i = 60^\circ, \varphi^i = 0^\circ$) and ($\theta^s = 60^\circ, -180^\circ \le \varphi^s \le 180^\circ$), respectively. It is found that the results computed by the proposed method (one level UV method and three level MLFMA) agree well with the results in [10]. The minimum group size of the UV/MLFMA is 0.25 λ_0 and the average number of RWG functions in the groups with minimum group size is 20. The "intermediate" term interactions are evaluated at the lowest level via the UV method and the "far" terms interactions are evaluated at level-2, level-3, and level-4 via the MLFMA. Figure 6 shows the comparison of the ranks and the column dimensions of the interaction matrices produced by the first group at the minimum level and its interaction groups. The number of the unknowns in the first group is 22. It is found that the dimensions of the interaction matrices are around 20 while the ranks are around 8 with the threshold of 10^{-4} in the matrix decomposition, which demonstrate the rank deficiency of the sub matrices in the proposed UV/MLFMA. By using the UV method in the "intermediate" terms, the size of the near field in the original MLFMA is decreased and its memory requirement is decreased from 226MB to 95MB, and the total solution time is decreased from 6929.1s to 4524.6 s.

Figures 7 and 8 show the memory requirement and CPU time respectively for the "near" terms of

the MLFMA and the "near" and "intermediate" terms of the UV/MLFMA versus frequency for a tank model above a lossy half-space characterized by $\varepsilon_{half} = (5.0, -0.2)$, $\mu_{half} = 1.0$, and $\sigma_{half} = 0$. The length of the tank is 10.3m, the width is 3.3m, and the height is 2.3 m. The incident frequency of the plane wave is changed from 0.12GHz to 0.36GHz and the number of unknowns is changed from 21, 354 to 79, 008. It is found that significant memory requirements and CPU time are both saved in the "near" terms compared with the MLFMA for the proposed method in the simulated frequency band, which demonstrate the validity of the UV/MLFMA method. Figures 9 and 10 show the bistatic RCS for the VV- and HH-polarization of the tank model at the frequency 120 MHz. The incident and scattered directions are ($\theta^i = 0^\circ, \varphi^i = 0^\circ$) and ($\theta^s = 60^\circ, 0 \le \varphi^s \le 180^\circ$). Good agreement can be found.

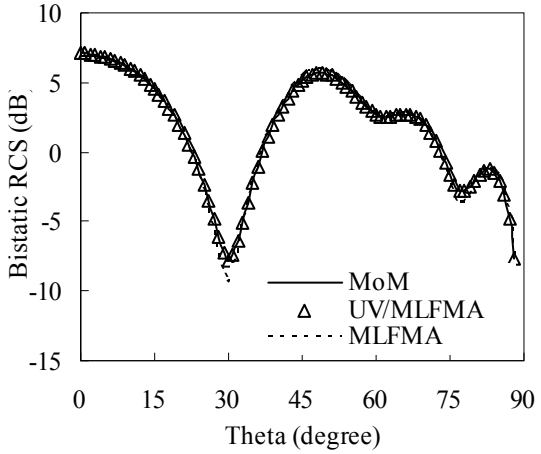

Fig. 3. Bistatic scattering cross section for VV-polarization of the conducting sphere at $\varphi = 0^\circ$. The minimum group size is $0.5\lambda_0$ for both the hybrid UV/MLFMA and the MLFMA based on real-image approximation.

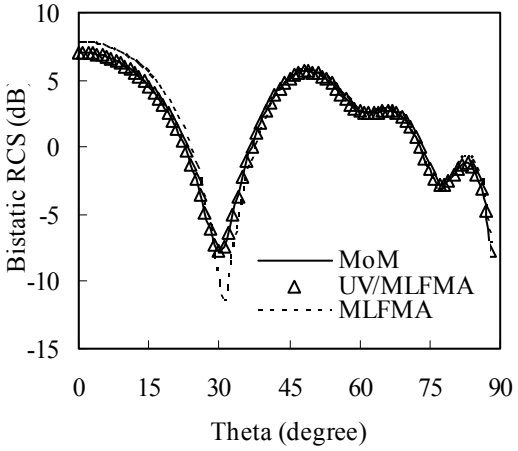

Fig. 4. Bistatic scattering cross section for VV-polarization of the conducting sphere at $\varphi = 0^\circ$. The minimum group size is $0.25\lambda_0$ for both the hybrid UV/MLFMA and the MLFMA based on real-image approximation.

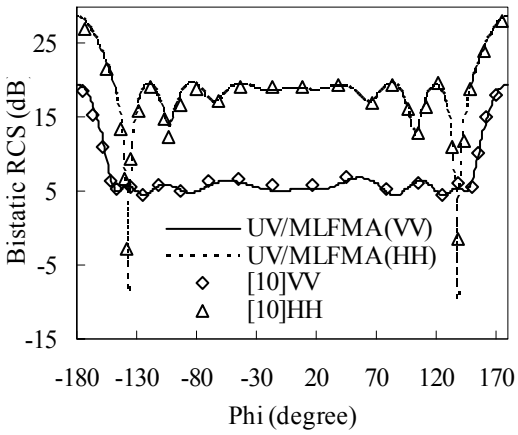

Fig. 5. Bistatic scattering cross section for VV- and HH-polarization of a PEC cylinder of height 3m and diameter 1m situated 0.2m above Yuma soil of 10% water content.

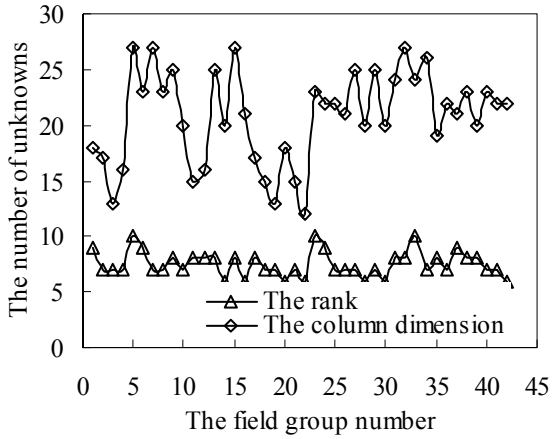

Fig. 6. The rank of the interaction matrix and the column dimensions of the first group at the minimum level. The horizontal axis represents the local group number of the observation groups in the "intermediate" field of the first group. And the vertical axis represents the number of unknowns in the observation groups, i.e. the column dimensions of the interaction sub-matrices. And the number of unknowns in the first group is 22.

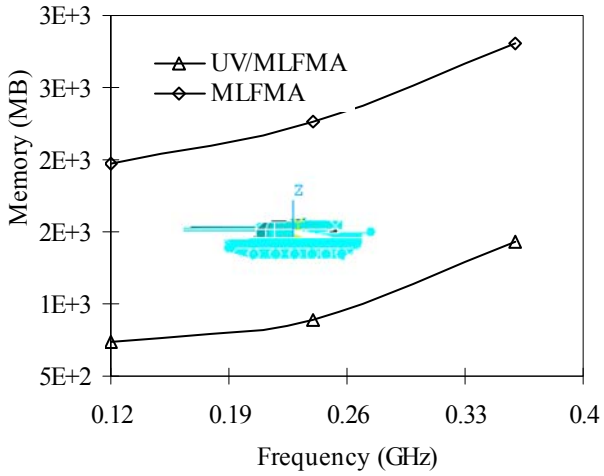

Fig. 7. Memory requirement for the "near" terms of the MLFMA and the "near" and "intermediate" terms of the UV/MLFMA versus the frequency for analysis of the tank above a lossy half-space.

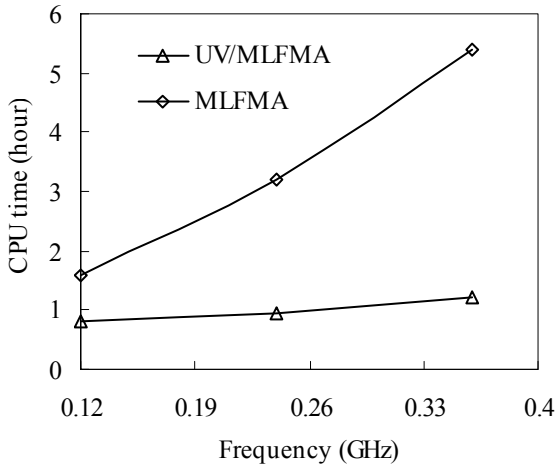

Fig. 8. CPU time for the "near" terms of the MLFMA and the "near" and "intermediate" terms of the UV/MLFMA versus the frequency for analysis of the tank above a lossy half-space.

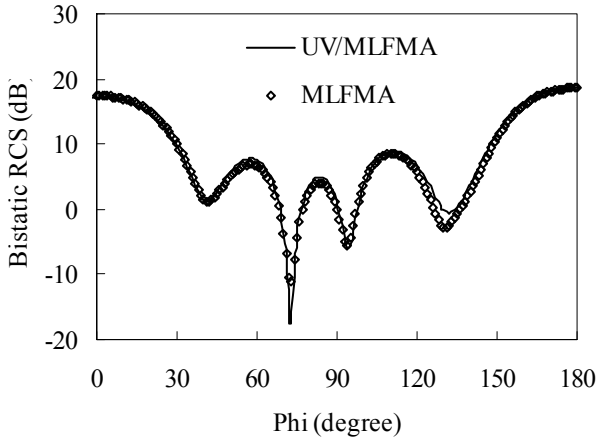

Fig. 9. The bistatic RCS for the VV-polarization of the tank model at the frequency 120 MHz.

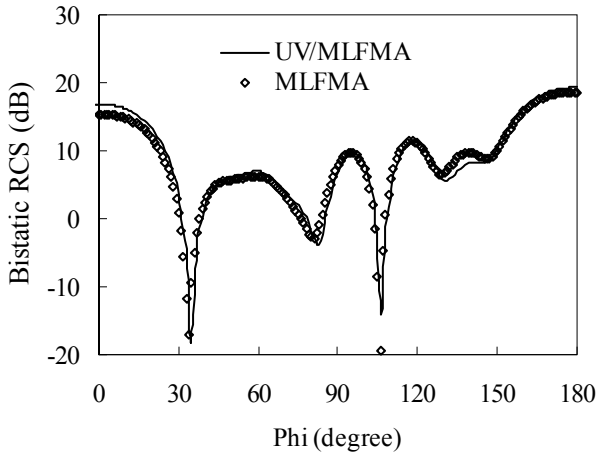

Fig. 10. The bistatic RCS for the HH-polarization of the tank model at the frequency 120 MHz.

IV. CONCLUSIONS

In this paper, a hybrid UV/MLFMA is proposed for the analysis of scattering by PEC targets above a lossy half-space. The multilevel UV method is applied to handle the interaction in the "intermediate" terms. The MLFMA is applied to handle the interaction in the "far" terms. By using the UV method in the "intermediate" terms, the error of the real-image approximation can be avoided and the size of the "near" terms of the original MLFMA is decreased. In this paper, we focused on analyzing PEC targets above a lossy half-space. For dielectric targets [11-12], the proposed method is also applicable with little change of the code.

ACKNOWLEDGMENT

We would like to thank the support of the Major State Basic Research Development Program of China (973 Program：2009CB320201).

REFERENCES

[1] T. J. Cui and W. C. Chew, "Fast Evaluation of Sommerfeld Integrals for EM Scattering and Radiation by Three-Dimensional Buried Objects," *IEEE Trans. Geosci. Remote Sensing,* vol. 37, pp. 887-900, Mar. 1999.

[2] R. S. Chen, W. Zhuang, D. X. Wang, and D. Z. Ding, "A Robust Method for Determination the Surface Waves Components of a Multilayered Media," *Microw. Opt. Technol. Lett.*, vol. 51, no. 8, pp.1923-1934, Aug. 2009.

[3] R. Coifman, V. Rokhlin, and S.Wandzura, "The Fast Multipole Method for the Wave Equation: A Pedestrian Prescription," *IEEE Antennas Propag. Mag.*, vol. 35, no. 3, pp. 7-12, Jun. 1993.

[4] W. C. Chew, J. M. Jin, E. Michielssen, and J. M. Song, *Fast and Efficient Algorithms in Computational Electromagnetics*. Norwood, MA: Artech House, 2001

[5] H. Zhao, J. Hu, and Z. Nie, "Parallelization of MLFMA with Composite Load Partition Criteria and Asynchronous Communication," *Applied Computational Electromagnetic Society (ACES) Journal*, vol. 25, no. 2, pp. 167-173, 2010.

[6] H. Fangjing, Z. Nie, and J. Hu, "An Efficient Parallel Multilevel Fast Multipole Algorithm for Large-Scale Scattering Problems," *Applied Computational Electromagnetic Society (ACES) Journal*, vol. 25, no. 4, pp. 381-387, 2010.

[7] V. Jandhyala, "Fast Multilevel Algorithms for the Efficient Electromagnetic Analysis of Quasi-Planar Structures," Ph.D. Dissertation, Dept. Elect. Comput. Eng., Univ. Illinois, Urbana, 1998.

[8] V. Jandhyala, B. Shanker, E. Michielssen, and W. C. Chew, "A Fast Algorithm for the Analysis of Scattering by Dielectric Rough Surfaces," *J Opt Soc Amer A, Opt Image Sci*, vol. 15, pp. 1877-1885, 1998.

[9] V. Jandhyala, B. Shanker, E. Michielssen, and W. C. Chew, "A Fast Algorithm for the Analysis of Radiation and Scattering from Microstrip Arrays on Finite Substrates," *Microw Opt Techno Let*,. vol. 23, no. 5, pp. 306-310, Dec. 1999.

[10] N. Geng, A. Sullivan, and L. Carin, "Multilevel Fast-Multipole Algorithm for Scattering from Conducting Targets above or Embedded in a Lossy Half Space," *IEEE Trans. Geosci. Remote Sensing.*, vol. 38, pp.1561-1573, Jul. 2000.

[11] Z. Liu, J. He, Y. Xie, A. Sullivan, and L. Carin, "Multilevel Fast Multipole Algorithm for General Targets on a Half-Space Interface," *IEEE Trans. Antennas Propag.*, vol. 50, no. 12, pp. 1838-1849, Dec. 2002.

[12] R. S. Chen, Y. Q. Hu, Z. H. Fan, D. Z. Ding, D. X. Wang, and E. K. N. Yung, "An Efficient Surface Integral Equation Solution to EM Scattering by Chiral Objects above a Lossy Half Space," *IEEE Trans. Antennas Propag.*, vol. 57, no. 11, pp. 3586-3593, Nov. 2009.

[13] L. B. Felsen and N. Marcuvitz, *Radiation and Scattering of Waves. Piscataway*, NJ: IEEE Press, 1996, ch. 4.

[14] Y. Q. Hu, R. S. Chen, D. Z. Ding, and J. Q. Liu, "MLFMA Analysis of Scattering by Conducting Objects above a Lossy Half-Space," *8th International Symposium on Antennas Propag and EM Theory* pp.736-739, 2008.

[15] S. Kapur and D. E. Long, "IES3: A Fast Integral Equation Solver for Efficient 3-Dimensional

Extraction," *Proc. IEEE/ACM Int. Conf. Computer-Aided Design (ICCAD)*, San Jose, CA, pp. 448-455, 1997.

[16] W. Hackbusch and B. N. Khoromskij, "A Sparse H-Matrix Arithmetic, Part II: Application to Multidimensional Problems," *Computing*, vol. 64, pp. 21-47, 2000.

[17] M. Bebendorf and S. Rjasanow, "Adaptive Low-Rank Approximation of Collocation Matrices," Computing, vol. 70, pp. 1-24, 2003.

[18] L. Tsang, Q. Li, P. Xu, D. Chen, and V. Jandhyala, "Wave Scattering with UV Multilevel Partitioning Method: 2. Three-Dimensional Problem of Nonpenetrable Surface Scattering," *Radio Sci.*, vol. 39, p. RS5011, 2004.

[19] A. Heldring, J. M. Rius, and J. M. Tamayo, "Comments on Fast Direct Solution of Method of Moments Linear System," *IEEE Trans. Antennas Propag.*, vol 58, no. 3, pp. 1015-1016, Mar. 2010.

[20] M. I. Aksun, "A Robust Approach for the Derivation of Closed-Form Green's Functions," *IEEE Tran. Microwave Theory Tech.*, vol. 44, no. 5, pp. 651-658, May 1996.

[21] C. -J. Ong and L. Tsang, "Full-Wave Analysis of Large-Scale Interconnects using the Multilevel UV Method with the Sparse Matrix Iterative Approach (SMIA)," *IEEE Trans. Adv. Packag.*, vol. 31, no. 4, pp. 818-829, Nov. 2008.

[22] M. M. Li, J. J. Ding, D. Z. Ding, Z. H. Fan, and R. S. Chen, "Multiresolution Preconditioned Multilevel UV Method for Analysis of Planar Layered Finite Frequency Selective Surface," *Microw. Opt. Tech. Lett.*, vol. 52, no. 7, pp. 1530-1536, Jul. 2010.

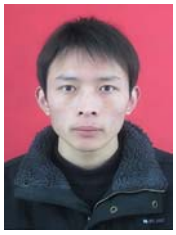

Meng-Meng Li was born in Jiangsu Province, the People's Republic of China in 1984. He received the B.S. degree in Physics from Huaiyin normal college in 2007, and is currently working toward the Ph.D. at Nanjing University of Science and Technology. His research interests focus on fast solution of integral equations, model order reduction in FEM, modeling of microwave integrated circuits, and UWB antennas.

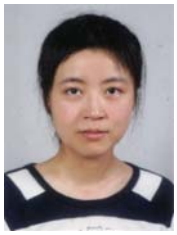

Hua Chen was born in Anhui Province, the People's Republic of China. She received the B.S. degree in Electronic Information Engineering from Anhui University, China, in 2005, and is currently working toward the Ph.D. at Nanjing University of Science and Technology (NJUST), Nanjing, China. Her current research interests include computational electromagnetics, antennas and electromagnetic scattering and propagation, electromagnetic modeling of microwave integrated circuits.

Chunyan Li was born in Jiangsu Province, the People's Republic of China. She received the B.S. degree in Electronic Information Engineering from Nanjing University of Science and Technology in 2009, and is currently working toward the master degree at Nanjing University of Science and Technology. Her research interests focus on fast solution of integral equations, model order reduction in FEM

Ru-Shan Chen (M'01) was born in Jiangsu, P. R. China. He received his B.Sc. and M.Sc. degrees from the Dept. of Radio Engineering, Southeast University, in 1987 and in 1990, respectively, and his Ph.D. from the Dept. of Electronic Engineering, City University of Hong Kong in 2001. He joined the Dept. of Electrical Engineering, Nanjing University of Science & Technology (NJUST), where he became a Teaching Assistant in 1990 and a Lecturer in 1992. Since September 1996, he has been a Visiting Scholar with Department of Electronic Engineering, City University of Hong Kong, first as Research Associate, then as a Senior Research Associate in July 1997, a Research Fellow in April 1998, and a Senior Research Fellow in 1999. From June to September 1999, he was also a Visiting Scholar at Montreal University, Canada. In September 1999, he was promoted to Full Professor and Associate Director of the Microwave & Communication Research Center in NJUST and in 2007, he was appointed Head of the Dept of Communication Engineering, Nanjing University of Science & Technology. His research interests mainly include microwave/millimeter-wave systems, measurements, antenna, RF-integrated circuits, and computational electromagnetics. He is a Senior Member of the Chinese Institute of Electronics (CIE). He received the 1992 third-class science and technology advance prize given by the National Military Industry Department of China, the 1993 third class science and technology advance prize given by the National Education Committee of China, the 1996 second-class science and technology advance prize given by the National Education Committee of China, and the 1999 first-class science and technology advance prize given by JiangSu Province as well as the 2001 second-class science and technology advance prize. At NUST, he was awarded the Excellent Honor Prize for academic achievement in 1994, 1996, 1997, 1999, 2000, 2001, 2002, and 2003. He has authored or co-authored more than 200 papers, including over 140

papers in international journals. He is the recipient of the Foundation for China Distinguished Young Investigators presented by the National Science Foundation (NSF) of China in 2003. In 2008, he became a Chang-Jiang Professor under the Cheung Kong Scholar Program awarded by the Ministry of Education, China.

Chong-Jin Ong was born in Singapore. He received the B.Eng. (with first class honors) and the M.Eng. degrees in Electrical Engineering from the National University of Singapore, in 1994 and 1999, respectively, and the Ph.D. degree in Electrical Engineering from the University of Washington, Seattle, in 2007. From 1994 to 2001, he was an Antenna Engineer at the DSO National Laboratories in Singapore. In the summer and autumn of 2002, he was a Graduate Technical Intern at the Intel Corporation, Hillsboro, OR. In the summers of 2003 and 2004, he was a Graduate Technical Intern at the Intel Corporation, Dupont, WA. In 2007, he joined the Memory Products Group of Micron Technology, Inc., as a Signal Integrity Engineer. His current interests are in package signal integrity and electromagnetic simulations.

An Alternative Multiresolution Basis in EFIE for Analysis of Low-Frequency Problems

Jianjun Ding, Jian Zhu, Ru-shan Chen, Z. H. Fan, and K. W. Leung

Department of Electronic Engineering
Nanjing University of Science and Technology, Nanjing, 210094, China
draksea@yahoo.com, zhujian82gogo@hotmail.com, eerschen@mail.njust.edu.cn,
zhfan@mail.njust.edu.cn, eekleung@cityu.edu.hk

Abstract ─ An alternative multiresolution (MR) basis is presented for the method-of-moments (MoM) solution of the electric-field integral equation (EFIE) for the analysis of low-frequency problems. The proposed MR basis functions can be treated as an extension of the traditional loop-tree basis function to hierarchical functions. Similar to the loop-tree basis, the MR basis functions are linear combinations of standard Rao-Wilton-Glisson (RWG) functions. Therefore, the MR algorithm can be easily applied to MoM codes with RWG basis. Since the MR basis is immune from the so-called low-frequency breakdown, the MR basis is especially suitable for the analysis of low-frequency problems. Compared with the previous MR basis, the present MR basis is easier to construct and comprehend, and the basis-changing matrix is sparser. Physical interpretation and comparison are given for the previous and present MR bases. Numerical results demonstrate that both the previous and present MR bases are efficient for 3D electromagnetic scattering problems at low frequencies.

Index Terms ─ EFIE, electromagnetic scattering, low frequency, method of moments (MoM), multiresolution techniques.

I. INTRODUCTION

The method of moments (MoM) is one of the most powerful numerical methods applicable to a wide variety of practical electromagnetic radiation and scattering problems [1, 2]. The electric field integral equation (EFIE) is always preferred in MoM. However, the EFIE suffers the so called low-frequency breakdown problem which occurs when the harmonic field wavelength is substantially larger than the characteristic size of the MoM grid. An effective solution to this problem is to separate the solenoidal part of the current [3-11]. The loop-star basis and loop-tree basis are proposed in the early 1980s [3, 4]. Both of them introduce divergence-free loop functions which can effectively separate the solenoidal part of the current. The detailed discussion and application of the loop-star basis and loop-tree basis can be found in [5-9], and a comparison of the frequency dependent iterative solver convergence for RWG, loop-tree, and loop-star basis functions is given in [10].

In recent years, the multiresolution (MR) basis has been proposed and acted as an efficient physics-based preconditioner [12-27]. Compared with the loop-star/tree basis, the MR basis has a much faster MoM convergence rate when an iterative solver is applied. The reasons why the MR basis can positively act on the spectrum of a MoM matrix has been investigated and discussed in [20, 21]. The MR basis was first mentioned by G. Vecchi in [7], where he pointed out that a MR basis can be efficiently constructed to replace the loop-star basis. Consequently, a MR basis was proposed in [12]. Then a modified MR basis was proposed in [13] to simplify the generation procedure. However, the MR bases in [12, 13] has a limit in modeling the curved structures, since the shape of the hierarchical meshes is restricted by the coarse mesh. To remedy this drawback of MR basis, a curvilinear MR basis is proposed in [15]. More recently, a new MR algorithm was proposed in [16-19] to overcome the shortcoming of the MR basis defined over triangular patches. In the new MR algorithm, the concepts of generalized mesh and generalized RWG (gRWG) basis were introduced. The generalized mesh is generated by

a grouping algorithm. The gRWG basis is the generalization of the standard RWG basis and it is defined on the generalized meshes. The new MR basis functions are constructed as linear combinations of gRWG basis functions and can finally be represented by linear combinations of the RWG basis functions.

Inspired by the novel idea of generalized mesh and generalized RWG basis, an alternative MR basis is proposed in this paper which is also defined on the generalized meshes. Contrary to the MR algorithm in [16-19] which relies on mathematical operations, the MR basis proposed in this paper is generated via geometric operations. Compared with the previous MR basis, the proposed MR basis can be constructed in a much easier fashion and provide more direct physical meanings. Also, the basis-changing matrix of the RWG basis functions to the MR basis functions is sparser and can be generated faster. Furthermore, physical interpretations are provided for both MR bases and the number of MR basis functions of each level is clearly given which explains why the MR bases span the same space as the RWG basis. Numerical examples demonstrate that the MR bases have a much faster convergence rate for iterative solvers than the traditional loop-tree basis as explained in [20, 21].

This paper is organized as follows. Section II introduces the hierarchical generalized meshes and the gRWG basis. Section III gives a detailed description of the MR basis generation. Section IV provides physical interpretations for the MR bases. A discussion on the computational complexity of the MR basis is given in Section V. Section VI presents numerical results to validate and demonstrate the performance of the MR basis. Finally, the work is concluded in Section VII.

II. GENERALIZED MESH AND GRWG BASIS

Before discussing the new MR basis, the essential concepts of the generalized mesh and gRWG basis are briefly described as preliminary knowledge. Since the detailed generation algorithm of the generalized mesh and gRWG basis has already been given in [17, 18], only a brief description is provided in this section.

A. Hierarchical generalized meshes

Generation of the hierarchical generalized meshes starts from an input triangular mesh which is called level-0 mesh and denoted by M^0. Using a grouping algorithm, the nearby cells of the level-0 mesh are grouped into level-1cells. The union of the level-1 cells is called level-1 mesh, M^1. Applying the same grouping algorithm to the level-1 cells will generate the level-2 mesh (M^2) and so on and a set of hierarchical generalized meshes $\{M^l,\ l = 1, \ldots, L\}$ will be obtained. The last level L is usually decided by the maximum size of the generated cells that should be smaller than the wavelength, with a typical range of $\lambda/8 - \lambda/4$. To demonstrate the grouping algorithm, the hierarchical generalized meshes of a circular plate are shown in Fig. 1.

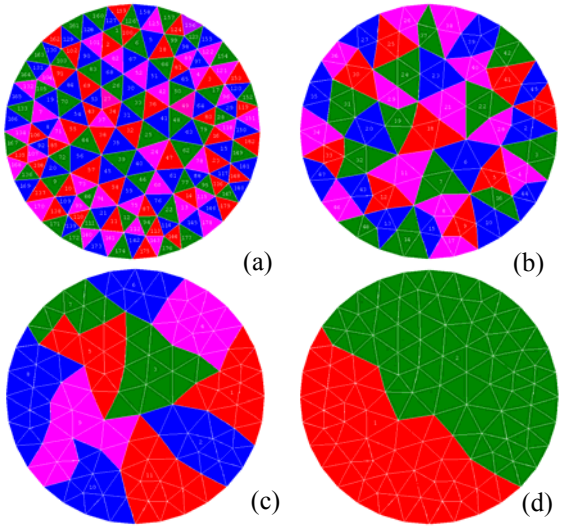

Fig. 1. An example of hierarchical generalized meshes on a circular plate. (a) level-0 mesh, (b) level-1 mesh, (c) level-2 mesh, (d) level-3 mesh.

B. Generalized RWG basis

Similar to the definition of the RWG basis, a gRWG basis function is defined on a pair of adjacent cells of its corresponding level. Denoting a level-l gRWG basis function as $\bar{R}_i^l(\bar{r})$, its divergence is given as

$$\nabla_s \cdot \bar{R}_i^l(\bar{r}) = \begin{cases} \ell_i^l / A_{+,i}^l & \bar{r} \in C_{+,i}^l \\ -\ell_i^l / A_{-,i}^l & \bar{r} \in C_{-,i}^l \\ 0 & \text{otherwise,} \end{cases} \quad (1)$$

where $A_{+,i}^l$ and $A_{-,i}^l$ are the areas of the two adjacent cells ($C_{+,i}^l$, $C_{-,i}^l$), and ℓ_i^l is the length of the level-*l* generalize edge shared by the two cells and is a polygonal line in general.

C. Inter-mesh reconstruction relationship

The inter-mesh reconstruction relationship can be derived through the charge matrix. In the inter-mesh reconstruction relationship, a level-*l* *g*RWG function $\vec{R}_i^l(\vec{r})$ can be expressed as the linear combination of the level-(*l*-1) gRWG functions $\vec{R}_n^{l-1}(\vec{r})$ (n = 1,…, N_i^{l-1}) which are completely defined in the domain $C_{+,i}^l \cup C_{-,i}^l$ of $\vec{R}_i^l(\vec{r})$, i.e.

$$\vec{R}_i^l(\vec{r}) = \sum_{n=1}^{N_i^{l-1}} R_{n,i}^l \vec{R}_n^{l-1}(\vec{r}), \tag{2}$$

where $R_{n,i}^l$ is the reconstruction coefficient. Applying the surface divergence to both sides of (2), we have

$$\nabla_s \cdot \vec{R}_i^l(\vec{r}) = \sum_{n=1}^{N_i^{l-1}} R_{n,i}^l \nabla_s \cdot \vec{R}_n^{l-1}(\vec{r}). \tag{3}$$

Projecting (3) on the cells C_m^{l-1} (m = 1, …, $N_{c,i}^{l-1}$) in the domain of $\vec{R}_i^l(\vec{r})$, a linear system can be obtained as

$$\left[Q_i^l\right] \cdot \left[R_i^l\right] = \left[q_i^l\right], \tag{4}$$

where $\left[Q_i^l\right]$ is the $N_{c,i}^{l-1} \times N_i^{l-1}$ charge matrix whose element is given by

$$\left[Q_i^l\right]_{m,n} = \nabla_s \cdot \vec{R}_n^{l-1}(\vec{r})\Big|_{C_m^{l-1}},$$

$$\left[R_i^l\right] = \left[R_{1,i}^l, R_{2,i}^l, \ldots, R_{N_i^{l-1},i}^l\right]^T, \ \left[q_i^l\right]_m = \nabla_s \cdot \vec{R}_n^l(\vec{r})\Big|_{C_m^{l-1}}.$$

As will be discussed in the next section, the maximum number of the linear independent functions $\vec{R}_n^{l-1}(\vec{r})$ (n = 1,…, N_i^{l-1}) is $N_{c,i}^{l-1} - 1$ according to Euler's theorem. Therefore, the rank of the matrix $\left[Q_i^l\right]$ is $N_{c,i}^{l-1} - 1$ and a full row rank matrix $\left[\tilde{Q}_i^l\right]$ can be obtained by deleting an arbitrary row of $\left[Q_i^l\right]$. When $N_{c,i}^{l-1} - 1 < N_i^{l-1}$, the matrix equation (4) has infinitely many solutions and the least squares solution can be taken as the reconstruction coefficients $\left[R_i^l\right]$, i.e.

$$\left[R_i^l\right] = \left[\tilde{Q}_i^l\right]^+ \left[q_i^l\right], \tag{5}$$

where $\left[\tilde{Q}_i^l\right]^+$ is the Moore-Penrose pseudoinverse of $\left[\tilde{Q}_i^l\right]$.

III. MR BASIS GENERATION

For a general 3-D surface (without torus), the Euler's theorem states that [9, 19]

$$V + F = E - N_\Gamma + 2, \tag{6}$$

where V, E, F, N_Γ denote the number of vertices, edges, faces, and separated boundary contours, respectively. Since the number of vertices and edges on the boundary contours is equal, we have

$$V_{\text{int}} + F = E_{\text{int}} - N_\Gamma + 2, \tag{7}$$

where V_{int}, E_{int} is the number of internal vertices and edges, respectively.

For a domain (e.g. a cell or a pair of cells of level-*l*) composed of $N_{c,i}^{l-1}$ cells of level-(*l*-1), we have

$$N_i^{l-1} - (V_{\text{int}} + N_\Gamma - 1) = N_{c,i}^{l-1} - 1. \tag{8}$$

N_i^{l-1} is the number of the gRWG functions in the domain, since the gRWG functions are defined on the interior edges. If connecting all the cells in a tree (see e.g. Fig. 2) and avoid forming any loop on the tree, then the maximum number of edges on the tree will be $N_{c,i}^{l-1} - 1$. Obviously, the gRWG functions corresponding to the edges on the tree are linear independent. Therefore, the maximum number of the linear independent gRWG functions in the domain is equal to $N_{c,i}^{l-1} - 1$.

If the surface is discretized with triangles, the number of solenoidal functions N_S and the number of nonsolenoidal functions N_X of loop-star basis are given by [7, 9]

$$N_S = V_{\text{int}} + N_\Gamma - 1 \tag{9}$$

$$N_X = F - 1. \tag{10}$$

Their sum is equal to the number of the RWG functions, i.e.

$$N_S + N_X = N, \tag{11}$$

where N is the number of the RWG functions.

Similar to loop-star/tree basis, the MR basis can also be split into the solenoidal and nonsolenoidal parts. It will be shown in the next section that the solenoidal and nonsolenoidal functions of the MR basis span the same space as for the loop-tree/star basis, and the numbers of the solenoidal and nonsolenoidal functions of the MR basis can also be given by equations (9)-(11).

A. Solenoidal basis

It has already been shown in [17] that the use of a hierarchical decomposition of the nonsolenoidal part together with a non hierarchical loop basis suffices to obtain well conditioned MoM matrices and, hence, quickly convergent solvers for low-frequency and very dense discretizations. The difference between the low-frequency and very dense discretization is addressed in [11]. Therefore, for simplicity, the loop basis generated on level-0 mesh is chosen as the solenoidal part of the MR basis. The detailed discussion of the loop basis can be found in [7, 9], whereas the topic of generating the loop basis functions on the more complex surfaces (e.g. wire-surface structure) can be found in [28].

After generating the loop basis, the solenoidal basis of the MR basis can be written as

$$\left[\vec{f}_L\right]=\left[T_L\right]^T\left[\vec{R}^0\right], \tag{12}$$

where $\left[\vec{f}_L\right]^T=\left[\vec{f}_{1,L},\vec{f}_{2,L},\ldots,\vec{f}_{N_S,L}\right]$ is the solenoidal MR basis, $\left[T_L\right]$ is the basis-changing matrix, and $\left[\vec{R}^0\right]^T=\left[\vec{R}_1^0,\vec{R}_2^0,\ldots,\vec{R}_N^0\right]$ is the RWG basis of level-0 mesh.

B. Nonsolenoidal basis

The nonsolenoidal basis is defined on the hierarchical generalized meshes. The nonsolenoidal basis functions of the highest level (level-*L*) are different from the nonsolenoidal basis functions of other levels (level-*l*, l = 1, …, *L*-1). Therefore, the nonsolenoidal basis functions of level-*L* are generated separately from the function of the other levels.

1). Nonsolenoidal functions of level-L

The generation of the nonsolenoidal functions of level-*L* is similar to that of the tree basis functions in loop-tree basis. The only difference is that the cells of level-*L* are replaced by triangles. An easy procedure of constructing the nonsolenoidal functions of level-*L* is to connect the cells of the level-*L* mesh in a tree, and each gRWG basis function on the branch of the tree is taken as a nonsolenoidal function. To demonstrate this procedure, the nonsolenoidal functions defined on the level-2 mesh (Fig. 1) are plotted. In this example, it is assumed that level-2 mesh is of the highest level. As shown in Fig. 2 (a), each black line connecting a pair of cells represents a generated nonsolenoidal function. It is worth mentioning that the number of the nonsolenoidal functions of level-*L* equals the number of the cells of level-*L* minus one.

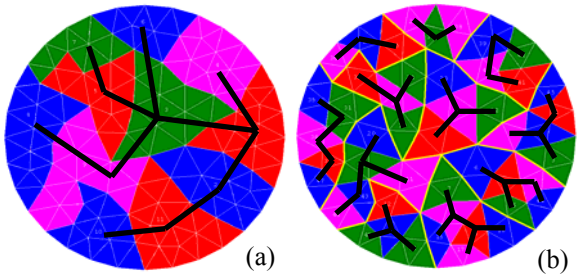

Fig. 2. The nonsolenoidal functions, which are depicted with black lines, on a circular plate. (a) Level-2 functions, (b) level-1 functions.

2). Nonsolenoidal functions of level- l (l = 1, …, L-1)

Let the nonsolenoidal functions of level-*l* belong to the cell C_k^{l+1} of level-(*l*+1) denoted with $\left\{\vec{f}_{k,i}^{\,l}, i=1,\cdots,N_{C_k^{l+1}}^l-1\right\}$, in which $N_{C_k^{l+1}}^l$ is the number of the cells of level-*l* belonging to the cell C_k^{l+1}, the nonsolenoidal functions of level-*l* can be expressed as the union of the nonsolenoidal functions that belong to all the cells of level-(*l*+1), i.e.

$$\left\{\vec{f}_{j,X}^{\,l}, j=1,\cdots,N_c^l-N_c^{l+1}\right\}=\bigcup_{k=1}^{N_c^{l+1}}\left\{\vec{f}_{k,i}^{\,l}, i=1,\cdots,N_{C_k^{l+1}}^l-1\right\}, \tag{13}$$

where N_c^l and N_c^{l+1} are the numbers of the cells of level-*l* and level-(*l*+1) respectively, and $N_c^l-N_c^{l+1}$ is the number of the nonsolenoidal functions of level-*l*. A simple way of generating the level-*l* nonsolenoidal functions in the cell C_k^{l+1} is to connect all the level-*l* cells which are completely included in the cell C_k^{l+1} in a tree and taking the gRWG basis functions on the branches of the tree as nonsolenoidal functions. An example of level-1 nonsolenoidal functions is shown in Fig. 2 (b). As can be observed from Fig. 2 (b), the level-2 cells are bounded with yellow lines and the level-1 nonsolenoidal functions are clustered in each level-2 cell shown with black lines.

The nonsolenoidal functions (13) can be written as linear combinations of the gRWG basis functions of level-*l*, i.e.

$$\left[\vec{f}_X^{\,l}\right] = \left[T'^{\,l}_{\ X}\right]^T \left[\vec{R}^l\right], \tag{14}$$

where $\left[\vec{f}_X^{\,l}\right]^T = \left[\vec{f}^{\,l}_{1,X}, \vec{f}^{\,l}_{2,X}, \ldots, \vec{f}^{\,l}_{N_c^l - N_c^{l+1},X}\right]$, $\left[T'^{\,l}_{\ X}\right]^T$ is the basis-changing matrix, and $\left[\vec{R}^l\right]^T = \left[\vec{R}^l_1, \vec{R}^l_2, \ldots, \vec{R}^l_{N^l}\right]$ is the gRWG basis of level-*l*. Applying the inter-mesh reconstruction relationship (2) recurrently, the nonsolenoidal functions of level-*l* can then be written as linear combinations of the RWG basis functions of level-0 mesh, i.e.,

$$\left[\vec{f}_X^{\,l}\right] = \left[T_X^l\right]^T \left[\vec{R}^0\right]. \tag{15}$$

Then, the nonsolenoidal functions of all levels can be written as

$$\left[\vec{f}_X\right] = \left[T_X\right]^T \left[\vec{R}^0\right], \tag{16}$$

where $\left[\vec{f}_X\right]^T = \left[\left[\vec{f}_X^{\,0}\right]^T, \left[\vec{f}_X^{\,1}\right]^T, \cdots, \left[\vec{f}_X^{\,L}\right]^T\right]$ and $\left[T_X\right]^T = \left[\left[T_X^0\right]^T, \left[T_X^1\right]^T, \cdots, \left[T_X^L\right]^T\right]$.

Finally, the MR basis functions can be expressed in terms of the RWG basis functions as follows

$$\left[\vec{f}_{MR}\right] = \left[T\right]^T \left[\vec{R}^0\right], \tag{17}$$

where $\left[T\right] = \left[\left[T_L\right], \left[T_X\right]\right]$.

IV. PHYSICAL INTERPRETATION OF MR BASES

Although the generation algorithm of the MR basis proposed in [18, 19] is clearly given, the physical meaning behind it is not clearly pointed out. Readers may also be confused about why the number of the MR basis functions equals the number of the RWG basis functions. Therefore, physic interpretations are tried to give in this section for both the present MR basis and the previous MR basis for better understanding of the MR bases.

A. The present MR basis

From the discussion given in Section III-B, the total number of the nonsolenoidal functions can be calculated as

$$\begin{aligned} N_X &= N_X^0 + N_X^1 + \cdots + N_X^L \\ &= (F - N_c^1) + (N_c^1 - N_c^2) + \cdots + (N_c^L - 1) \cdot \\ &= F - 1 \end{aligned} \tag{18}$$

Therefore, the numbers of the nonsolenoidal functions of the MR basis also satisfy (10). Similar to the loop-tree/star basis, it can be easily proven that all the solenoidal and nonsolenoidal functions of the present MR basis are linear independent from each other. Therefore, the MR basis spans the same space as for the loop-star/tree basis.

B. The previous MR basis

The previous MR basis functions proposed in [18, 19] are constructed via SVD on charge matrices. After applying SVD on a charge matrix, the right singular vectors associated to non-zero and null singular values are assigned as the coefficients of the corresponding gRWG function to generate the solenoidal and nonsolenoidal MR functions respectively. However, the reason is not explained. In the following, a physical explanation to the above mathematical operations is given. Assuming a charge matrix generated by projecting *n* level-*l* gRWG functions onto *m* level-*l* cells, then its SVD result can be written as

$$\begin{aligned} [Q] &= \left[\nabla \cdot R_1, \nabla \cdot R_2, \cdots, \nabla \cdot R_n\right] = [U] \cdot [\Sigma] \cdot [V]^T \\ &= \left[U_1, U_2, \cdots, U_m\right] \cdot diag(\sigma_1, \sigma_2, \cdots, \sigma_{m-1}) \\ &\quad \left[V_1, V_2, \cdots, V_n\right]^T, \end{aligned} \tag{19}$$

where $\sigma_1 \geq \sigma_2 \geq \cdots \geq \sigma_{m-1} > 0$, since the rank of $[Q]$ is *m*-1. The expression (19) can be rewritten as

$$\begin{aligned} &\nabla \cdot \left[R_1, R_2, \cdots, R_n\right] \cdot \left[V_1, V_2, \cdots, V_n\right] = \\ &\left[\sigma_1 U_1, \sigma_2 U_2, \cdots, \sigma_{m-1} U_{m-1}, 0 \cdot U_m, \cdots, 0 \cdot U_n\right] \end{aligned}. \tag{20}$$

It can be inferred from (20) that the gRWG functions multiplies the first *m*-1 columns of $[V]$ generates *m*-1 linear independent functions which have surface charge and can be taken as the nonsolenoidal functions. Therefore, the number of the nonsolenoidal functions generated with the algorithm in [17, 18] can also be given by (18). Namely, the numbers of the MR nonsolenoidal functions in the present paper and in [17, 18] are equal. It can also be inferred from (20) that the gRWG functions multiplies the other *n*-*m* columns of $[V]$ generates *n*-*m* linear independent functions which have no surface charge and can be taken as the solenoidal functions.

It can be inferred from the discussion at the beginning of Section III that the number of the level-*l* solenoidal functions in a level-(*l*+1) cell (except the level-*L* cell of closed surfaces which

has no boundary) equals the number of the interior vertexes shared by the *level-l* edges inside the level-(l+1) cell. Furthermore, the number of the level-l solenoidal functions added by generating solenoidal functions across a pair of level-(l+1) cells equals the number of the interior vertexes which connecting the level-l edges that coincide with the common edge of the two level-(l+1) cells. Therefore, the total number of the MR basis functions generated in [18, 19] can be finally described by (21). It can be proven by theorem 1 that the number of the MR basis functions equals the number of the RWG basis functions of the input mesh.

Theorem 1 *The number of the RWG basis functions of the input mesh can be written as the sum of the following elements:*

$$N = \sum_{l=0}^{L} N_e^l + \sum_{l=1}^{L} \left(\sum_{n=1}^{N_e^l} N_{v,n}^l \right), \tag{21}$$

where N_e^l *(l=L) is the number of the level-L interior edges and* $N_e^l = \sum_{m=1}^{N_c^{l+1}} N_{e,m}^l$ *(0⩽l<L-1) is the total number of the level-l interior edges inside all level-(l+1) cells, in which* $N_{e,m}^l$ *is the number of the level-l edges inside the m-th level-(l+1) cell and* N_c^{l+1} *is the number of level-(l+1) cells, and* $N_{v,n}^l$ *is the number of the interior vertexes on the n-th level-l interior edges.*

Proof: The expression (21) can be interpreted by the changes of the interior edges of each level in the procedure of generating the hierarchical meshes. In the first step of the mesh generating procedure, the level-1 mesh is generated from the input mesh (level-0) and parts of the level-0 interior edges are grouped into the level-1 interior edges. Since the number of the level-0 interior edges grouped into one level-1 interior edge equals the number of the level-0 interior vertexes on the level-1 interior edge plus one, the total number of the grouped level-0 interior edges equals the total number of level-0 interior vertexes on the level-1 interior edges plus the number of the level-1 interior edges. Namely, the number of the level-0 interior edges can be decomposed as the sum of the total number of the level-0 interior edges inside all level-1 cells (i.e. the number of the left level-0 interior edges), the total number of level-0 interior vertexes on the level-1 interior edges, and the number of the level-1 interior edges. Similarly, the number of the level-l ($1 \leqslant l<L$-1) interior edges can be decomposed as the sum of the total number of the level-l interior edges inside all level-(l+1) cells, the total number of level-l interior vertexes on the level-(l+1) interior edges, and the number of the level-(l+1) interior edges. As a consequence, the number of the level-0 interior edges can be finally written as (21). Since each RWG basis function of the input mesh is corresponding to a level-0 interior edge, theorem 1 is proven.

It can be inferred from the above discussion that the number of the solenoidal and nonsolenoidal functions of the previous MR basis functions can also be given by equations (9)-(11). The level-L functions of the previous MR basis should be constructed independently if the cells are not finally grouped into one big cell. The level-L functions of the previous MR basis could be generated by applying SVD on the charge matrix generated by projecting the level-L gRWG functions on the level-L cells or simply taking the level-L gRWG basis functions as the level-L MR basis functions. It can also be inferred from Theorem 1 that the solenoidal part of the present MR basis can be constructed as a hierarchical basis in which each solenoidal function is generated as a linear combination of the gRWG functions of the same level which constitute a loop around an interior vertex.

V. COMPUTATIONAL COMPLEXITY

Since the computational complexity of the loop basis is known as $O(N)$ [28], only the computational complexity of the nonsolenoidal MR basis is needed to be analyzed. The computational complexity of the nonsolenoidal MR basis can be estimated by estimating the number of on-zero elements of the basis-changing matrix [T].

The number of non-zero elements of the basis-changing matrix [T] as the functions of the number of levels of a structure discretized with 19090 unknowns is investigated and shown in Fig. 3. It can be observed from Fig. 3 that the number of non-zero elements of matrix [T] increase linearly with the number of the levels of the MR basis. Therefore, the computational complexity of the

nonsolenoidal MR basis is of $O(NL)$, where L is the number of levels. If keep grouping the cells of each level upwards until the cells are finally grouped into one single cell in the highest level mesh, the number of levels L will be equal to Log$N$ and the computational complexity will be of $O(N\text{Log}N)$. The number of non-zero elements and the generation time of matrix [T] as functions of the number of the unknowns for the previous MR basis and present MR basis when the cells are finally grouped into a single cell are investigated and shown in Fig. 4 (a) and (b), respectively. It can be observed from the figure that the computational complexity of both the previous and present MR basis is of $O(N\text{Log}N)$ and the computational complexity of the present MR basis has a smaller constant.

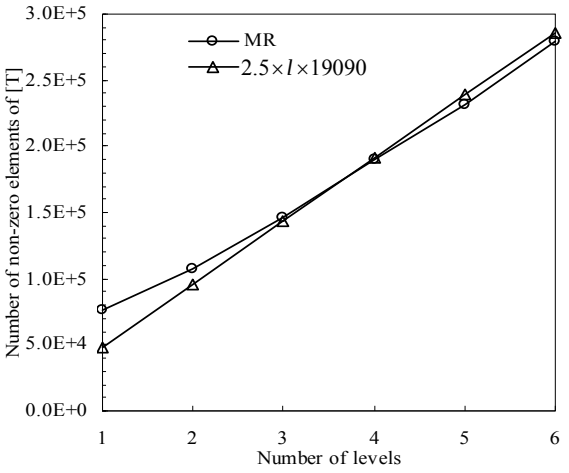

Fig. 3. The number of non-zero elements of the basis-changing matrix [T] versus the number of levels of a structure discretized with 19090 unknowns.

VI. NUMERICAL RESULTS

In this section, the MR basis is applied for the analysis of EM scattering problems at low frequencies. In the following examples, the restarted GMRES(30) algorithm is used as an iterative method. All simulations were performed on a PC computer with Intel(R) Core(TM)2 1.86 GHz CPU and 2 GB RAM using single precision. Zero vector is taken as initial approximate solution and the iteration process is terminated when the relative backward error is reduced by 10^{-4}. And all the results with different bases were obtained after applying a diagonal preconditioning to the MoM matrix.

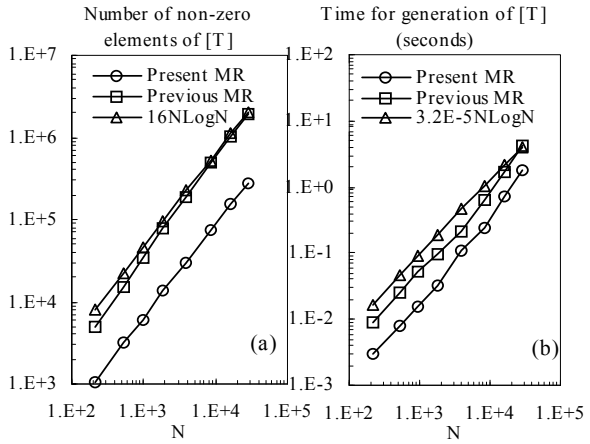

Fig. 4. (a) The number of non-zero elements of the basis-changing matrix [T], (b) the time for generation of matrix [T], versus the number of unknowns.

A. Offset bend rectangular cavity

The first example is a metallic offset bend rectangular cavity with 8.7 cm by 10 cm square cross section and offset angles 30°. As shown in Fig. 5, the offset bend rectangular cavity is discretized with 4317 unknowns. The mesh of the offset bend rectangular cavity could generate six levels hierarchical meshes and five levels MR basis at most. The EM scattering of the offset bend rectangular cavity is calculated with the EFIE using the RWG, loop-tree, the previous MR, and present MR bases. The 2-norm condition number and convergence behavior of GMRES(30) for the offset bend rectangular cavity using the above bases over a frequency range of 0.1-200 MHz is shown in Fig. 5 and Fig. 6, respectively. The corresponding total time for applying the MR bases is depicted in Fig. 7.

With reference to the figures, the RWG basis performs worse than both the loop-tree basis and MR bases in the low frequency range. It can be also found that the MR bases perform much better than the loop-tree basis in the low frequency range. The more levels of the present MR basis, the better it performs in the low frequency range. Comparing the previous MR basis with the present MR basis, it can be found that the present MR basis performs similar to the previous MR basis at low frequencies. However, the previous MR basis

performs more stable as the frequency increases. The corresponding total time which includes the time of the generation of the basis-changing matrix, the time of the generation of the diagonal preconditioning matrix, and the solution time of the GMRES(30) is depicted in Fig. 6. The result using the RWG basis is not given in Fig. 6 since the GMRES(30) solver cannot converge by using the RWG basis at some frequencies. It is also clearly indicates that the MR bases have better performance than the loop-tree basis at the low-frequency range.

The impact of the discretization density to the performance of different bases is investigated. The 2-norm condition number of the MoM matrices using the RWG basis, loop-tree basis, and the present and previous MR bases for the offset bend rectangular cavity discretized with different number of unknowns is shown in Fig. 8. It can be found from Fig. 8 that the MR bases perform more stable than the RWG basis and loop-tree basis as the discretization density increases and this result agrees with the results in [11].

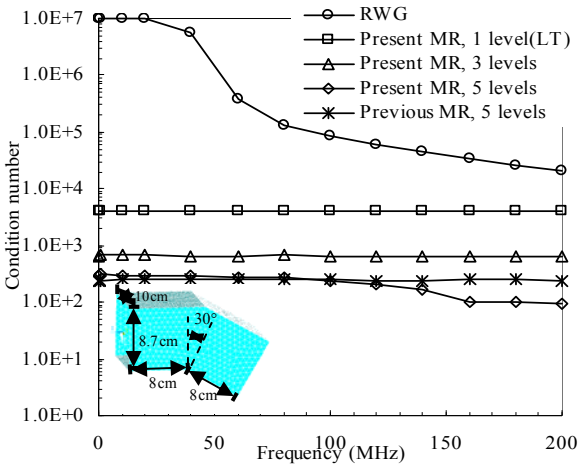

Fig. 5. The 2-norm condition number as a function of frequency for the offset bend rectangular cavity using the RWG, loop-tree, and MR bases.

B. Tank model

As shown in Fig. 9, the second example is a tank model discretized with 8706 unknowns. The length, width, and height of the tank model are 10.3 m, 3.3 m, and 2.3 m, respectively. To describe the shape of the tank model efficiently, the parts varying rapidly in geometry are discretized with relatively small triangular patches and the other parts are with large patches.

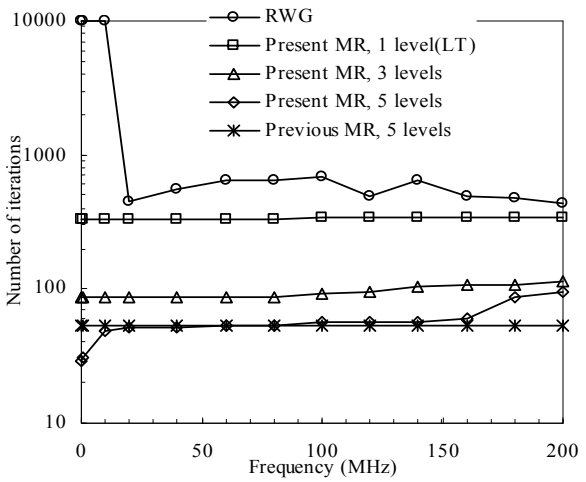

Fig. 6. The convergence behavior of GMRES(30) as a function of frequency for the offset bend rectangular cavity using the RWG, loop-tree, and MR bases.

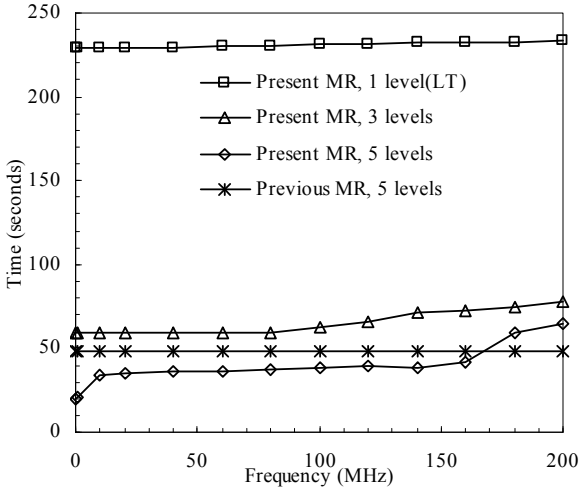

Fig. 7. The total time as a function of frequency for the offset bend rectangular cavity using the loop-tree and MR bases.

The convergence curves of the GMRES(30) are compared in Fig. 9 at the low frequency 1.0 MHz using the RWG, loop-tree and the MR bases. It can also be found from Fig. 9 that the convergence of the GMRES(30) using the MR bases which have higher levels is much faster than the others. The convergence behavior of GMRES(30) and the corresponding total time for applying the MR bases over a frequency range of

0.1-6 MHz is shown in Fig. 10 and Fig. 11, respectively. From Fig. 10 and Fig. 11 it can found that the both MR basis performs similar at lower frequencies and the previous MR performs more stable as the frequency increases.

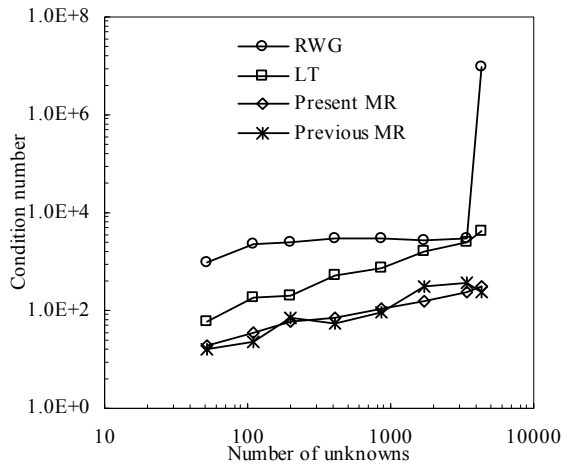

Fig. 8. The 2-norm condition number as a function of discretization density for the offset bend rectangular cavity using the RWG, loop-tree, and MR bases.

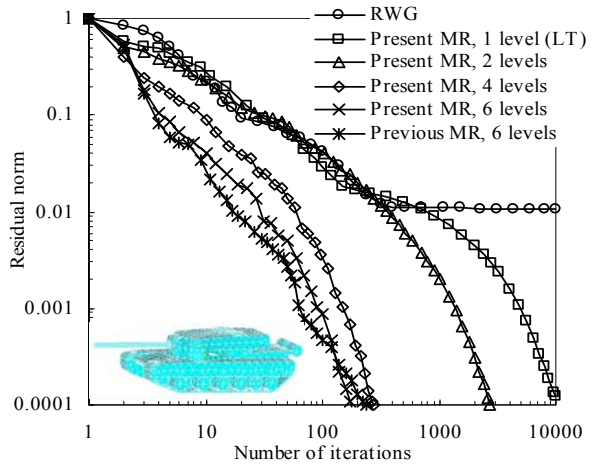

Fig. 9. The convergence history of the GMRES(30) for the tank model at 1.0 MHz using the RWG, loop-tree, and MR bases.

VII. CONCLUSION

An alternative MR basis has been proposed for analyzing low-frequency problems using the MoM. Contrary to the previous MR basis which is generated based on mathematical operations, the present MR basis is generated based on geometrical operations. The present MR basis is an extension of the loop-tree basis to hierarchical basis, and the loop-tree can be treated as a special one-level MR basis.

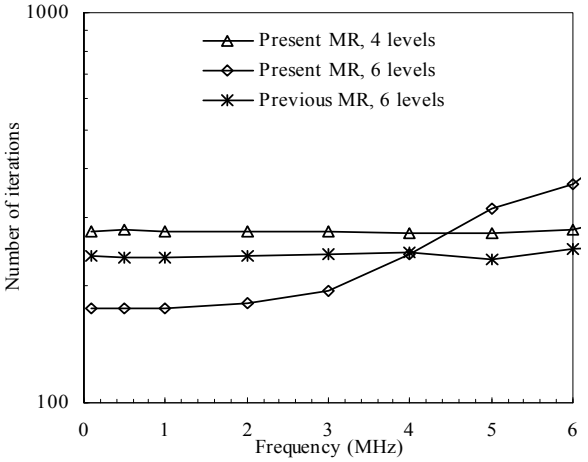

Fig. 10. The convergence behavior of GMRES(30) as a function of frequency for the tank model using the MR bases.

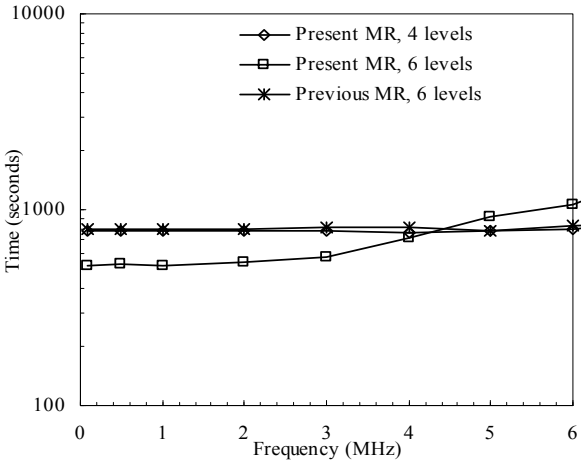

Fig. 11. The total time as a function of frequency for the tank model using the MR bases.

Therefore, the present MR basis is easier to construct and comprehend. Also, the computational complexity of the present MR basis is lower than that of the previous MR basis and the basis-changing matrix of the RWG basis to the present MR basis is sparser. As similar to the loop-tree basis, the present MR basis functions are combinations of RWG basis functions. Thus, the present MR basis can be easily applied to existing MoM codes. It has been demonstrated by the numerical results that the MR bases can be used to solve low-frequency EM scattering problems

efficiently. Compared with the traditional loop-tree basis, the MR bases converge much faster at low frequencies for iterative solvers. Although the present MR basis performs similar to the previous MR basis at lower frequencies, it should be pointed out that the present MR basis suffers the same drawback as the loop-tree basis, i.e. it will be unstable as the frequency goes higher. Therefore, the previous MR basis is recommended at higher frequencies since it performs more stable as the frequency increases.

ACKNOWLEDGMENT

The authors would like to thank the assistance and support of Major State Basic Research Development Program of China (973 Program: 2009CB320201), Natural Science Foundation of 60871013, 60701004, and 60928002, and Jiangsu Natural Science Foundation of BK2008048.

REFERENCES

[1] R. F. Harrington, *Field Computations by Moment Methods*, MacMillan, New York, 1968.

[2] S. M. Rao, D. R. Wilton, and A. W. Glisson, ‘‘Electromagnetic Scattering by Surfaces of Arbitrary Shape,’’ *IEEE Trans. Antennas Propagat.*, vol. AP-30, pp. 409-418, May 1982.

[3] D. R. Wilton and A.W. Glisson, “On Improving the Electric Field Integral Equation at Low Frequencies,” in *Proc. URSI Radio Science Meeting Dig.*, Los Angeles, CA, p. 24, June 1981.

[4] J. Mautz and R. F. Harrington, “An E-Field Solution for a Conducting Surface Small or Comparable to the Wavelength,” *IEEE Trans. Antennas Propagat.*, vol. AP-32, no. 4, pp. 330-339, April 1984.

[5] M. Burton and S. Kashyap, “A Study of a Recent Moment-Method Algorithm that is Accurate to Very Low Frequencies,” *Applied Computational Electromagnetic Society (ACES) Journal*, vol. 10, no. 3, pp. 58-68, Nov. 1995.

[6] W. L. Wu, A. Glisson, and D. Kajfez, “A Study of Two Numerical Solution Procedures for the Electric Field Integral Equation at Low Frequency,” *Applied Computational Electromagnetic Society (ACES) Journal*, vol. 10, no. 3, pp. 69-80, Nov. 1995.

[7] G. Vecchi, “Loop-Star Decomposition of Basis Functions in the Discretization of the EFIE,” *IEEE Trans. Antennas Propagat.*, vol. 47, no. 2, pp. 339-346, Feb. 1999.

[8] J. S. Zhao and W. C. Chew, “Integral Equation Solution of Maxwell’s Equations from Zero Frequency to Microwave Frequency,” *IEEE Trans. Antennas Propagat.*, vol. 48, pp. 1635-1645, Oct. 2000.

[9] J. F. Lee, R. Lee, and R. J. Burkholder, “Loop Star Basis Functions and a Robust Precodnitioner for EFIE Scattering Problems,” *IEEE Trans. Antennas Propagat.*, vol. 51, pp. 1855-1863, Aug. 2003.

[10] T. F. Eibert, “Iterative-Solver Convergence for Loop-Star and Loop-Tree Decomposition in Method-of-Moments Solutions of the Electric-Field Integral Equation,” *IEEE Antennas Propag. Mag.*, vol. 46, pp. 80-85, Jun. 2004.

[11] F. P. Andriulli, A. Tabacco, and G. Vecchi, “Solving the EFIE at Low Frequencies with a Conditioning that Grows Only Logarithmically with the Number of Unknowns,” *IEEE Trans. Antennas Propagat.*, vol. 58, no. 5, pp. 1614-1624, May 2010.

[12] F. Vipiana, P. Pirinoli, and G. Vecchi, “A Multiresolution Method of Moments for Triangular Meshes,” *IEEE Trans. Antennas Propag.*, vol. 53, no. 7, pp. 2247-2258, Jul. 2005.

[13] F. Vipiana, G. Vecchi, and P. Pirinoli. “A Multiresolution System of Rao–Wilton–Glisson Functions,” *IEEE Trans. Antennas Propagat.*, vol. 55, no. 3, pp. 924-930, Mar. 2007.

[14] F. Andriulli, A. Tabacco, and G. Vecchi, “A Multiresolution Approach to the Electric Field Integral Equation in Antenna Problems,” *SIAM J. Sci. Comput.*, vol. 29, pp. 1-21, Jan. 2007.

[15] R. S. Chen, J. J. Ding, D. Z. Ding, Z. H. Fan, and D. X. Wang, “A Multiresolution Curvilinear Rao-Wilton-Glisson Basis Function for Fast Analysis of Electromagnetic Scattering,” *IEEE Trans. Antennas Propagat.*, vol. 57, no. 10, pp. 3179-3188, Oct., 2009.

[16] F. P. Andriulli, F. Vipiana, and G. Vecchi, “Enhanced Multiresolution Basis for the MoM Analysis of 3D Structures,” in *Proc. IEEE Int. Symp. Antennas Propagat.*, Honolulu, HI, Jun. 2007, pp. 5612-5615.

[17] F. P. Andriulli, F. Vipiana, and G. Vecchi, "Hierarchical Bases for Non-Hierarchic 3-D Triangular Meshes," *IEEE Trans. Antennas Propagat.*, vol. 56, pp. 2288-2297, Aug. 2008.

[18] F. Vipiana, F. P. Andriulli, and G. Vecchi, "Two-Tier Non-Simplex Grid Hierarchic Basis for General 3D Meshes," *Waves in Random and Complex Media*, vol. 19, no. 1, Feb. 2009, pp.126-146.

[19] F. Vipiana, and G. Vecchi, "A Novel, Symmetrical Solenoidal Basis for the MoM Analysis of Closed Surfaces," *IEEE Trans. Antennas Propagat.*, vol. 57, no. 4, pp. 1294-1299, April 2009.

[20] F. Vipiana, P. Pirinoli, and G. Vecchi, "Regularization Effect of a Mutiresolution Basis on the EFIE-MoM Matrix," *IEEE Antennas and Propagation Society Int. Symp. Digest*, Washington, DC, Jul. 2005, vol. 3b, pp. 192-195.

[21] F. Vipiana, P. Pirinoli, and G. Vecchi, "Spectral Properties of the EFIE-MoM Matrix for Dense Meshes with Different Types of Bases," *IEEE Trans. Antennas Propagat.*, vol. 55, no. 11, pp. 3229-3238, Nov. 2007.

[22] J. J. Ding, J. Zhu, D. Z. Ding, and R. S. Chen, "Application of Perturbed Multiresolution Preconditioner Technique Combined with MLFMA for Scattering Problem," in *Proc. Int. Conf. on Microwave and Millimeter Wave Technology*, pp. 978-981, Apr. 2008.

[23] H. Chen, D. Z. Ding, R. S. Chen, D. X. Wang, and E. K. Yung, "Application of Multiresolution Preconditioner Technique for Scattering Problem in a Half Space," in *Proc. Int. Conf. on Microwave and Millimeter Wave Technology*, pp. 975-977, Apr. 2008.

[24] Y. Q. Hu, J. J. Ding, D. Z. Ding, and R. S. Chen, "Analysis of Electromagnetic Scattering from Dielectric Objects above a Lossy Half-Space by Multiresolution Preconditioned Multilevel Fast Multipole Algorithm," *IET Microw. Antennas Propag.*, vol. 4, iss. 2, pp. 232-239, Feb., 2010.

[25] M. M. Li, J. J. Ding, D. Z. Ding, Z. H. Fan, and R. S. Chen, "Multiresolution Preconditioned Multilevel UV Method for Analysis of Planar Layered Finite Frequency Selective Surface," *Microwave and Optical Technology Letters*, vol. 52, no. 7, pp. 1530-1536, July 2010.

[26] F. Vipiana, M. A. Francavilla, and G. Vecchi, "A Multi-Resolution Stabilization of the Incomplete LU Preconditioner," in *Antennas and Propagation Society International Symposium*, Charleston, SC, June 2009, pp. 1-4.

[27] F. Vipiana, M. A. Francavilla, and G. Vecchi, "EFIE Modeling of High-Definition Multiscale Structures," *IEEE Trans. Antennas Propagat.*, vol. 58, no. 7, pp. 2362-2374, July 2010.

[28] F. Vipiana, G. Vecchi, and D. R. Wilton, "Automatic Loop-Tree Scheme for Arbitrary Conducting Wire-Surface Structures," *IEEE Trans. Antennas Propagat.*, vol. 57, no. 11, pp. 3564-3574, Nov. 2009.

Performance Evaluation of State-of-the-Art Linear Iterative Solvers Based on IDR Theorem for Large Scale Electromagnetic Multiple Scattering Simulations

Norimasa Nakashima[1], Seiji Fujino[2], and Mitsuo Tateiba[3]

[1] Faculty of Information Science and Electrical Engineering
Kyushu University, Fukuoka, 819-0395, Japan
norimasa@ait.kyushu-u.ac.jp

[2] Research Institute for Information Technology
Kyushu University, Fukuoka, 812-8581, Japan
fujino@cc.kyushu-u.ac.jp

[3] Ariake National College of Technology
Omuta, 836-8585, Japan
tateiba@ariake-nct.ac.jp

Abstract ─ The present paper treats with the latest linear iterative solver IDR(*s*) method and its variants proposed by P. Sonneveld and M. van Gijzen. We derive preconditioned algorithms of the solvers based on right preconditioning and list them. The solvers are numerically tested in terms of convergence and accuracy for the computation of electromagnetic wave scattering from over 10^4 dielectric cylinders. Consequently, minimization schemes for residual vectors refine not only convergence but also accuracy for the original IDR(*s*) method. However, a spurious convergence may be confirmed and its influence is *1* or *2* digit error independently of parameter *s*.

Index Terms ─ Boundary element method, electromagnetic multiple scattering, IDR(*s*) method.

I. INTRODUCTION

The aim of the authors' work is to simulate electromagnetic (EM) wave scattering from a medium composed of several kinds of objects in shape, size, and material. As a basic issue, we try to develop fast techniques for the computation by means of the boundary element method (BEM) [1]. In the BEM computation, the most time-consuming part rises from solving the dense linear system of equations followed by the discretization of boundary integral equations. Our previous work presented that both the computational and memory complexities for the multiplication of a vector by the coefficient matrix can be drastically reduced by a wideband fast multipole algorithm [2]. Then, we use an iterative solver based on the Krylov subspace method [3] because the operation of matrix-vector multiplication is in its algorithm. The propositions of high performance iterative solvers and preconditionings are important to the fast computation today.

The authors have used a generalized minimal residual method with restart process (GMRES(*m*) method [4]) for solving the linear system of equations [5]. A restart cycle *m* should be chosen a very large value for high convergence but it needs much memory space. P. Sonneveld and M. van Gijzen proposed the IDR(*s*) method which belongs to the Krylov subspace method [6]. "IDR" is an abbreviation of "Induced Dimension Reduction". The authors' numerical experiments revealed that the IDR(*s*) method was better than the GMRES(*m*) method in terms of convergence and memory efficiency for the BEM analyses of electromagnetic wave scattering from many dielectric cylinders. As the parameter *s* of the IDR(*s*) method is larger, however, convergence is more improved but the accuracy deteriorates drastically [7].

$$E_z^{\mathrm{inc}}(\boldsymbol{\rho}_i) = \frac{1}{2}E_z(\boldsymbol{\rho}_i) + \frac{\mathrm{j}}{4}\sum_{n=1}^{N}\left[\int_{C_n}\left\{E_z(\boldsymbol{\rho}'_n)\frac{\partial \mathrm{H}_0^{(2)}(k_0|\boldsymbol{\rho}_i - \boldsymbol{\rho}'_n|)}{\partial n'_n} - \mathrm{H}_0^{(2)}(k_0|\boldsymbol{\rho}_i - \boldsymbol{\rho}'_n|)\frac{\partial E_z}{\partial n'_n}(\boldsymbol{\rho}'_n)\right\}\mathrm{d}l'_n\right] \quad (1)$$

$$0 = \frac{1}{2}E_z(\boldsymbol{\rho}_i) - \frac{\mathrm{j}}{4}\int_{C_i}\left\{E_z(\boldsymbol{\rho}'_i)\frac{\partial \mathrm{H}_0^{(2)}(k_i|\boldsymbol{\rho}_i - \boldsymbol{\rho}'_i|)}{\partial n'_i} - \mathrm{H}_0^{(2)}(k_i|\boldsymbol{\rho}_i - \boldsymbol{\rho}'_i|)\mu_r^{(i)}\frac{\partial E_z}{\partial n'_i}(\boldsymbol{\rho}'_i)\right\}\mathrm{d}l'_i \quad (i = 1, 2, \cdots, N). \quad (2)$$

Such a prejudicial phenomenon concerning accuracy is called "a spurious convergence" in this paper. The authors managed the spurious convergence by using Sleijpen and van der Vorst's convergence refinement method [8]. This technique is very simple and easy to implement but is not complete solution. Sakurai *et al.* proposed an auto corrected (AC) IDR(*s*) method that perfectly dissolves the problem of the spurious convergence [9]. In this method, however, a computation of matrix-vector multiplication may be added for one iteration. Then the net computation time may become much longer for the AC-IDR(*s*) method than for the original one in solving a large scale dense linear system of equations. On the other hand, Sonneveld and van Gijzen modified the algorithm and proposed two variants of the IDR(*s*) method in order to expedite convergence [10, 11].

This paper investigates the performance of the variant IDR(*s*) methods for the computation of EM wave scattering from many dielectric cylinders by means of the BEM. We solve the linear system of equations of order 10^5 by the IDR(*s*) method and its variants and compare their convergence and accuracy. After this introductory Section I, Section II presents two-dimensional boundary integral equations and discretization of them. We explain the structures of the coefficient matrix and the unknown and right-hand side vectors. Section III outlines the variant IDR(*s*) methods with a right preconditioning. Performance evaluations are done in Section IV. Finally, Section V summarizes conclusions of this study. Throughout this paper, $\mathrm{e}^{\mathrm{j}\omega t}$ time convention is used and suppressed.

II. FORMULATION

Let us consider the two-dimensional problem of EM wave scattering by *N* infinitely long cylinders in a vacuum. The relative permittivity and permeability of the *i*th cylinder are $\varepsilon_{\mathrm{r}}^{(i)}$ and $\mu_{\mathrm{r}}^{(i)}$, respectively. The wave numbers of the vacuum and the *i*th cylinder are represented by k_0 and $k_i = k_0\sqrt{\varepsilon_r^{(i)}\mu_r^{(i)}}$, respectively. Each axis of the cylinders is parallel to the *z*-axis of the cylindrical coordinate system. We formulate this problem in the electrical field integral equations (EFIEs) for TM wave. The *z*-components of unknown electric fields E_z and their normal derivatives $\partial E_z/\partial n$ are given by Eqs. (1) and (2). Here, the C_i is the boundary of the *i*th cylinder, and $\boldsymbol{\rho}_i$ and $\boldsymbol{\rho}'_i$ are the observation and integration points on C_i, respectively. The $\mathrm{H}_0^{(2)}$ is the zero order Hankel function of the second kind, and $\partial/\partial n_i$ is the outward normal derivative on C_i. The E_z^{inc} is an incident wave.

The integral equations can be discretized through the BEM [1]. We divide each boundary into M_i boundary elements and choose the rectangular pulse function as a basis function. Using the point matching method, we obtain a dense linear system of *L* equations $\mathrm{A}\boldsymbol{x} = \boldsymbol{b}$, where $L = 2(M_1 + M_2 + \cdots + M_N)$. The linear system is composed of blocks and subvectors:

$$\mathcal{A} = \left[\begin{array}{ccc|ccc} a_{11}^{\mathrm{out}} & \cdots & a_{1N}^{\mathrm{out}} & b_{11}^{\mathrm{out}} & \cdots & b_{1N}^{\mathrm{out}} \\ \vdots & \ddots & \vdots & \vdots & \ddots & \vdots \\ a_{N1}^{\mathrm{out}} & \cdots & a_{NN}^{\mathrm{out}} & b_{N1}^{\mathrm{out}} & \cdots & b_{NN}^{\mathrm{out}} \\ \hline a_{11}^{\mathrm{in}} & & 0 & b_{11}^{\mathrm{in}} & & 0 \\ & \ddots & & & \ddots & \\ 0 & & a_{NN}^{\mathrm{in}} & 0 & & b_{NN}^{\mathrm{in}} \end{array}\right] \quad (3)$$

$$\boldsymbol{x} = \left[\begin{array}{ccc|ccc} \boldsymbol{\alpha}^{(1)} & \cdots & \boldsymbol{\alpha}^{(N)} & \boldsymbol{\beta}^{(1)} & \cdots & \boldsymbol{\beta}^{(N)} \end{array}\right]^T \quad (4)$$

$$\boldsymbol{b} = \left[\begin{array}{ccc|ccc} \boldsymbol{e}_z^{(1)} & \cdots & \boldsymbol{e}_z^{(N)} & \mathbf{0}^{(1)} & \cdots & \mathbf{0}^{(N)} \end{array}\right]^T. \quad (5)$$

Here, the blocks a_{ij} and b_{ij} are the matrix of M_i by M_j. The notations "out" and "in" mean outer and internal fields of cylinders, respectively. The subvectors of M_i order $\boldsymbol{e}_z^{(i)}$, $\boldsymbol{\alpha}^{(i)}$ and $\boldsymbol{\beta}^{(i)}$ indicate the incident wave, unknown field, and its normal derivative on the boundary elements, respectively. The *T* and $\mathbf{0}^{(i)}$ mean matrix transpose and the M_i dimensional zero vector, respectively. Equation (3) implies that the lower half of coefficient matrix is comparably sparse. Then, we reduce the number of unknowns in half and obtain the linear system given by Eq. (6) [5].

$$\begin{pmatrix} -a_{11}^{\mathrm{out}}(a_{11}^{\mathrm{in}})^{-1}+b_{11}^{\mathrm{out}}(b_{11}^{\mathrm{in}})^{-1} & \cdots & -a_{1N}^{\mathrm{out}}(a_{NN}^{\mathrm{in}})^{-1}+b_{1N}^{\mathrm{out}}(b_{NN}^{\mathrm{in}})^{-1} \\ \vdots & \ddots & \vdots \\ -a_{N1}^{\mathrm{out}}(a_{11}^{\mathrm{in}})^{-1}+b_{N1}^{\mathrm{out}}(b_{11}^{\mathrm{in}})^{-1} & \cdots & -a_{NN}^{\mathrm{out}}(a_{NN}^{\mathrm{in}})^{-1}+b_{NN}^{\mathrm{out}}(b_{NN}^{\mathrm{in}})^{-1} \end{pmatrix} \begin{pmatrix} \boldsymbol{x}^{(1)} \\ \vdots \\ \boldsymbol{x}^{(N)} \end{pmatrix} = \begin{pmatrix} \boldsymbol{e}_z^{(1)} \\ \vdots \\ \boldsymbol{e}_z^{(N)} \end{pmatrix}. \tag{6}$$

III. THE IDR(*s*) METHOD AND ITS VARIANTS

The IDR(*s*) method is one of the iterative solvers for nonsymmetric linear system of equations and is derived by a new approach different from conventional BiCG-like and GMRES-like solvers. In the conventional solvers, the solution vector is iteratively refined thorough a bi-orthgonalization scheme and a minimal norm scheme over the Krylov subspace, respectively [3]. In the IDR(*s*) method, whereas, spaces are iteratively generated from the complete Krylov space according to a rule. The solution vector is determined in order that the corresponding residual vector may belong to the spaces. From the IDR theorem, the dimensions of the spaces monotonically decrease, and the residual vector converges to the zero vector [6]. Thus, the IDR(*s*) method is a new solver which belongs to neither BiCG-like nor GMRES-like solvers.

The subsequent spaces are generated every *s+1* iteration, and we actually compute *s+1* basis vectors of corresponding space. Due to the induced dimension reduction, the residual vectors only for every *s+1*th iteration are expected to reduce monotonically. In order to accelerate convergence, Sonneveld and van Gijzen introduced the minimization scheme for residual vectors based on an orthonormalization. They also adopt a bi-orthogonalization scheme to minimize the residual vectors. The new solvers based on the above two techniques are called "MR-IDR(*s*) method" and "Bi-IDR(*s*) method", respectively.

A preconditioned MR-IDR(*s*) method and Bi-IDR(*s*) method are listed in Figs. 1 and 2, respectively. Here, we derive the preconditioned algorithms based on a right preconditioning. A pseudo code of a preconditioned IDR(*s*) method is already presented in [7]. The notations K^{-1} and *H* stand for a preconditioner and Hermitian adjoint, respectively.

1. Let $\boldsymbol{x}_0$ be an initial guess, and put $\boldsymbol{r}_0 = \boldsymbol{b} - \mathcal{A}\boldsymbol{x}_0$
2. $\mathcal{G} = \mathcal{U} = \mathcal{O},\ \mathcal{M} = \mathcal{I},\ \omega = 1,\ n = 0$
3. While $||\boldsymbol{r}_n||_2/||\boldsymbol{r}_0||_2 > \epsilon$ Do
4. For $i = 0, \ldots, s-1$ Do
5. Solve $\boldsymbol{c}$ from $\mathcal{M}\boldsymbol{c} = \mathcal{P}^H\boldsymbol{r}_n$
6. $\boldsymbol{v} = \boldsymbol{r}_n - \mathcal{G}\boldsymbol{c}$
7. $\boldsymbol{u}_n = \mathcal{U}\boldsymbol{c} + \omega\mathcal{K}^{-1}\boldsymbol{v},\ \ \boldsymbol{g}_n = \mathcal{A}\boldsymbol{u}_n$
8. For $j = 1, \ldots, i$ Do
9. $\boldsymbol{g}_n = \boldsymbol{g}_n - (\boldsymbol{g}_{n-j}^H\boldsymbol{g}_n)\boldsymbol{g}_{n-j}$
   $\boldsymbol{u}_n = \boldsymbol{u}_n - (\boldsymbol{g}_{n-j}^H\boldsymbol{g}_n)\boldsymbol{u}_{n-j}$
10. End Do
11. $\boldsymbol{g}_n = \dfrac{\boldsymbol{g}_n}{||\boldsymbol{g}_n||_2},\ \ \boldsymbol{u}_n = \dfrac{\boldsymbol{u}_n}{||\boldsymbol{g}_n||_2}$
12. $\boldsymbol{r}_{n+1} = \boldsymbol{r}_n - (\boldsymbol{g}_n^H\boldsymbol{r}_n)\boldsymbol{g}_n,$
    $\boldsymbol{x}_{n+1} = \boldsymbol{x}_n + (\boldsymbol{g}_n^H\boldsymbol{r}_n)\boldsymbol{u}_n$
13. $n = n + 1$
14. End Do
15. $\mathcal{G} = (\boldsymbol{g}_{n-1} \cdots \boldsymbol{g}_{n-s}),$
    $\mathcal{U} = (\boldsymbol{u}_{n-1} \cdots \boldsymbol{u}_{n-s})$
16. $\mathcal{M} = \mathcal{P}^H\mathcal{G}$
17. Solve $\boldsymbol{c}$ from $\mathcal{M}\boldsymbol{c} = \mathcal{P}^H\boldsymbol{r}_n$
18. $\boldsymbol{v} = \boldsymbol{r}_n - \mathcal{G}\boldsymbol{c},\ \ \boldsymbol{t} = \mathcal{A}\mathcal{K}^{-1}\boldsymbol{v}$
20. $\omega = \dfrac{\boldsymbol{t}^H\boldsymbol{v}}{\boldsymbol{t}^H\boldsymbol{t}}$
    $\left(\begin{array}{l} \rho = \dfrac{\boldsymbol{t}^H\boldsymbol{v}}{||\boldsymbol{t}||_2\,||\boldsymbol{v}||_2}, \\ \text{if } |\rho| < \kappa \text{ then } \omega = \dfrac{\kappa}{\rho}\omega \end{array} \right)$
21. $\boldsymbol{x}_{n+1} = \boldsymbol{x}_n + \mathcal{U}\boldsymbol{c} + \omega\mathcal{K}^{-1}\boldsymbol{v}$
    $\boldsymbol{r}_{n+1} = \boldsymbol{r}_n - \mathcal{G}\boldsymbol{c} - \omega\boldsymbol{t}$
22. $n = n + 1$
23. End While

Fig. 1. A preconditioned MR-IDR(*s*) algorithm.

1. Let $\boldsymbol{x}_0$ be an initial guess, and put
   $\boldsymbol{r}_0 = \boldsymbol{b} - \mathcal{A}\boldsymbol{x}_0$
2. $\boldsymbol{u}_i = \boldsymbol{g}_i = \boldsymbol{0}$ $(i = 0, \ldots, s-1)$,
   $\mathcal{M} = \mathcal{I}$, $\omega = 1$, $n = 0$
3. While $||\boldsymbol{r}_n||_2/||\boldsymbol{r}_0||_2 > \epsilon$ Do
4. $\boldsymbol{m} = \mathcal{P}^H \boldsymbol{r}_n$
5. For $i = 0, \ldots, s-1$ Do
6. Solve $\boldsymbol{c}$ from $\mathcal{M}\boldsymbol{c} = \boldsymbol{m}$
7. $\boldsymbol{v} = \boldsymbol{r}_n - \sum_{j=i}^{s-1} c_j \boldsymbol{g}_j$
8. $\boldsymbol{u}_i = \omega \mathcal{K}^{-1}\boldsymbol{v} + \sum_{j=i}^{s-1} c_j \boldsymbol{u}_i$, $\boldsymbol{g}_i = \mathcal{A}\boldsymbol{u}_i$
9. For $j = 0, \ldots, i-1$ Do
10. $\boldsymbol{g}_i = \boldsymbol{g}_i - \frac{\boldsymbol{p}_j^H \boldsymbol{g}_i}{M_{jj}} \boldsymbol{g}_j$
    $\boldsymbol{u}_i = \boldsymbol{u}_i - \frac{\boldsymbol{p}_j^H \boldsymbol{g}_i}{M_{jj}} \boldsymbol{u}_j$
11. End Do
12. $M_{ji} = \boldsymbol{p}_j^H \boldsymbol{g}_i$ $(j = i, \ldots, s-1)$
13. $\boldsymbol{r}_{n+1} = \boldsymbol{r}_n - \frac{m_i}{M_{ii}} \boldsymbol{g}_i$,
    $\boldsymbol{x}_{n+1} = \boldsymbol{x}_n + \frac{m_i}{M_{ii}} \boldsymbol{u}_i$
14. If $i \leq s-2$ then
15. $m_j = \begin{cases} 0 & (j = 0, \ldots, i) \\ m_j - \frac{m_i}{M_{ii}} M_{ji} & \\ & (j = i+1, \ldots, s-1) \end{cases}$
16. End If
17. $n = n + 1$
18. End Do
19. $\boldsymbol{t} = \mathcal{A}\mathcal{K}^{-1}\boldsymbol{r}_n$
20. $\omega = \frac{\boldsymbol{t}^H \boldsymbol{r}_n}{\boldsymbol{t}^H \boldsymbol{t}}$
    $\left(\rho = \frac{\boldsymbol{t}^H \boldsymbol{r}_n}{||\boldsymbol{t}||_2 \, ||\boldsymbol{r}_n||_2}, \right.$
    $\left. \text{if } |\rho| < \kappa \text{ then } \omega = \frac{\kappa}{\rho}\omega \right)$
21. $\boldsymbol{x}_n = \boldsymbol{x}_n + \omega \mathcal{K}^{-1}\boldsymbol{r}_n$, $\boldsymbol{r}_n = \boldsymbol{r}_n - \omega \boldsymbol{t}$
22. $n = n + 1$
23. End While

Fig. 2. A preconditioned Bi-IDR(s) algorithm.

The matrix P = ($\boldsymbol{p}_0$ $\boldsymbol{p}_1$ ⋯ $\boldsymbol{p}_{s-1}$) is an orthogonal matrix followed by [6]. The large bracket is Sleijpen and van der Vorst's convergence refinement technique. We fix the parameter κ at *0.7* that is recommended by them [8]. This technique has the effect to reduce a spurious convergence for the IDR(*s*) method [7]. As shown in the pseudo codes, solving a linear system of *s* equations is necessary for the IDR(*s*) methods. We do it by using the direct method with a LU factorization in the original IDR(*s*) method and the MR-IDR(*s*) method. In the Bi-IDR(*s*) method, the coefficient matrix M is a lower triangular matrix, and we obtain solution vector $\boldsymbol{c}$ by a forward substitution.

IV. PERFORMANCE EVALUATION

We treat EM wave scattering from regularly placed $N \times N$ dielectric circular cylinders whose configurations are listed in Tab. 1. The incident wave is assumed as a plane wave. Comparison among a various kinds of IDR(*s*) methods is carried out in terms of the convergence and accuracy. It notes that the computation time is directly connected with the number of matrix-vector multiplications to convergence (abbreviate to ``MATVECS", hereafter) [5]. Computations are performed on Intel Core2Duo E6700 processor and 2GB of main memory. An iterative process is begun with $\boldsymbol{x}_0 = \boldsymbol{0}$, and the stopping criterion ε is put at 10^{-10}. A matrix-vector multiplication in an iterative process is expedited by the wideband fast multipole algorithm with the tolerance of 10^{-10} [2]. We exploit the block Jacobi preconditioning.

Results of performance evaluation are displayed in Figs. 3 and 4. Here, the accuracy for converged solution vector $\boldsymbol{x}_n$ is estimated by $||\mathrm{A}\boldsymbol{x}_n - \boldsymbol{b}||_2 / ||\boldsymbol{b}||_2$. Performances of a full GMRES(*m*) method are exhibited in each figure. The full GM-

Table 1: Physical parameters for cylinders

Normalized radius: $k_0 a$	*1.0*
Relative permittivity: $\varepsilon_r^{(i)}$	*2.0*
Relative permeability: $\mu_r^{(i)}$	*1.0*
Length between each cylinder: $k_0 d$ (in row and column directions)	$\sqrt{100\pi}\, k_0 a$
Fractional volume: *f*	*0.01*

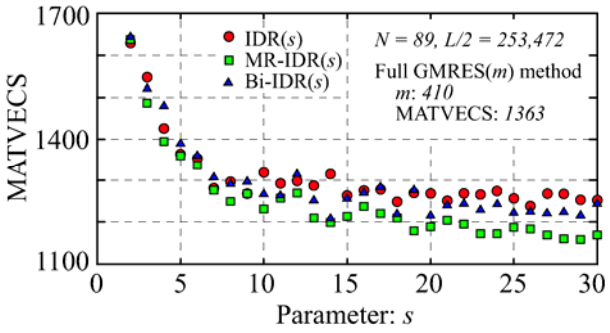

(a) $N = 89,\ L/2 = 253,472$

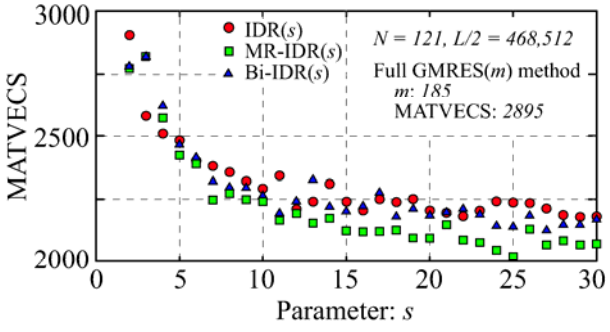

(b) $N = 121,\ L/2 = 468,512$

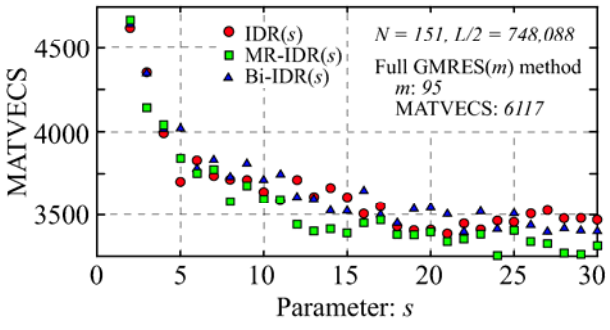

(c) $N = 153,\ L/2 = 748,088$

Fig. 3. Fluctuation of MATVECS for parameter *s* of the preconditioned IDR(*s*) methods.

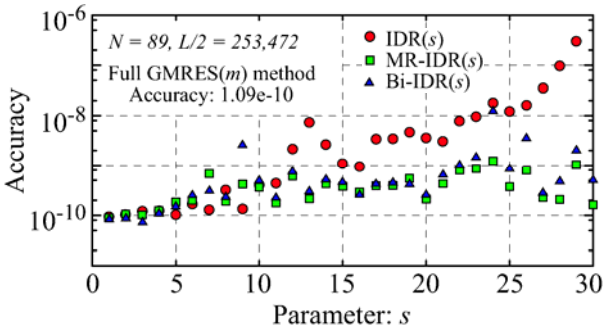

(a) $N = 89,\ L/2 = 253,472$

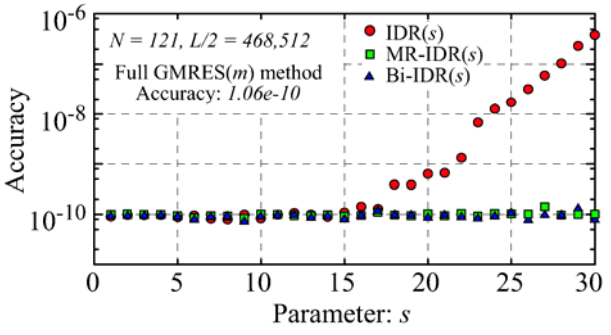

(b) $N = 121,\ L/2 = 468,512$

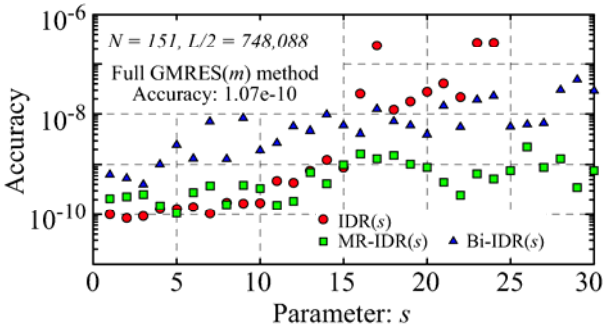

(c) $N = 153,\ L/2 = 748,088$

Fig. 4. Fluctuation of the accuracy for parameter *s* of the preconditioned IDR(*s*) methods.

RES (*m*) method means that the restart cycle *m* is decided in order that we may use over *90%* of the amount of memory installed. These figures expose that both the MR-IDR(*s*) and Bi-IDR(*s*) methods refine not only the convergence but also accuracy for the original IDR(*s*) method. The MR-IDR(*s*) method is the best in the three types of IDR(*s*) method in terms of convergence and accuracy, and converges faster than the full GMRES (*m*) method. Unfortunately, the spurious convergence is confirmed in figure 4 but its feature is different among the solvers. Deterioration of accuracy for the MR-IDR(*s*) and Bi-IDR(*s*) methods do not always occur and its impact may be in *1* or *2* digit error independently of parameter *s*. The authors are considered that a mechanism of the spurious convergence for the MR-IDR(*s*) and Bi-IDR(*s*) methods are identical but differ from that for the original IDR(*s*) method.

Figure 5 exhibits convergence behaviors of a variety of IDR(*s*) methods with an optimal parameter and the full GMRES (*m*) method. The optimal parameter means that MATVECS is minimum and the deterioration of accuracy is under *1* digit. We can find from Fig. 5 that the full GMRES (*m*) method rapidly converge at first but the convergence curve of it becomes slow due to restart.

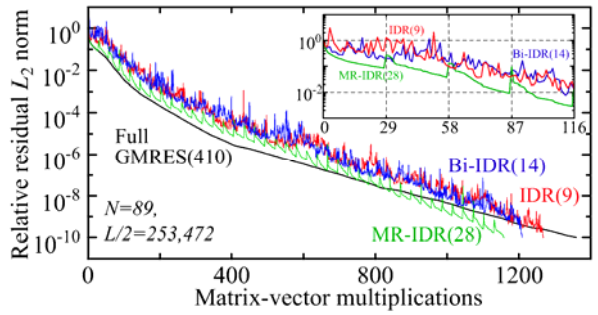

(a) $N = 89,\ L = 253,472$

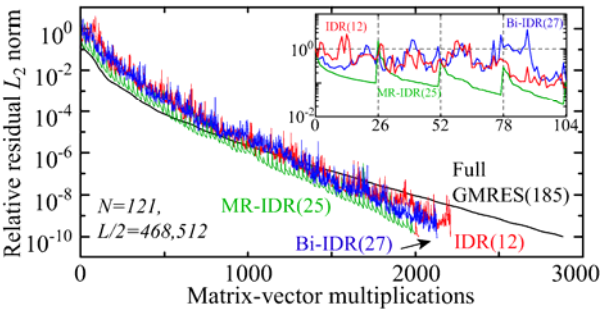

(b) $N = 121,\ L = 468,512$

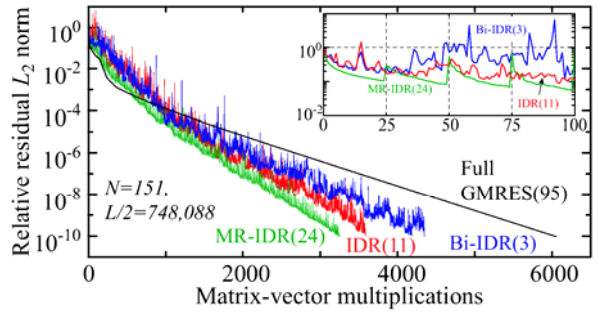

(c) $N = 153,\ L = 748,088$

Fig. 5. Convergence of the preconditioned IDR(*s*) methods and the full GMRES (*m*) method.

The convergence curves of the IDR(*s*) methods have a thumping vibration, but it reaches the value of stopping criterion at a constant rate. The magnification of the curves for first several iterations is pasted on each figure. We can see from them that the convergence curve of the MR-IDR(*s*) method is smoother than other two types of the IDR(*s*) methods. The needles in the convergence curve for the MR-IDR(*s*) method are confirmed every *s+1* iterations. This may be caused by the update space in algorithm.

Table 2 is the comparison of the convergence, the memory used, and accuracy among the variant IDR(*s*) methods for the top three parameters and the GMRES (*50*), GMRES (*100*) and full GMRES (*m*) methods. Here, the top three parameters mean that MATVECS is minimum and the accuracy is around the stopping criterion.

Table 2: Comparison between the IDR(*s*) methods and the GMRES (*m*) methods

(a) $N = 89,\ L/2 = 253,472$

Method	MATVECS (ratio)	Mem. [MB] (ratio)	Accuracy
IDR(9)	1268 (0.93)	385 (0.21)	1.33e-10
IDR(7)	1280 (0.94)	362 (0.19)	1.27e-10
IDR(6)	1354 (0.99)	350 (0.19)	1.67e-10
MR-IDR(28)	1159 (0.85)	612 (0.33)	1.99e-10
MR-IDR(30)	1169 (0.86)	636 (0.34)	1.61e-10
MR-IDR(27)	1169 (0.86)	600 (0.32)	2.28e-10
Bi-IDR(14)	1209 (0.89)	445 (0.24)	5.40e-10
Bi-IDR(18)	1218 (0.89)	493 (0.26)	4.47e-10
Bi-IDR(20)	1216 (0.89)	517 (0.28)	2.64e-10
GMRES(50)	1783 (1.31)	468 (0.25)	1.10e-10
GMRES(100)	1662 (1.22)	662 (0.35)	1.06e-10
GMRES(410)	1363 (1.00)	1865 (1.00)	1.09e-10

(b) $N = 121,\ L/2 = 468,521$

Method	MATVECS (ratio)	Mem. [MB] (ratio)	Accuracy
IDR(10)	2291 (0.79)	765 (0.85)	8.38e-11
IDR(9)	2320 (0.80)	744 (0.82)	9.80e-11
IDR(8)	2351 (0.81)	723 (0.80)	7.96e-11
MR-IDR(25)	2020 (0.70)	1080 (0.58)	1.01e-10
MR-IDR(24)	2046 (0.71)	1059 (0.57)	9.99e-11
MR-IDR(29)	2067 (0.71)	1164 (0.62)	9.98e-11
Bi-IDR(27)	2129 (0.74)	1122 (0.60)	9.89e-11
Bi-IDR(25)	2143 (0.74)	1080 (0.58)	1.06e-10
Bi-IDR(24)	2146 (0.74)	1059 (0.57)	9.33e-11
GMRES(50)	3661 (1.26)	905 (0.48)	1.06e-10
GMRES(100)	3291 (1.14)	1262 (0.67)	1.07e-10
GMRES(185)	2895 (1.00)	1870 (1.00)	1.06e-10

(c) $N = 153,\ L/2 = 749,088$

Method	MATVECS (ratio)	Mem. [MB] (ratio)	Accuracy
IDR(10)	3639 (0.59)	1146 (0.63)	1.70e-10
IDR(5)	3702 (0.61)	977 (0.53)	1.30e-10
IDR(9)	3710 (0.61)	1112 (0.61)	1.64e-10
MR-IDR(24)	3249 (0.53)	1620 (0.89)	4.14e-10
MR-IDR(29)	3261 (0.53)	1789 (0.98)	3.45e-10
MR-IDR(28)	3269 (0.53)	1755 (0.96)	8.29e-10
Bi-IDR(3)	4349 (0.71)	909 (0.50)	4.08e-10
Bi-IDR(2)	4655 (0.76)	875 (0.48)	4.57e-10
Bi-IDR(1)	7827 (1.28)	841 (0.46)	6.46e-10
GMRES(50)	6647 (1.09)	1366 (0.75)	1.06e-10
GMRES(95)	6117 (1.00)	1820 (1.00)	1.07e-10
GMRES(100)	- (-)	- (-)	-

Here, we cannot execute the GMRES (*100*) method for *N = 153* case due to the shortage of memory space. The ratio to the results of the full GMRES (*m*) method is written in the columns of MATVECS and Mem. in Tab. 2.

Figures 2 and 3 and Tab. 2 disclose that the optimal parameters for the IDR(*s*) and MR-IDR(*s*) methods may be in $5 \le s \le 10$ and $25 \le s \le 30$, respectively. However, that for the Bi-IDR(*s*) method is hard to determine because the top three parameters are quite different in each problem. The amount of used memory of the IDR(*s*) methods increases proportional to parameter *s*. Then the MR-IDR(*s*) method with optimal parameters needs more memory space than the IDR(*s*) and Bi-IDR(*s*) methods.

The IDR(*s*) methods with the optimal parameter converge faster than the full GMRES (*m*) method, and the difference of MATVECS becomes larger accordingly to the enlargement of problem size. The amount of used memory is less for the IDR(*s*) methods than for the full GMRES (*m*) method. Therefore, we conclude that IDR(*s*) method is better than the GMRES (*m*) method in terms of not only convergence but also the amount of memory used in the large scale computation of EM wave scattering from many objects. Especially, the MR-IDR(*s*) method is the best among the three types of IDR(*s*) method in terms of convergence and accuracy. However, spurious convergence may occur, and the user has to check the accuracy for convergent solution.

V. CONCLUDING REMARKS

This paper remarks variants of IDR(*s*) method. Preconditioned MR-IDR(*s*) and Bi-IDR(*s*) algorithms are presented. Performance evaluations are done for the computation of the dense linear system of equations of order 10^5 followed by the BEM analysis of EM wave multiple scattering. As a consequence, the MR-IDR(*s*) method is the best among the three types of IDR(*s*) method in terms of convergence and accuracy. Optimal parameter for the MR-IDR(*s*) method may be in $25 \le s \le 30$. The MR-IDR(*s*) method with optimal parameter converges faster and spends less memory space than the full GMRES (*m*) method. However, the accuracy the MR-IDR(*s*) method may deteriorate in *1* digit independently of parameter *s*. The investigation and provision of it are important subjects.

ACKNOWLEDGMENT

This research was supported by the Ministry of Education, Culture, Sports, Science, and Technology, Grant-in-Aid for Young Scientists (B), 20760058, 2009. The authors would like to thank Prof. M. van Gijzen for his helpful discussions on this work.

REFERENCES

[1] N. Morita, N. Kumagai, and J. R. Mautz, *Integral Equation Methods for Electromagnetics*, Artech House, 1990.

[2] N. Nakashima and M. Tateiba, "A Wideband Fast Multipole Algorithm for Two-dimensional Volume Integral Equations," *Int. J. Numer. Meth. Eng.*, vol. 77, pp. 195-213, 2009.

[3] Y. Saad, *Iterative Methods for Sparse Linear Systems*, SIAM, 2003.

[4] Y. Saad and M. Schultz, "GMRES: A Generalized Minimal Residual Algorithm for Solving Nonsymmetric Linear Systems," *SIAM J. Sci. Stat. Comput.*, vol. 7, no. 3, pp. 856-869, 1986.

[5] N. Nakashima, S. Fujino, and M. Tateiba, "Fast Computation for Electromagnetic Wave Scattering Problem with Many Dielectric Cylinder (2) --- Two-step Preconditioning Combined with Half Reduction and Block Jacobi," *Trans. IPSJ*, vol. 45, no. SIG1(ACS4), pp. 1-9, 2004. (in Japanese)

[6] P. Sonneveld and M. B. van Gijzen, "IDR(*s*): A Family of Simple and Fast Algorithms for Solving Large Nonsymmetric Systems of Linear Equations," *SIAM J. Sci. Comput.*, vol. 31, pp. 1035-1062, 2008.

[7] N. Nakashima, S. Fujino, M. Tateiba, and Y. Onoue, "An Application of IDR(*s*) Method to Boundary Element Analyses of Two-dimensional Electromagnetic Multiple Scattering," *IEICE Trans. Electron.*, vol. J92-C, no. 4, pp. 111-118, 2009. (in Japanese)

[8] G. L. G. Sleijpen and H. A. van der Vorst, "Maintaining Convergence Properties of BiCGStab Methods in Finite Precision Arithmetic," *Numer. Algo.*, vol. 2, no. 2, pp. 203-223, 1995.

[9] T. Sakurai, K. Naono, M. Egi, M. Igai, H. Kidachi, and M. Shoji, "Proposal and Evaluation of AC-IDR(s) Method That Combines High-

Performance with High Accuracy," *IPSJ Tech. Rep., HPC*, pp. 49-54, 2008. (in Japanese)

[10] M. B. van Gijzen and P. Sonneveld, "An IDR(*s*) variant with minimal intermediate residual norms," *Proc. Int. Kyoto-Forum on Krylov Subspace Method*, pp. 85-92, 2008.

[11] M. B. van Gijzen and P. Sonneveld, "An Elegant IDR(*s*) Variant that Efficiently Exploits Bi-orthogonality Properties," *Delft University of Technology, Reports of the Department of Applied Mathematical Analysis,* Report 08-21, 2008.

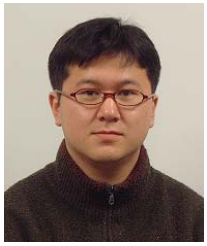

Norimasa Nakashima received the B.E., M.E., and D.E. degrees from Kyushu University, Fukuoka, Japan in 1999, 2001, and 2004, respectively. He joined Kyushu University as a research associate in 2004. He is currently an Assistant Professor of Faculty of Information Science and Communication Engineering, Kyushu University, Japan. His research interest is in computational electromagnetics. He is a member of IEICE, JSIAM, and the IEEE.

Seiji Fujino received the B.E. degree in Mathematics in 1974 from Kyoto University, Kyoto, Japan. Moreover, He received the D.E. in 1993 from the University of Tokyo, Tokyo, Japan. He is currently a Professor of Research Institute for Information Technology, Kyushu University, Japan. His research interest is in iterative methods and its preconditioning for linear systems. He is a member of Japan SIAM, IPSJ, JSCES, and JSST, respectively.

Mitsuo Tateiba received the B.E. and M.E. degrees in Electronics in1967 and 1969, respectively, and the D.E. degree in communication engineering in 1977, all from Kyushu University, Fukuoka, Japan. He joined the Faculty of Engineering, Kyushu University as a Research Associate in 1969, an Associate Professor in 1983 and a Professor in 1990. He served as a Vice-Dean of Graduate School of Computer Science and Communication Engineering of the same University in 2004 and the Dean of the same School from 2005 to 2008. Since 2008, he has been in charge of the President of Ariake National College of Technology and a Professor Emeritus of Kyushu University. He was an Associate Professor of Nagasaki University from 1977 to 1983 and a Visiting Professor of the University of Washington in 1994. His research has been on wave theory of propagation and scattering in random media and its applications to radar engineering, satellite communications, remote sensing, and diffraction tomography. He is a member of the IEE of Japan, IOP, IEEE and an associate member of the Science Council of Japan.

A Search-and-Track Algorithm for Controlling the Number of Guided Modes of Planar Optical Waveguides with Arbitrary Refractive Index Profiles

Tarek A. Ramadan

Department of Physics Kuwait University, Safat-13060, Kuwait
and
Electronics and Electrical Communication Engineering Department
Ain Shams University, Abbasia 11517, Cairo, Egypt
Tarek.ramadan@ku.edu.kw

Abstract ─ A search-and-track algorithm is proposed for controlling the number of guided modes of planar optical waveguides with arbitrary refractive index profiles. The algorithm starts with an initial guess point in the parameter space that supports a specific number of guided modes. Then, it searches for, and tracks, the boundaries of this space or another space supporting a different number of modes. It does so by monitoring the sign of a unified cutoff dispersion function. The algorithm is applied to both symmetric and asymmetric silicon-based parabolic-index waveguides. It shows that unlike asymmetric waveguides, the single-mode condition of symmetric waveguides is controlled by TM-, as opposed to TE-, polarization. This abnormal polarization control is strongest for high index contrast waveguides of sub-micrometer core sizes. The results are verified by the full-vectorial beam propagation method.

Index Terms ─ EM propagation, integrated optics, numerical analysis, optical waveguides, waveguide theory.

I. INTRODUCTION

Identifying the optical waveguide parameters which support a specific number of modes is a key step that precedes the design of any photonic integrated circuit. In a few special cases, exact analytical expressions of these parameters are available [1]. In most of the other cases, they are only identified by approximate or numerical computational approaches [2-11]. The inherent assumptions and/or approximations in many of these approaches limit their application to specific regions of the parameter space. Other numerically intensive computational approaches [11] consume a considerable amount of time in generating design curves which map waveguide parameters to the number of guided modes.

The purpose of this paper is to develop an algorithm for controlling the number of modes of planar waveguides of an arbitrary refractive index profile, which combines simplicity and generality. The algorithm applies to both strong- and weak-guiding conditions and discriminates between TE and TM polarizations. It starts with *a priori* knowledge of waveguide parameters which support an initial number of guided modes. Then, it monitors the sign of a unified cutoff dispersion function to allocate the boundaries of the parameter space which supports the required number of modes. It identifies this space without direct solution of the dispersion equation. The algorithm reveals an abnormal TM-polarization dependence of the single-mode condition (SMC) of symmetric parabolic-index waveguides. This dependence is verified by computations done by full-vectorial beam propagation method (FV-BPM) [12]. To the best of our knowledge, this peculiar result has not been previously reported. It mainly affects the design of high index contrast waveguides with sub-micrometer core sizes.

II. BACKGROUND THEORY

A. Differential mode counting

The number of guided modes supported by an optical waveguide may change by changing any of its geometrical or refractive index parameters. The requirement that the effective refractive index, n_e, of each guided mode must cross-over the substrate refractive index, n_s, as the mode becomes guided or leaks into the substrate, implies a change in the sign of the corresponding dispersion function at cutoff [3]. It allows computing the number of modes at any point of the parameter space in terms of the number of modes at another reference point by counting the number of changes in the sign of the cutoff dispersion function along an arbitrarily chosen path between these points. This count must exclude the changes in this sign due to poles of the dispersion function, which may crossover the cutoff point along that path. It is the basis of the search-and-track (SAT) algorithm presented in this paper.

B. Discretization model

Consider the case of a planar waveguide with core thickness *t,* upper cladding thickness *h*, and a semi-infinite substrate. Its cover and substrate refractive indexes are n_a and n_s, respectively. Its core refractive index has a maximum, n_c, and a minimum, which is greater than n_s. It is converted by discretization to a nonuniform stack of L step-index layers of thickness Δt_l and refractive index n_l. The recurrence dispersion function of this stack is obtained in terms of the normalized propagation constant, $b=(\delta_e-1)/(\delta_f-1)$, following the approach in [13]. Here, $\delta_e=n_e^2/n_s^2$, and $\delta_f=\max_l\left(n_l^2/n_s^2\right)$, which limits b between zero and unity. The cutoff dispersion function of this stack, C_L, is obtained by taking the limit of the dispersion function as $b\to 0$. It is given by (1) where, $\kappa_{l+1}=\eta_{l,l+1}\csc^2(\Delta T_l)$, $\rho_{l+1}=\cot(\Delta T_{l+1})+\eta_{l,l+1}\cot(\Delta T_l)$, $\eta_{l,l+1}=(\varepsilon_l/\varepsilon_{l+1})\sqrt{(\delta_{l+1}-1)/(\delta_l-1)}$, $\hat{\kappa}_2/\kappa_2=\left(1+\sigma^2\right)/\left((1+\gamma_a\sigma)+(\sigma-\gamma_a)\cot(\Delta T_1)\right)$, $\hat{\rho}_2=\rho_2+(\hat{\kappa}_2-\kappa_2)/C_1$, $\sigma=H/\varepsilon_1+1/\varepsilon_a\sqrt{a}$, and $\gamma_a=\left(1-a\varepsilon_a^2\right)/2\varepsilon_a\sqrt{a}$. The cutoff dispersion function, $C_1=\cot(\Delta T_1)-\sigma$. The normalized parameters, $\Delta T_l=(2\pi/\lambda_o)\Delta t_l\sqrt{n_l^2-n_s^2}$, and $H=(2\pi/\lambda_o)h\sqrt{n_1^2-n_s^2}$, where λ_o is the free-space wavelength. The asymmetry parameter, $a=\left(n_s^2-n_a^2\right)/\left(n_1^2-n_s^2\right)$, the stack-layer refractive index parameter, $\delta_l=n_l^2/n_s^2$, and the polarization parameters, $\varepsilon_l=\varepsilon_a=1$ for TE modes, while $\varepsilon_l=\delta_l$ and $\varepsilon_a=n_1^2/n_a^2$ for TM modes.

$$C_L=\det\begin{pmatrix}\rho_L & \kappa_L & & & & & \\ 1 & \rho_{L-1} & \kappa_{L-1} & & & & \\ & 1 & \rho_{L-2} & \kappa_{L-2} & & & \\ & & \bullet & \bullet & \bullet & & \\ & & & 1 & \rho_{l+1} & \kappa_{l+1} & \\ & & & & \bullet & \bullet & \bullet \\ & & & & & 1 & \hat{\rho}_2 & \hat{\kappa}_2 \\ & & & & & & 1 & C_1\end{pmatrix}. \quad (1)$$

C. Interference of pole crossing with mode counting

The dispersion function has two groups of poles. The poles of the first group are given by, $b_l^{(1)}=(\delta_l-1)/(\delta_f-1)$. Each stack layer generates one of these poles. They never cross the cutoff point (b=0) due to changing any of the waveguide parameters. The poles of the second group are given by, $b_{l,p}^{(2)}=b_l^{(1)}\left(1-p^2\pi^2/\Delta T_l^2\right)$, where p = 1,2,.., $\lfloor \Delta T_l/\pi \rfloor$, for each stack layer of $\Delta T_l\geq\pi$. Here, $\lfloor x \rfloor$ denotes the floor of x. One of these poles crosses the cutoff point each time ΔT_l equals an integer multiple of π along any path in the parameter space. To investigate the effect of this crossing on the sign of C_L, the normalized thickness of the l^{th} layer in the vicinity of $q\pi$ is expressed as, $T_l=q\pi\pm\Delta$, where q is a positive integer and Δ is infinitesimally small. Only C_{l+1} (the minor indicated in (1)) depends on T_l through the $\cot(T_l)$ and $\sec^2(T_l)$ terms of the three parameters, ρ_l, ρ_{l+1}, and κ_{l+1}. These terms become infinitely high when Δ tends to zero. Therefore, with the assumption that no other normalized thickness is an integer multiple π, they dominate over other terms, which results in, $\rho_l=\pm 1/\Delta$, $\rho_{l+1}=\pm\eta_{l,l+1}/\Delta$, and $\kappa_{l+1}=\eta_{l,l+1}/\Delta^2$,

where we have used $\cos(\Delta)\approx 1$ and $\sin(\Delta)\approx \Delta$. These approximations become exact in the limit when $\Delta \to 0$. Now, $C_{l+1} = (\pm \eta_{l,l+1}/\Delta)C_l - (\eta_{l,l+1}/\Delta^2)C_{l-1}$ while $C_l = (\pm 1/\Delta)C_{l-1} - \kappa_l C_{l-2}$. Therefore, $C_{l+1} = (\mp \eta_{l,l+1}\kappa_l/\Delta)C_{l-2}$, which changes its sign when T_l crosses $q\pi$. Next, filtering out C_{l+1} from the determinant of (1), allows writing C_L as the product of C_{l+1} and the matrix,

$$U_L^l = \det\begin{pmatrix} \rho_L & \kappa_L & & & \\ 1 & \rho_{L-1} & \kappa_{L-1} & & \\ & 1 & \rho_{L-2} & \kappa_{L-2} & \\ & & \bullet & \bullet & \bullet \\ & & & 1 & \rho_{l+2} \end{pmatrix}, \quad (2)$$

where we have used $1/C_{l+1} = (\mp \Delta/\eta_{l,l+1}\kappa_l)(1/C_{l-2}) \to 0$ as $\Delta \to 0$. Since U_L^l is independent of T_l, then the limit, $\lim_{\Delta\to 0} C_L = (\lim_{\Delta\to 0} C_{l+1})(\lim_{\Delta\to 0} U_L^l) = \pm\infty$, which shows that C_L must change its sign when T_l crosses $q\pi$. This change in sign does not correspond to an increase or a decrease in the number of supported modes.

III. PROPOSED ALGORITHM

A. Search-and-track approach

In order to identify the closed space of generalized waveguide parameters *u* and *v*, which support a specific number of guided modes, *M*, the proposed algorithm starts with an initial guess of a point that either belongs to this space (see point 1 in Fig.1) or to a space supporting M_o modes, which is different from *M*. For example, a point in the n_c-t space with an initial maximum core refractive index, n_{co}, and an initial thickness, t_o. This initial guess may either be obtained using different physical and/or mathematical bounds (see below).

After choosing the initial guess point (IGP), the algorithm searches for a point on the space boundaries. For example, the boundary between the spaces supporting *M* and *M*+1 modes shown in Fig. 1. It does so by moving along a single dimension in the horizontal or the vertical direction of the *u*-*v* space in infinitesimally small steps starting from the IGP, keeping the other space dimension unchanged, see Fig. 1. In moving along either of the horizontal or vertical search paths, it monitors the sign of C_L. Any unwanted sign changes due to function poles crossing the cutoff point are filtered out, as described below. Once the number of sign changes exceeds the absolute difference between *M* and M_o, the motion along the horizontal (or vertical) dimension stops and the preceding point along the search path represents a point on the boundary that encloses the target space, which supports the required number of modes, *M*. See the flow chart in Fig. 2(a) for a description of the search loop.

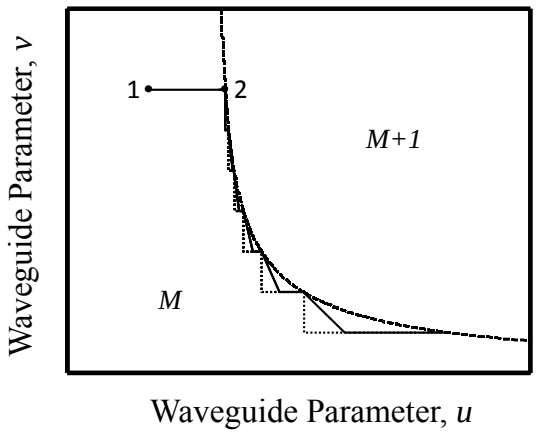

Fig. 1. A horizontal search path extending from an initial guess point 1 (with M_o = *M*) to point 2, which represents the origin of the track, followed by a downward staircase (dotted) or linear (solid) track of the boundary (dashed) between two *u*-*v* parameter spaces supporting *M* and *M*+1 modes. Although not shown, vertical search paths as well as upward staircase tracks may also be followed which results in four search and track possibilities.

The boundary point 2, allocated by the search loop, is the origin of a staircase path that tracks that boundary, see Fig. 1. It is created by a step decrease (or increase) in the vertical (or horizontal) parameter of the *u*-*v* space starting from this origin point, followed by a search for a new boundary point along the horizontal (or vertical) search dimension of the *u*-*v* space. This step-and-search process continues until sufficient points are allocated to reconstruct the space boundary within a predefined computational window. It requires *a priori* knowledge of the

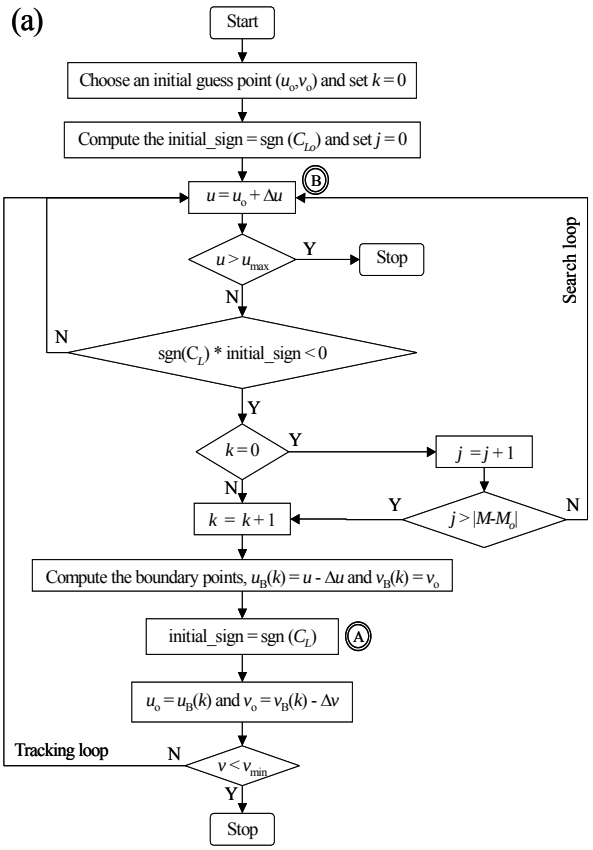

Fig. 2. (a) A flow chart description of a horizontal-search and downward-tracking algorithm. It assumes that u and v have opposite tracking directions. The index j counts the number of sign changes along the search path between points 1 and 2 of Fig.1. The index k counts the boundary points. The parameter L_o represents the number of discretization layers at the IGP, which, in general, may change to L as u or v changes. The vectors u_B and v_B are the u- and v-coordinates of the space boundary. Vertical search interchanges u and v in the search loop while upward tracking interchanges them in the tracking loop.

shape of the boundary to determine the directions of increasing or decreasing u and v along the track. These directions are governed by a general rule, which is described below. The staircase tracking loop is described in the flow chart of Fig. 2(a).

If the search path increases with the tracking steps, for example as in the n_c-t space,[1] then the

[1] The upper or lower boundary of an n_c-t space supporting M modes satisfies the asymptotic conditions, $n_c \to n_s$ when $t \to \infty$ and $n_c \to \infty$ when $t \to 0$. These conditions, in addition to the monotonic change of t and n_c along the boundary, imply that $\partial t/\partial n_c < 0$ and $\partial^2 t/\partial n_c^2 > 0$. Thus, the search path along n_c increases as t decreases along the track.

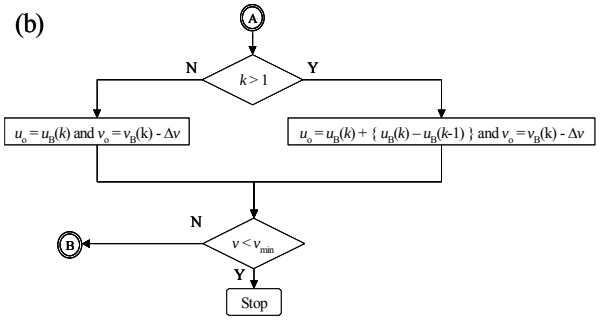

Fig. 2. (b) A flow chart description of linear downward tracking that substitutes the flow chart in (a) in going from A to B. Staircase tracking is initially followed (when k=1) until two or more boundary points (k>1) are allocated.

computations of the space boundary may be speeded up by using linear tracking. This tracking interpolates between the last two boundary points to predict the location of the third boundary point. Then, it searches for the actual boundary point starting from this predicted point, which is closer to the space boundary compared to the staircase tracking approach, see Fig. 1. It may be regarded as a modification of the staircase tracking in which a horizontal step is added to the vertical step in going from an actual boundary point to a predicted boundary point (a bottom corner point of the stair). The horizontal step equals the difference in u between the last two boundary points, as shown by the flow chart of Fig. 2(b). This interpolation process continues along the track, which shortens the overall search length and reduces the CPU computational time.

B. Tracking rule

As a preliminary step towards developing a tracking rule which specifies the directions of increasing or decreasing u and v along the boundary between two spaces, we classify waveguide parameters into two types depending on whether their increase may add modes to, or

subtract modes from, the waveguide. Next, the number of modes supported by the array is expressed as a two dimensional function $M(u,v)$ in the *u*-*v* space. The dependence of *M* on other waveguide parameters is suppressed for simplicity. Let $Y(u,v)$ be a randomly selected continuous differentiable function associated with *M*, which satisfies the relation, $\lfloor Y \rfloor = M$. The value of *Y* at the upper or lower boundary of the space supporting *M* modes is denoted by Y_B. In the vicinity of this boundary, $Y = Y_B + \Delta Y$, where ΔY represents a first-order perturbation from Y_B. This perturbation may be expanded by the first-order terms of a Taylor series, $\Delta Y = (\partial Y/\partial u)_B \Delta u + (\partial Y/\partial v)_B \Delta v$, around the boundary. For all functions *Y*, which satisfy $\lfloor Y \rfloor = M$, their derivatives in this expansion must be positive for mode-adding parameters and negative for mode-subtracting parameters. If this is not the case, then it would contradict the definition of these derivatives which are computed at the boundaries of the space where *u* and *v* have their extreme values (minima (maxima) for mode-subtracting parameters and maxima (minima) for mode-adding parameters at the upper (lower) boundary). The relation between Δu and Δv at the boundary (upper or lower) is obtained by setting $\Delta Y = 0$ in the Taylor expansion. It gives,

$$\Delta v = -(\partial Y/\partial u)_B / (\partial Y/\partial v)_B \, \Delta u \, . \qquad (3)$$

According to (3), Δu and Δv must have opposite (similar) signs whenever $(\partial Y/\partial u)_B$ and $(\partial Y/\partial v)_B$ have similar (opposite) signs. This result leads to a simple tracking rule, which states that: two waveguide parameters of the same type must have opposite tracking directions (if one decreases, then the other increases and vice versa) while those of different types must have the same tracking direction (both increase or decrease) along the boundaries of the parameter space supporting a specific number of modes. For example, the increase in either of the thickness *t* or the maximum core refractive index n_c of an optical waveguide never decreases the number of guided modes. It either increases it or keeps it constant. Therefore, *t* and n_c must have opposite tracking directions along the boundaries of a specific space. Inspection of the waveguide design parameters leads to the conclusion that, except for the substrate refractive index, n_s, all other parameters (including *t*, *h*, n_c, and n_a) are mode-adding parameters. Note that the cover refractive index is constrained by, $n_a \le n_s$. Since the free-space wavelength is a mode-subtracting parameter, normalization of any of the mode-adding parameters by λ_o does not change their type.

C. Filtering out sign changes due to poles

In order to filter out sign changes due to poles, it is sufficient to flip the sign of C_L at each crossing of a pole during the search loop; see the flow chart of Fig. 2(a). If these sign changes are not filtered out, they result in a premature termination of the search path and faulty locations of the boundary points of the parameter space. An alternative approach eliminates the crossing of poles by satisfying the condition, $\max_l \Delta t_l < \lambda_o \big/ 2\sqrt{n_c^2 - n_s^2}$, which ensures that all the layers of the stack are single moded ($\Delta T_l < \pi$). This elimination is only possible in graded-index waveguides. In other more general cases of refractive index profiles, which include step-index layers, e.g. in [14], the thickness of the step-index layers may exceed the maximum imposed by this condition. Hence, the above rule of flipping the sign of C_L at the crossing of each pole must be applied.

IV. APPLICATIONS

A. Modal maps

In this section, the SAT algorithm identifies waveguide parameters, which support different number of TE and TM modes. Since the number of modes supported by a step-index waveguide whose core refractive index is n_c (and shares all other waveguide parameters) represents an upper bound, the algorithm starts by choosing an IGP, which belongs to the space supporting the minimum number of modes (zero for asymmetric guides and one for symmetric guides). This choice allows selecting any combination of *u* and *v* of this step-index waveguide as an IGP. Next, the algorithm allocates the upper boundary of the space, which supports the initial number of modes, as explained in Section III. Then, the computations follow a sequential approach in allocating the

boundaries of the subsequent spaces. In these sequential computations, the upper boundary of one space is the lower boundary of the subsequent space. Thus, allowing sequential generation of the IGPs of the successive spaces, as their boundaries are constructed. The accuracy of the generated IGPs is verified by monitoring the flip in the sign of the cutoff dispersion function between successive spaces excluding those due to pole crossings. The final outcome is a two-dimensional modal map of selected waveguide parameters, which support different number of modes.

B. Asymmetric profiles

Consider the case of an optical waveguide made of a-SiO_x:H [15]. The waveguide parameters are h=0, n_a=1, n_s=1.45, $n(x)=1.6\sqrt{1-0.062\left((x/t_1)-1\right)^2}$ for $0<x<t_1$ and n(x) = 2.0 for $t_1<x<t_1+t_2\,(=t)$, where the x-axis has its origin at the cover-cladding interface and points towards the substrate. Its modal map was computed in the t_2-t_1 plane (replacing u with t_2 and v with t_1) using a MATLAB code which employs a vertical search with a downward staircase-tracking algorithm and follows the sequential approach described above. The algorithm starts with an IGP (t_1=0.1 μm, t_2=0.1 μm) in the space supporting zero modes. The computational steps along t_1 and t_2 are both equal to 10^{-2} μm. The choice of a uniform stack layer thickness of 10^{-3} μm in the graded-index layer eliminates the crossing of poles as t_1 increases. The pole filtering rule switches the sign of the cutoff dispersion function each time the normalized thickness of the step-index layer crosses $q\pi$ as t_2 increases. The resultant modal map is shown in Fig. 3. It identifies combinations of t_1 and t_2 which support different number of TE and TM modes.

As an example of the computations of the modal map in the η–t plane (replacing u with $\eta\left(\equiv\left(n_c^2-n_s^2\right)/2n_c^2\right)$ and v with t), consider a truncated parabolic-index waveguide with h=0, n_a=1, n_s = 1.45, and $n(x)=n_c\sqrt{1-2\eta(x/t)^2}$ for $0<x<t$. Its modal map was computed at λ_o=1.55 μm as described above, however, horizontal search was used, as opposed to vertical search, starting from an IGP (t=5 μm, n_c=1.45001). The results are shown in Fig. 4. It identifies

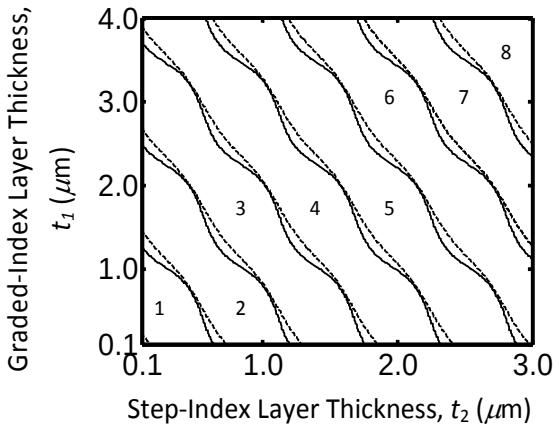

Fig. 3. Modal map of TE (solid) and TM (dashed) modes of a planar waveguide of a truncated parabolic index layer of thickness t_1 grown on top of a step-index layer of thickness t_2 computed at λ_o=1.55 μm. The other waveguide parameters are h=0, n_a=1, and n_s=1.45. The number of modes is indicated in each zone. Because of its small size, the zone supporting zero modes almost disappears.

combinations of t and η which support different number of TE and TM modes. The overall CPU times for these computations are 638 s and 659 s for the TE- and TM-modes, respectively. If linear tracking is used (see Section III-A) with the same IGPs to generate this modal map, then the CPU times reduce to 332 s and 380 s, for the TE- and TM-modes, respectively. This reduction represents 45% saving in the overall computational time.

The accuracy of the above modal maps has been verified using a FV-BPM simulator, which employs an iterative mode computational technique [12]. Because of the unlimited time needed to scan the parameter spaces of the entire modal maps, computations of the number of modes were carried out by changing the horizontal parameter of each map in steps at arbitrarily selected values of its vertical parameter (t_1 in the modal map of Fig. 3 and t in the modal map of Fig. 4). The results (not shown) show excellent agreement between these modal maps and the FV-BPM computations for both TE and TM polarizations.

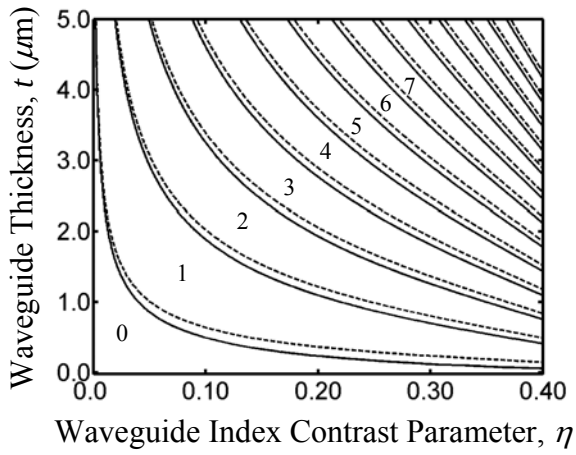

Fig. 4. Modal map of TE (solid) and TM (dashed) modes of a truncated parabolic-index waveguide with $h = 0$, n_a=1, and n_s=1.45 computed at λ_o=1.55 μm, showing parameters of the η–t space supporting zero to twelve modes.

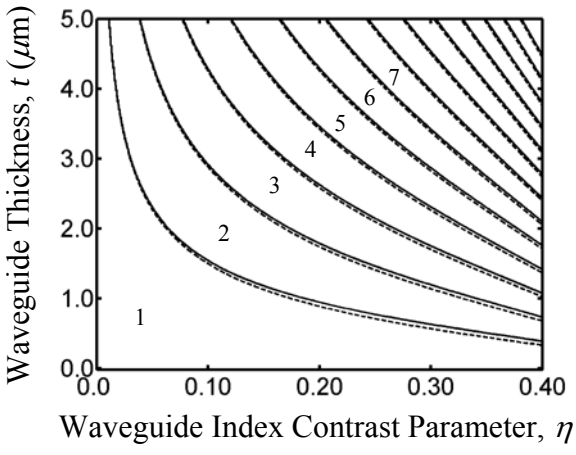

Fig. 5. Modal map of TE (solid) and TM (dashed) modes of a symmetric parabolic-index waveguide with n_s=1.45 computed at λ_o=1.55 μm, showing parameters of the η–t space supporting one to thirteen modes.

C. Symmetric profile

To investigate the effect of symmetry on the modal map, a symmetric parabolic-index waveguide is considered. Its core refractive index is $n(x) = n_c\sqrt{1-8\eta(x/t-1/2)^2}$ for $0 < x < t$ while n_s = 1.45. The SAT algorithm starts with the same IGP (t=5 μm, n_c=1.45001), which now belongs to the parameter space supporting a single mode. It uses the same numerical parameters and free-space wavelength as in the previous section. The computed modal map is plotted in Fig. 5. The CPU computational times of the TE and TM modes, using staircase tracking, are 666 s and 684 s, respectively. Again, linear tracking reduces these CPU times to 349 s and 360 s, respectively, which saves 47% of the overall computational time. The modal map of Fig. 6 shows that the splitting in cutoff boundaries between the TE and TM modes is inverted. Namely, unlike the asymmetric waveguides, the cutoff t (or η) of the TM modes is smaller than that of the TE modes at any η (or t). This inversion means that, under SMC, the maximum waveguide thickness equals the cutoff thickness of the first-order TM-, as opposed to TE- mode. Therefore, operating under single TE-mode condition does not ensure simultaneous single-mode operation of both modal polarizations in symmetric parabolic-index waveguides. This result has not been previously reported by various approximate methods which analyzed these symmetric waveguides, e.g. in [2, 5, 6].

D. FV-BPM computations

In order to verify this abnormal polarization dependence of the SMC, a symmetric parabolic-index waveguide parameters, $n_c = 2.55$ (η=0.34) and $t = 0.5$ μm, were selected, which support two TM modes and a single TE mode. They correspond to a point between the cutoff boundaries of the TM_1 and the TE_1 modes in the modal map of Fig. 5. Next, the FV-BPM simulator used in Section IV-B computed the modes of this guide at λ_o=1.55 μm. The results of these computations show that the waveguide supports two TM modes and a single TE mode. The computed modal field profiles are shown in Fig. 6. While these results are in agreement with the modal map computations, further verification was carried out to exclude any error in the mode excitation conditions of the FV-BPM computations. It is done by selecting a design point ($n_c = 2.55$ and $t = 0.6$ μm) from the modal map of Fig. 5, just above the cutoff boundary of the TE_1 mode. Then computing the effective index of the TM_1 mode (n_e=1.470229) and verifying that it is, indeed, greater than the effective index of the TE_1 mode (n_e=1.460989).

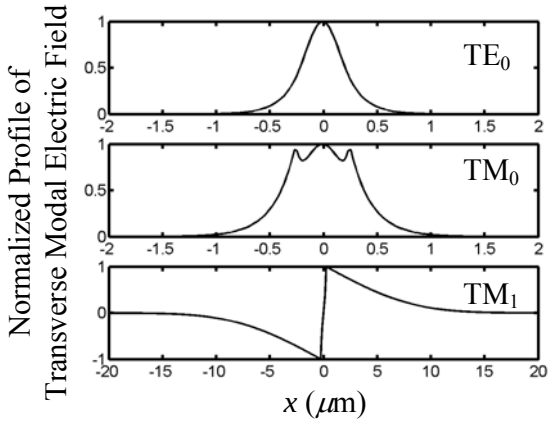

Fig. 6. Transverse electric-filed distribution of the TE_0 (top), TM_0 (middle), and TM_1 (bottom) modes of a symmetric parabolic-index waveguide with t=500 nm, n_c = 2.55, and n_s=1.45, computed by FV-BPM at λ_o=1.55 μm. The field is normalized to a maximum of unity.

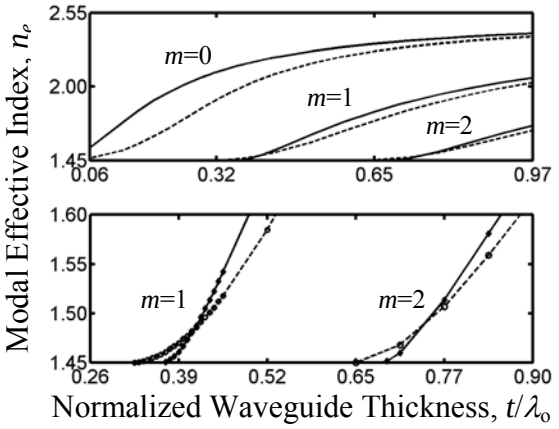

Fig. 7. Effective index n_e versus t/λ_o for the first three TE (solid) and TM (dashed) modes of a symmetric parabolic-index waveguide with n_c = 2.55 and n_s=1.45, computed by FV-BPM. Below is a zoom-in on the dispersion curves of the first-order (m=1) and the second-order (m=2) modes near their cutoff.

Full dispersion information was obtained by repetitive FV-BPM computations of n_e, as the waveguide thickness increased in steps from 0.1 μm to 1.5 μm, at λ_o=1.55 μm. The resultant dispersion curves are plotted in Fig. 7. It shows that, starting form the first-order mode (m=1), the dispersion curves of the TM and TE polarizations intersect near cutoff. This intersection leads to lower cutoff thickness of the higher-order TM modes compared to TE modes. Above the intersection thickness, the dispersion curves follow their normal behavior where the effective index of the TE modes is greater than the TM modes. Below this thickness, this relation is inverted and a range of thickness arises (between the cutoffs of the higher-order TM and TE modes) where an extra TM mode is supported. This range is where the modes of Fig. 6 were computed. This result is, again, consistent with the modal map computations and is a logical outcome of the inversion of the modal cutoff, which verifies the utility of the proposed algorithm.

E. Abnormal parameter space

In order to investigate the effect of the upper cladding layer thickness on the TM polarization dependence of the SMC, we consider an asymmetric parabolic waveguide with fixed n_s = 1.45, n_a = 1, η = 0.1 (n_c=1.62), and a variable h. It becomes a symmetric waveguide (as in Section IV-C) in the limit as $h \to \infty$. The cutoff thickness of the TE_1 and TM_1 modes of this guide were computed at different h at λ_o = 1.55 μm. The computations applied a vertical search with a downward stair-tracking algorithm to the h-t plane (replacing u with h and v with t). They started from an IGP (h=0.1 μm and t=0.1 μm) which supports zero modes (M_o=0), skipped a single sign change on the search path (corresponding to j=1 in the flow chart of Fig. 2(a)) to reach a point on the upper boundary of the target parameter space, which supports a single mode (M=1). Next, they followed opposite tracking directions along that boundary, according to the tracking rule of Section III-B. Figure 8 plots the computed cutoff waveguide thickness of the first-order TE and TM modes versus h. As expected, the cutoff thickness of the TM_1 mode starts higher (at low h), gradually decreases (with increasing h), and ends up lower than the cutoff thickness of the TE_1 mode. The upper cladding thickness h=730 nm at the point of intersection is the minimum h which results in an abnormal TM-polarization control of the SMC in this specific example. For further understanding of this abnormal polarization control, recomputations of the modal map of Fig. 4 (in the η–t space) were carried out replacing h=0 with h=730 nm. The new modal map (not shown) shows an intersection between the cutoff thickness of the TE_1 and TM_1

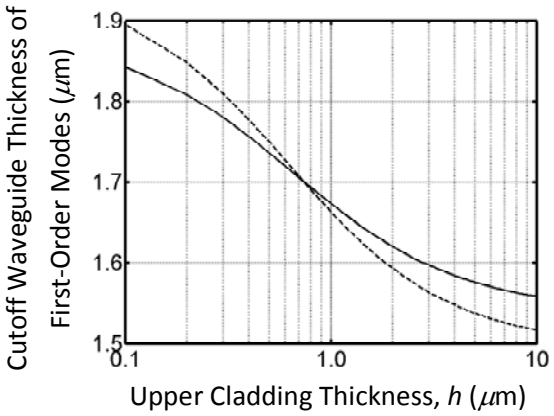

Fig. 8. Cutoff thickness of TE_1 (solid) and TM_1 (dashed) modes versus upper cladding thickness h for a parabolic-index waveguide with η=0.1, n_s=1.45, and n_a=1, computed at λ_o = 1.55 μm.

modes (upper boundaries of the M=1 space) at η=0.1 and t=1.7 μm. They show that at any t>1.7 μm (η<0.1) the SMC is controlled by the TE mode, otherwise (t<1.7 μm and η>0.1) it is controlled by the TM mode. Thus, the common waveguide cutoff thickness at the intersection point in Fig. 8 represents the maximum t which results in abnormal TM-polarization control of the SMC at h=730 nm.

In order to identify the boundary between the normal and abnormal spaces in the t-h plane, Fig. 9(a) plots h against this common cutoff thickness of the TE_1 and TM_1 modes, as η changes between 0.04 and 0.4. It identifies the combinations of t and h where the SMC is controlled by the TE (normal) or the TM (abnormal) mode. Figure 9(b) plots the same h against η to identify the same boundary between the normal and abnormal spaces in the η-h plane. Both figures show that the minimum h of the abnormal space decreases with decreasing t or increasing η. This decrease in the minimum h implies the need of a lower h in the case of high-index contrast waveguides of sub-micrometer core sizes to sustain the normal TE control of the SMC.

V. CONCLUSION

A numerical algorithm has been proposed for the design of planar optical waveguides with arbitrary refractive index profiles. The algorithm identifies the waveguide parameters, which support different number of modes. It is exact in the sense that the discretization error may

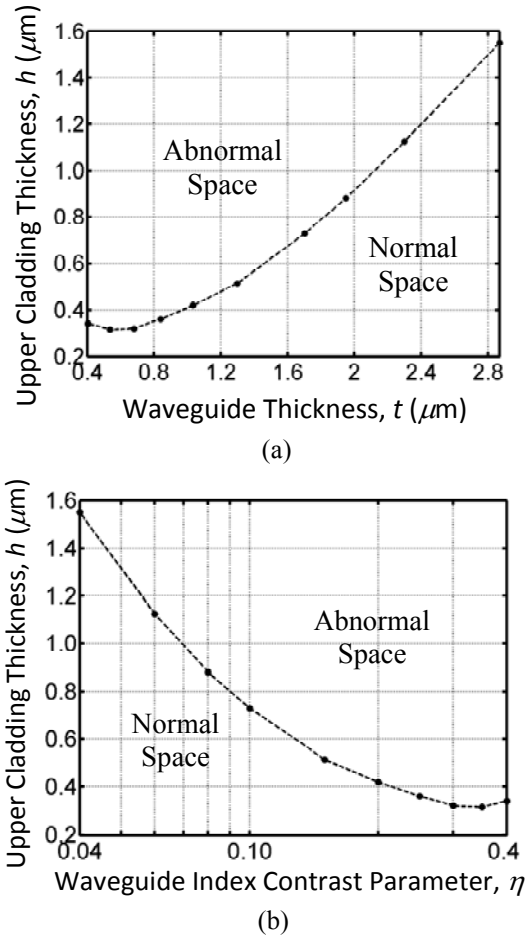

Fig. 9. Boundary between normal and abnormal regions of the (a) t-h and (b) η–h space of a parabolic-index waveguide with n_s=1.45 and n_a=1 computed at λ_o=1.55 μm.

arbitrarily be minimized by increasing the number of stack layers. It may be combined with genetic algorithms [16, 17] to optimize the performance of planar integrated optical devices under the constraint of supporting a specific number of modes using the appropriate cutoff function.

Application of the algorithm to symmetric and asymmetric parabolic-index waveguides reveals a fundamental difference between the modal polarizations which control the number of their guided modes. If the upper cladding thickness is greater than some critical thickness, which decreases under high index contrast and/or small core sizes, then this number is controlled by TM polarization. Otherwise, it is controlled by TE polarization.

REFERENCES

[1] M. J. Adams, *An Introduction to Optical Waveguides*, Wiley, New York, 1981.

[2] V. Ramaswamy and R. K. Lagu, "Numerical Field Solution for an Arbitrary Asymmetrical Graded-Index Planar Waveguide," *J. Lightw. Technol.*, vol. LT-1, no. 2, pp. 408-417, 1983.

[3] S. Ruschin, G. Griffel, A. Hardy, and N. Croitoru, "Unified Approach for Calculating the Number of Confined Modes in Multilayered Waveguiding Structures," *J. Opt. Soc. Amer. A*, vol. 3, no. 1, pp. 116-123, 1986.

[4] A. K. Ghatak, K. Thyagarajan, and M. R. Shenoy, "Numerical Analysis of Planar Optical Waveguides using Matrix Approach," *J. Lightw. Technol.*, vol. LT-5, no. 5, pp. 660-667, 1987.

[5] J. P. Donnelly and S. D. Lau, "Generalized Effective Index Series Solution Analysis of Waveguide Structures with Positionally Varying Refractive Index Profiles," *IEEE J. Quantum Electron.*, vol. 32, no. 6, pp. 1070-1079, 1996.

[6] H. Ding and K. T. Chan, "Solving Planar Dielectric Waveguide Equations by Counting the Number of Guided Modes," *IEEE Photon. Technol. Lett.*, vol. 9, no. 2, pp. 215-217, 1997.

[7] L. Wang and N. Huang, "A New Numerical Method for Solving Planar Waveguide Problems with Arbitrary Index Profiles: TE Mode Solutions," *IEEE J. Quantum Electron.*, vol. 35, no. 9, pp. 1351-1353, 1999.

[8] M. S. Chung and C. M. Kim, "General Eigenvalue Equations for Optical Planar Waveguides with Arbitrarily Graded-Index Profiles," *J. Lightw. Technol.*, vol. 18, no. 6, pp. 878–885, 2000.

[9] K. Mehrany and B. Rashidian, "Polynomial Expansion for Extraction of Electromagnetic Eigenmodes in Layered Structures," J. *Opt. Soc. Amer. B.*, vol. 20, no. 12, pp. 2434-2441, 2003.

[10] N. Zariean, P. Sarrafi, K. Mehrany, and B. Rashidian, "Differential-Transfer-Matrix Based on Airy's Functions in Analysis of Planar Optical Structures with Arbitrary Index Profiles," *IEEE J. Quantum Electron.*, vol. 44, no. 4, pp. 324-330, 2008.

[11] R. Scarmozzino, A. Gopinath, R. Pregla, and S. Helfert, "Numerical Techniques for Modeling Guided-Wave Photonic Devices," IEEE *J. Sel. Topics Quantum Electron.*, vol. 6, no. 1, pp. 150-162, 2000.

[12] G. R. Hadley and R. E. Smith, "Full-Vector Waveguide Modeling using an Iterative Finite-Difference Method with Transparent Boundary Conditions," *J. Lightw. Technol.*, vol. 13, no. 3, pp. 465-469, 1995.

[13] T. A. Ramadan, "A Recurrence Technique for Computing the Effective Indexes of the Guided Modes of Coupled Single-Mode Waveguides," *Progress In Electromagnetics Research M*, vol. 4, pp. 33-46, 2008.

[14] A. Delage, S. Janz, B. Lamontagne, A. Bogdanov, D. Dalacu, D. X. Xu, and K. P. Yap, "Monolithically Integrated Asymmetric Graded and Step-Index Couplers for Microphotonic Waveguides," *Opt. Express*, vol. 14, no. 1, pp. 148-161, 2006.

[15] K. Shiraishi and C. S. Tsai, "A Micro Light-Beam Spot-Size Converter using a Hemicylindrical GRIN-Slab Tip with High-Index Contrast," *J. Lightw. Technol.*, vol. 23, no. 11, pp. 3821-3826, 2005.

[16] D. S. Weile and E. Michielssen, "Genetic Algorithm Optimization Applied to Electromagnetics: A Review," *IEEE trans. Antennas Propagat.*, vol. 45, no. 3, pp. 343-353, 1997.

[17] D. Erni, D. Wiesmann, M. Spuhler, S. Hunziker, and E. Moreno, "Application of Evolutionary Optimization Algorithms in Computational Optics," *Applied Computational Electromagnetic Society (ACES) Journal*, vol. 15, no. 2, pp. 43-60, 2000.

Tarek A. Ramadan was born in Eldakahlia, Egypt, in 1966. He received the B.S. and M.S. degrees from the Electronics and Electrical Communication Engineering Department, Ain Shams University, Cairo, Egypt, in 1989 and 1994, and the Ph.D. degree from the Electrical Engineering Department, Columbia University, New York, in 2000.

From 1989 to 1990, he spent his military service at the Military Technical College, Cairo.

From 1990 to 1995, he was a Demonstrator and Assistant Lecturer at the Electronics and Electrical Engineering Department, Ain Shams University. From 2000 to 2007, he was an Assistant Professor at the Electronics and Electrical Communication Engineering Department, Ain Shams University. Since 2007, he has been an Associate Professor in the same department. In September 2004, he joined the Physics Department, Kuwait University, Kuwait. His research interests include analytical and numerical analysis of integrated optical components.

Dr. Ramadan was included in the 22nd edition of *Marquis Who's Who in the World* in 2005. He is a Member of IEEE Photonics society and the Optical Society of America.

Systems for Homogeneous Electrical Fields Generation and Effects of External Bodies on Field Homogeneity

Zlata Cvetkovic, Bojana Petkovic, and Mirjana Peric

Department of Theoretical Electrical Engineering
Faculty of Electronic Engineering of Nis, University of Nis, Serbia
zlata.cvetkovic@elfak.ni.ac.rs, bojana.petkovic@elfak.ni.ac.rs,
mirjana.peric@elfak.ni.ac.rs

Abstract ─ A procedure of modeling new systems consisting of thin toroidal electrodes placed at the surface of a sphere, for high homogeneity electric field generation, is presented in this paper. In order to investigate the influence of an external body shape and volume to the obtained field's homogeneity, the external object is modeled as a sphere, prolate and oblate ellipsoidal electrode and placed in the centre of the system. Numerical results, obtained using the software Mathematica 7.0 and Femm, are compared and shown graphically.

Index Terms ─ Charge simulation method, ellipsoidal conducting body, homogeneous electric field, method of images, toroidal electrodes.

I. INTRODUCTION

The problems of electric and magnetic field synthesis are of a great importance in many theoretical applications, where it is necessary to generate a field with a high accuracy and of required features. Great attention over years has been devoted to the production of a uniform magnetic field. Arrangements of coils like Helmholtz's two-coil system and Maxwell's three coils combinations are well known devices for producing a region of an approximately uniform magnetic field [1]. This case has been extended to an arbitrary number of coils placed at a virtual spherical surface [2]. A larger region of a uniform magnetic field inside a spherical coil system is achieved in [3].

Much less attention is, up to now, paid to the dual problem, i.e. to a generation of homogeneous electrical fields. A system consisting of two equal diameter charged rings produces a uniform electrical field, [4]. A very uniform electrical field near the center of the sphere is obtained using special bowl design, [5]. This is a kind of special spherical conducting surfaces at certain potentials.

In our earlier published paper [6], we extended the problem solved in [4] and modeled complex coil systems, which consist of a larger number of primary cells. The modeling process was similar to a procedure applied in [2]. Later, we investigated an effect of an external body on achieved field homogeneity of toroidal electrodes [7]. The external body is modeled as a conducting sphere and brought into the center of the observed system.

The aim of this paper is the modeling of an external body as a prolate and oblate ellipsoidal electrode and analyzing its influence on achieved filed homogeneity of a system of toroidal electrodes. Numerical results are obtained using software packages Mathematica and Femm.

II. HOMOGENEOUS ELECTRIC FIELD GENERATION

In practice, very often there is a need for getting homogeneous electric fields, with required features and of high precision. Those fields are used widely in technique: they are applied in electrical machines for high field generation, NMR spectroscopy, MHD technique, nuclear and plasma physics, so the problem of an electrostatic field is very actual from the standpoint of its realization as well as from the standpoint of its partial or complete elimination.

A. Toroidal electrodes system

By analogy to Helmholtz coils that produce an uniform magnetic field when the distance between coils is equal to the radius of the coils, it is possible to produce an uniform electrical field using two charged rings when the distance between rings is $\sqrt{6}$ times the ring radius [4].

The work described here refers to a modeling of complex systems for generating a homogeneous electric field, formed by thin coaxial toroidal electrodes. A primary cell is used as a starting element in a modeling procedure. It consists of a pair of flat toroidal electrodes which have the same radius d, separated by a distance $2h$ as in Fig. 1. The electrodes are of absolutely equal potential values, but of opposite signs. Complex systems consist of a number of primary cells placed at a virtual sphere, Fig 2.

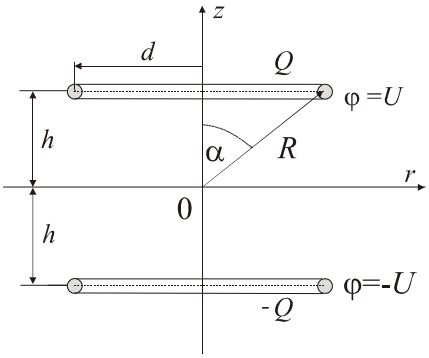

Fig. 1. A toroidal primary cell.

We shall take the z axis of a cylindrical coordinate system as being the axis of the coils, with the origin midway between the coils. In this case, the axial potential in area $|z| < R$ can be expanded in a power series, which contains only odd powers of the axial variable z [6]:

$$\phi(r=0,z)=\sum_{n=0}^{\infty}\phi_{2n+1}z^{2n+1}, \qquad (1)$$

where

$$\varphi_{2n+1}=\frac{QP_{2n+1}(\cos\alpha)}{2\pi\varepsilon R^{2n+2}}, \qquad (2)$$

$P_n(x)$ is the Legendre polynomial of the first kind, R denotes the electrode distance from the origin, $R=\sqrt{d^2+h^2}$ and $\cos\alpha = h/R$.

Since the coefficients in series (1) depend on electrodes positions and dimensions, it is possible to choose primary cell dimensions to eliminate a few subsequent terms different than linear so that a linear term becomes dominant.

For further work it is necessary to introduce the following definitions. The primary cell has N-th order, if the term φ_{2N+1} in expression (1) is equal to zero. This condition is satisfied if $P_{2N+1}(\cos\alpha)=0$. This equation, for $N\geq 1$, has N positive roots, $\cos\alpha_k = x_{2N+1,k}$, for $k=1,2,..,N$, where $x_{2N+1,k}$ are zeros of the Legendre polynomial $P_{2N+1}(x)$. Variable k defines the degeneration degree of primary cells. So the primary cell of the N-th order has N different degeneration states, i.e. shapes. All those primary cells are placed at a surface of a virtual sphere of radius R, Fig. 2.

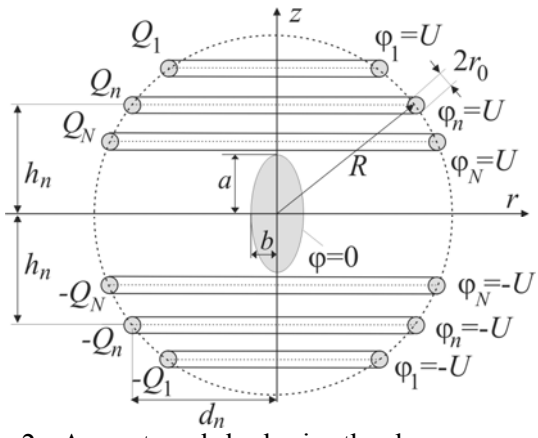

Fig. 2. An external body in the homogeneous electric field.

For the primary cell of the N-th order, the axial potential can be shown using (1), where

$$\varphi_{2n+1}=\sum_{k=1}^{N}\frac{Q_k P_{2n+1}(x_{2k+1,k})}{2\pi\varepsilon R^{2n+2}}. \qquad (3)$$

The term φ_{2N+1} is equal to zero.

In order to eliminate the influence of other series terms from z^3 to z^{2N-1}, the following system of equations has to be satisfied,

$$\varphi_{2n+1}=0, \text{ for } n=1,2,...,N-1. \qquad (4)$$

Charges of electrodes, Q_n, are obtained solving this system of equations using the condition that all electrodes are equipotential.

The field in a central region will be highly homogeneous if the contribution from the higher order terms is as small as possible. The rest of the

higher order terms can be neglected with respect to linear one.

B. Calculation of primary cell dimensions

Let us first consider a system consisting of one primary cell, i.e. two thin toroidal electrodes, Fig. 1. The electrodes dimensions are being obtained after assuming that the coefficient of z^3, given by formula (2), is equal to zero, what yields: $P_3(\cos\alpha)=0$. This equation has only one root, $\cos\alpha = 0.7745966692$, so the primary cell of the first kind has dimensions $h = 0.7745966692\,R$ and $d = 0.632455532\,R$. It is the same result as in [4].

By setting the coefficient of z^5 to zero, we get the equation that has two solutions, which define dimensions of the second order primary cell:

$$d_1 = 0.422892524\,R,\ h_1 = 0.906179846\,R,$$

$$d_2 = 0.8426544122\,R,\ h_2 = 0.538469310\,R.$$

In a general case, by setting the coefficient of z^{2N+1} to zero in (1), the primary cell of the N-th order is obtained.

Table 1 presents the dimensions of primary cells of the first to fifth order.

Table 1: Optimal system dimensions for N^{th} order primary cell

	d_5/R	d_4/R	d_3/R	d_2/R	d_1/R	
N	0.963	0.855	0.683	0.462	0.208	5
1	0.775	0.946	0.790	0.549	0.250	4
2	0.906	0.538	0.914	0.671	0.315	3
3	0.949	0.742	0.406	0.843	0.423	2
4	0.968	0.836	0.613	0.324	0.632	1
5	0.978	0.887	0.730	0.519	0.270	N
	h_1/R	h_2/R	h_3/R	h_4/R	h_5/R	

For the system dimensions presented in Table 1, the primary cells of the first and the second order are formed.

In Fig. 3, the normalized electric field along the z axis of the system with primary cells of the first and second order is shown. It is evident that the high field homogeneity is obtained in close vicinity of the central system area.

Below will be the examined effect of an external body on achieved field homogeneity of toroidal electrodes.

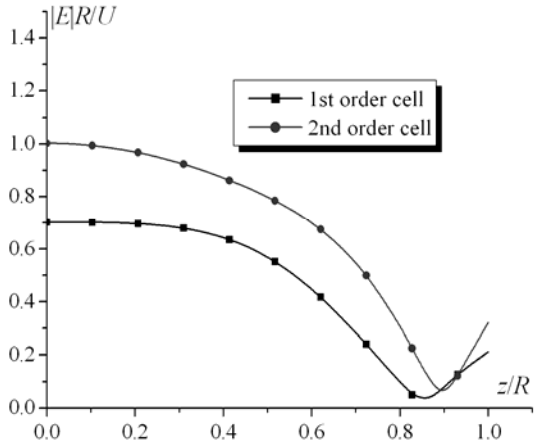

Fig. 3. Normalized electric field along z axis using primary cell of the first and second order.

III. MATHEMATICAL BACKGROUND

A. Rings charges calculation of ellipsoidal electrode

Consider a system presented in Fig. 2. The external body is firstly modeled as a prolate ellipsoidal electrode of semi-axes a and b, $a > b$, and placed into the central system area. Its centre coincides with the coordinate origin. In order to find the affection of the external prolate ellipsoid brought into the homogeneous electric field of the toroidal primary cell of N-th order, the charge simulation method [8] is used. Thin toroidal electrodes of radii

$$r_n = fb\sqrt{1-(n/(N+1))^2}$$

are used as fictitious sources and placed inside the conducting body at positions $z_n = n/(N+1)\,fa$, where f is the coefficient, $0 < f < 1$.

The potential at any point is given by the following expression:

$$\phi = \frac{1}{2\pi^2\varepsilon}\sum_{n=1}^{N}\sum_{m=1}^{4} Q_{nm}\left(\frac{\mathrm{K}(\pi/2,k_{nm})}{R_{nm}}\right), \quad (5)$$

where $\mathrm{K}(\pi/2,k)$ is the complete elliptic integral of the first kind of moduli:

$$k_{n1}^2 = \frac{4\,r\,r_n}{{R_{n1}}^2},\ k_{n2}^2 = \frac{4\,r\,r_n}{{R_{n2}}^2},$$

$$k_{n3}^2 = \frac{4\,r\,d_n}{{R_{n3}}^2},\ k_{n4}^2 = \frac{4\,r\,d_n}{{R_{n4}}^2},$$

where

$$R_{n1} = \sqrt{(r + r_n)^2 + (z - z_n)^2}$$
$$R_{n2} = \sqrt{(r + r_n)^2 + (z + z_n)^2}\ ,$$
$$R_{n3} = \sqrt{(r + d_n)^2 + (z - h_n)^2}\ ,$$
$$R_{n4} = \sqrt{(r + d_n)^2 + (z + h_n)^2}\ .$$

Q_{n1} and Q_{n2} are the charges of fictitious sources placed inside the prolate ellipsoidal electrode volume, for $z > 0$ and $z < 0$, respectively. Q_{n3} are the charges of ring electrodes of potential U and Q_{n4} are the charges of ring electrodes of potential $-U$. After matching the total potential to the value of zero at the ellipsoidal electrode surface and to the potential U at upper electrodes, i.e. to the value $-U$ at the lower electrodes, all the unknown charges can be determined.

B. Rings charges calculation of spherical electrode

We should now consider the system presented in Fig. 2 if *a*=*b*. In this case, the external body is modeled as a conducting sphere and placed into the central area. Using the method of images into the sphere mirror, this problem is observed in [7]. Dimensions of n-th degenerated primary cell of N-th order are h_n and d_n, and their images into the sphere mirror are $(a/R)^2 h_n$ and $(a/R)^2 d_n$, where $R = \sqrt{(h_n)^2 + (d_n)^2}$. If $Q_{n1} = Q_n$ are the charges of he toroidal electrodes of potential U, $Q_{n2} = -Q_n$ are the charges of the toroidal electrodes of potential $-U$, then $Q_{n3} = -Q_{n4} = -aQ_n / R$ are the charges of their images into the sphere mirror, respectively, for $n = 1, 2, ..., N$.

The potential, which produce charges on the toroidal electrodes and their images into the sphere mirror, can be calculated using (5), where

$$k_{n1}^2 = \frac{4 d_n r}{{R_{n1}}^2},\ k_{n2}^2 = \frac{4 d_n r}{{R_{n2}}^2},$$
$$k_{n3}^2 = \frac{4(a/R)^2 d_n r}{{R_{n3}}^2},\ k_{n4}^2 = \frac{4(a/R)^2 d_n r}{{R_{n4}}^2},$$

are moduli of complete elliptic integral of the first kind and:

$$R_{n1} = \sqrt{(r + d_n)^2 + (z - h_n)^2}\ ,$$
$$R_{n2} = \sqrt{(r + d_n)^2 + (z + h_n)^2}\ ,$$
$$R_{n3} = \sqrt{(r + (a/R)^2 d_n)^2 + (z - (a/R)^2 h_n)^2}\ ,$$
$$R_{n4} = \sqrt{(r + (a/R)^2 d_n)^2 + (z + (a/R)^2 h_n)^2}\ .$$

Using the condition that the toroidal electrodes are of equal potential U for $z > 0$, their unknown charges can be determined after matching the total potential to the potential U on them.

IV. NUMERICAL RESULTS

In accordance with the analysis presented above, a general numerical program has been developed using the software Mathematica 7.0 for different shapes of conducting bodies brought into the homogeneous electric field: prolate ellipsoid, oblate ellipsoid, and sphere conducting electrode. All these problem geometries are modeled using the software Femm [9] and the results are compared with analytical results.

A. Prolate ellipsoidal electrode

Let us observe a system consisting of a number of thin coaxial toroidal electrodes, which generate a homogeneous electric field, and prolate ellipsoidal electrode brought into the field. On the basis of a procedure presented in Section III A, numerical results for the prolate ellipsoidal electrode brought into the homogeneous electric field are obtained. A normalized value of the electric field strength along the z axis, for the case of an ellipsoidal body of normalized semi-axes $a/R = 0.4$ and $b/R = 0.2$, for primary cells of the first to fifth order is presented in Fig. 4.

It can be noticed that an excellent agreement of the results obtained using the analytical approach and the program FEMM is achieved. Equipotential lines for the same prolate ellipsoidal body and the number of primary cells $N = 1$ and $N = 3$ are presented in Figs. 5a and 5b, respectively. Only the region of $z > 0$ is shown as the electrical field symmetric.

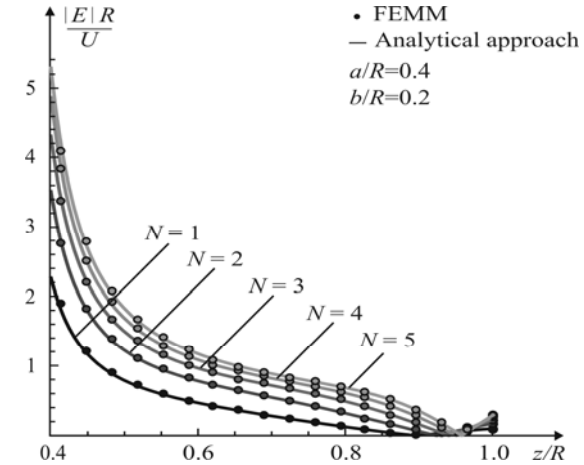

Fig. 4. Normalized electric field along z axis for different number of primary cells and ellipsoidal electrode of semi-axes $a/R = 0.4$ and $b/R = 0.2$.

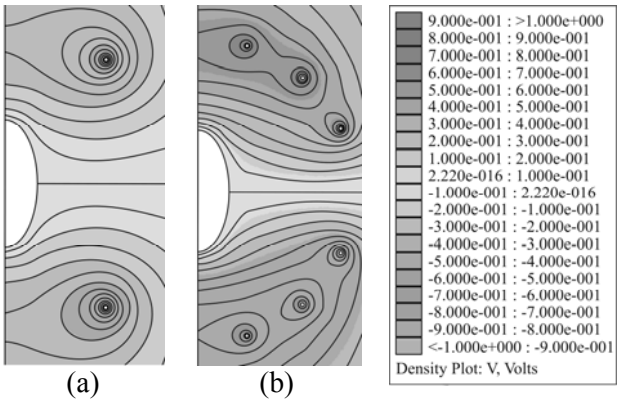

(a) (b)

Fig. 5. Equipotential lines for different number of primary cells, N, and ellipsoidal electrode of semi-axes $a/R = 0.4$, $b/R = 0.2$, $N = 1$ (a) and $a/R = 0.4$, $b/R = 0.2$ $N = 3$ (b).

B. Oblate ellipsoidal electrode

For the case of an oblate ellipsoidal electrode brought into the homogeneous electric field, of normalized semi-axes $a/R = 0.2$ and $b/R = 0.4$, normalized value of the electric field strength along z axis, $|E|R/U$, is presented in Fig. 6, for a different number of primary cells, from first to fifth.

Equipotential lines for the same ellipsoidal body and the number of primary cells $N = 1$ and $N = 3$ are presented in Figs. 7a and 7b, respectively.

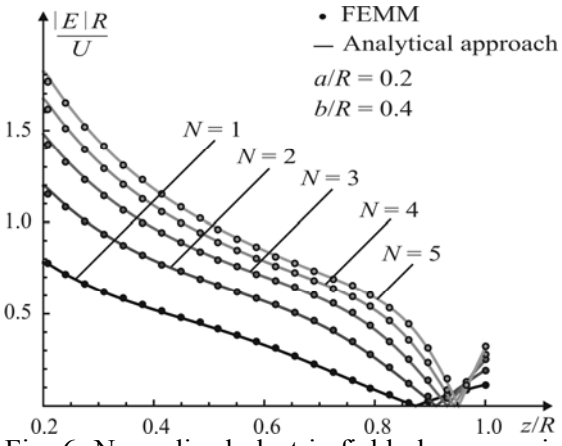

Fig. 6. Normalized electric field along z axis for different number of primary cells and ellipsoidal electrode of semi-axes $a/R = 0.2$ and $b/R = 0.4$.

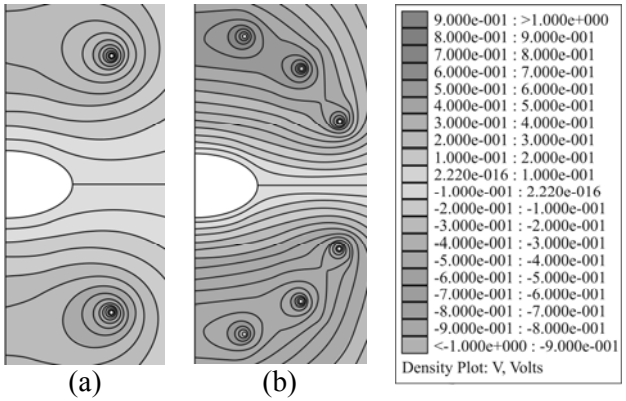

(a) (b)

Fig. 7. Equipotential lines for different number of primary cells, N, and ellipsoidal electrode of semi-axes $a/R = 0.2$, $b/R = 0.4$, $N = 1$ (a) and $a/R = 0.2$, $b/R = 0.4$, $N = 3$ (b).

C. Spherical electrode

On the basis of the procedure presented in Section III B, the problem of the spherical electrode brought into the homogeneous electric field of toroidal electrodes is investigated [7].

Let us observe firstly a system consisting of one primary cell. The normalized value of the electric field strength along z axis, with and without the external sphere conducting body of normalized radius $a/R = 0.1$, is presented in Fig. 8.

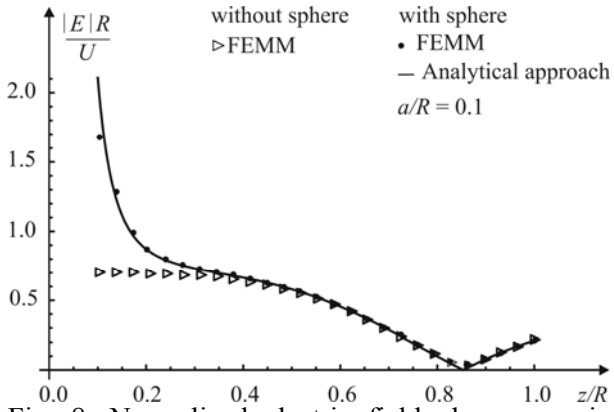

Fig. 8. Normalized electric field along z axis using one primary cell with and without external sphere of normalized radius $a/R = 0.1$.

Presented distributions show that an external conducting body influences on field distribution only in the close vicinity of the body brought into the homogeneous electric field.

The electric field distribution along the system axis for a different number of primary cells, by application of both Mathematica and Femm, is presented in Fig. 9. A high homogeneous electric field is attained using primary cells of high order.

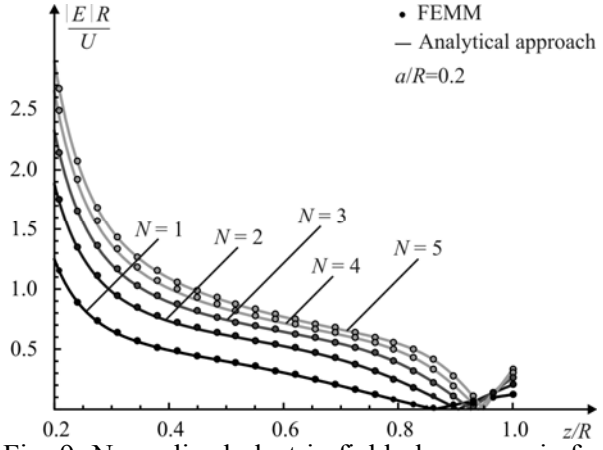

Fig. 9. Normalized electric field along z axis for different number of primary cells and $a/R = 0.2$.

The influence of the external body dimension on the achieved field homogeneity is shown in Fig. 10. An increase of sphere size disturbs realized field homogeneity.

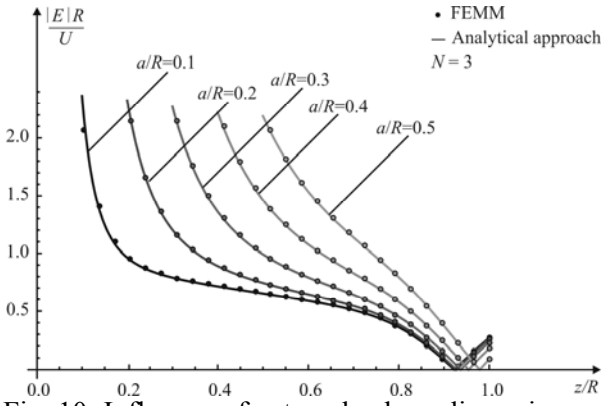

Fig. 10. Influence of external sphere dimension on realized field homogeneity using $N = 3$ primary cells.

Equipotential lines for $a/R = 0.2$, $N = 1$ and $a/R = 0.5$, $N = 3$, are shown in Figs. 11(a) and 11(b), respectively.

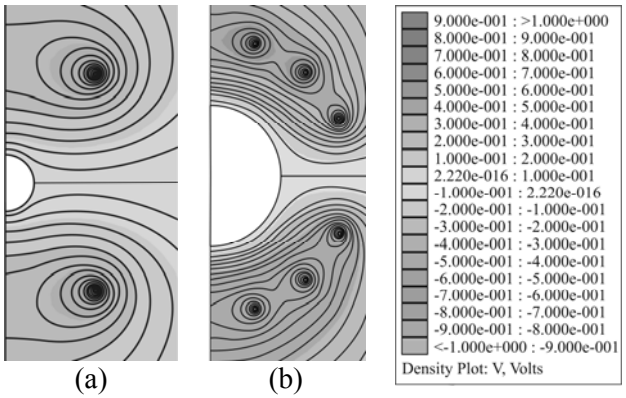

(a) (b)

Fig. 11. Equipotential lines for different number of primary cells, N, and spherical electrode of radius $a/R = 0.2$, $N = 1$ (a) and $a/R = 0.5$, $N = 3$ (b).

V. CONCLUSION

Complex toroidal electrostatic systems for the generation of homogeneous electrical fields and effects of different external conducting bodies on the achieved field homogeneity, are observed in this paper.

A potential along the system axis between two toroidal electrodes may be presented by a series in which all the coefficients are functions of an electrodes dimensions. With an appropriate choice of coil positions and dimensions, it is possible to eliminate as many as possible subsequent terms that differ from a linear one, which represent a

desired field. The homogeneity criterion is a number of series terms that vanish.

As the number of used electrodes increase, more members in the series vanish increasing the area of the homogeneous electric field. Keeping this in mind, a primary cell of the third order, $N = 3$, is recommended for a practical usage.

Based on the theoretical investigation, an affection of an external body, modeled as a spherical, prolate and oblate ellipsoidal electrode, is observed. External bodies are brought into the central region of the system of toroidal electrodes. The homogeneity is disturbed mostly in the close vicinity of the body.

More primary cells will provide a larger region of the homogeneous electrical field. Decrease of the external body influence on realized field homogeneity is accomplished by an increase of the primary cells number.

A dimension of an external conducting body has a strong influence on the achieved field homogeneity. The bigger the body, the smaller the area of the homogeneous electrical field.

The further investigation will apply to the system of biconical electrodes, which also can successfully be used for a generation of electrical fields of high homogeneity. Different shaped external bodies brought into the homogeneous electrical field will be investigated, too.

In addition to the need of making a space of the homogeneous electric field, very often there is a need for space in which there is no field. When such toroidal electrodes are grounded and placed in the external electric field, then they can be used for the space protection against the overflow electrical fields strengths.

ACKNOWLEDGEMENT

The authors want to thank Dr. Slavoljub Aleksic, full professor at the Faculty of Electronic Engineering of Nis, University of Nis, Serbia, for helpful discussions and comments. This research was partially supported by funding from the Serbian Ministry of Science (project No. 18019).

REFERENCES

[1] J. M. Jin, *Electromagnetic Analysis and Design in Magnetic Resonance Imaging*, CRC Press LLC, 1999.

[2] M. W. Garrett, "Axially Symmetric Systems for Generating and Measuring Magnetic Fields, Part I," *J. Appl. Phys.*, vol. 22, pp. 1091-1107, 1951.

[3] J. E. Everett and J. E. Osemeikhian, "Spherical Coils for Uniform Magnetic Fields," *J. Sci. Instrum.*, vol. 43, pp. 470-474, 1966.

[4] J. A. Jungerman, "Fourth-order Uniform Electric Field from Two Charged Rings," *Rev. Sci. Instrum.*, pp. 1479-1482, 1984.

[5] C. E. Baum, "Production of Uniform Electrostatic Fields by a Slotted Conducting Spherical Shell," *IEEE Trans. Mag*., vol. 30, no. 1, pp. 9-12, 1988.

[6] D. M. Velickovic and Z. Z. Cvetkovic, "Systems for Generating of Homogeneous Electrical Field," *Facta Universitatis, series Electronics and Energetic*, vol. 14, no. 1, pp. 91-108, 2001.

[7] Z. Cvetkovic, M. Peric, and B. Petkovic, "The Influence of Conducting Body on Electric Field Homogeneity," *54th International Scientific Colloquium - IWK 2009*, Ilmenau, Germany, pp. 113-114, Sept. 2009.

[8] H. Singer, H. Steinbigler, and P. Weiss, "A Charge Simulation Method for the Calculation of High Voltage Fields," *IEEE Trans. PAS-73*, pp. 1660-1668, 1974.

[9] femm 4.2 (Finite Element Method Magnetics) (2008) http://femm.berlios.de

Zlata Z. Cvetkovic was born in Blace, Serbia. She received the M.Sc. degree in 1991 and Ph.D. degree in 2002 from the University of Nis.

From June 1980 until May 1990, she had been working in the "Electronic Industry" in Nis, as an engineer. From May 1990 until today, she has been working at the Department of Theoretical Electrical Engineering at the Faculty of Electronic Engineering in Nis. Since 2007, she has been working as an Associate Professor.

Her researching areas are: analysis of the nonuniform transmission lines, analytical, and numerical methods for electromagnetic field modeling.

Bojana R. Petkovic was born in Nis, Serbia. She received Dipl. Ing. and Master degree from the Faculty of Electronic Engineering (FEE), University of Nis, Serbia, in 2002 and 2008, respectively.

From 2002 to 2009, she was working as a researching-teaching assistant at the Department of Theoretical Electrical Engineering at the FEE in Nis.

From 2010, she is a Ph.D. student in the International Graduate School Lorentz Force at the Ilmenau University of Technology, Germany. She is working on a project Optimization of sensor arrangements during image-guided Lorentz force eddy current testing.

Mirjana Peric was born in Nis, Serbia. In 2006, she received M.Sc. degree from the Faculty of Electronic Engineering (FEE), University of Nis, in Theoretical Electrical Engineering major.

Since 2001, she has been working as a teaching assistant at the Dept. of Theoretical El. Engineering at the FEE.

Her researching areas are: EM field theory, analytical and numerical methods for electromagnetic field modeling, EM field modeling in the vicinity of power lines, and software application in electromagnetics.

Extension of Compact TLM Air-Vent Model on Rectangular and Hexagonal Apertures

Nebojsa Doncov, Bratislav Milovanovic, and Zoran Stankovic

Faculty of Electronic Engineering
University of Niš, Aleksandra Medvedeva 14, 18000 Niš, Serbia
nebojsa.doncov@elfak.ni.ac.rs, bata@elfak.ni.ac.rs, zoran.stankovic@elfak.ni.ac.rs

***Abstract*—** Compact transmission line matrix (TLM) air-vent model extension, to allow for a computationally efficient modelling of airflow arrays with rectangular or hexagonal apertures, even in the case of significant thickness of a supporting metal panel, is presented. An empirically derived model is introduced as an equivalent circuit into an otherwise coarse TLM mesh to account for the electromagnetic (EM) presence of apertures. The model accuracy and efficiency are validated on several characteristic electromagnetic compatibility (EMC) examples.

***Index Terms* —** Empirical air-vent model, rectangular and hexagonal apertures, TLM method.

I. INTRODUCTION

Differential numerical techniques, such as the finite-difference time-domain (FD-TD) [1] and the transmission line matrix (TLM) [2], are common tools for computational analysis of numerous electromagnetic (EM) and electromagnetic compatibility (EMC) problems. However, when attempting to apply these methods, working usually in the time-domain, to describe complex practical systems, treatment of geometrically small but electrically important features, often found on these systems, presents a challenging and time-consuming task. A conventional solution of employing a very fine mesh to model these features in an otherwise large modelling space leads in some cases to a prohibitively large number of nodes and time steps. Therefore, enhancements to these techniques are required to allow for an efficient simulation of realistic multi-scale EM and EMC problems.

For some of the fine features, such as wires and slots, few enhancements to the FD-TD method [3, 4] and the TLM method [5-7] have been developed in the past. As far as the TLM method is concerned, these so-called compact models have been implemented in the form of an additional one-dimensional transmission line network running through a tube of regular nodes, allowing accounting for the EM presence of wires and slots without applying a very fine mesh around them. Compared with the conventional approach, these models yield a dramatic improvement in the computer resources required. A different type of solution has been presented in [8] in the form of several modified TLM nodes developed to accurately model the fast variation of the EM field around sharp conducting regions by coarse mesh.

Airflow aperture arrays or air-vents, often found on equipment enclosures for ventilation purposes, fall into the category of fine features. Their presence can significantly increase emission and decrease shielding effectiveness of the box [9]. Again, if conventional FD-TD and TLM as effective volume-based methods are used without any enhancement (e.g. compact model or modified node), an extremely fine mesh is required to accurately capture the strong variation of the EM field across each aperture dimension and depth of the supporting panel. Therefore, it has a cost that prediction of enclosure performances at the design stage, due to presence of air-vents, can be computationally very expensive [10].

In recent years, enhancements of the TLM method, based on **Z**-transform approach, have been done and applied, among other things, to model air-vents [11]. In parallel with this approach, a simple compact model solution of air-vent for square and circular apertures has been

developed and presented in [10]. This efficient solution, developed especially for air-vents, is easy for implementation and it does not require a modification of standard TLM symmetrical condensed node (SCN) and its scattering procedure. It was based on the insertion of equivalent circuit with an empirically found inductive element into an otherwise course mesh. The equivalent circuit model is often used for EM and EMC analyses, but in [10] it was implemented into the time-domain solver. Both approaches take into account the EM presence of air-vents using computational cells larger than the individual apertures and achieving significant savings in memory and run-time in comparison with the conventional TLM approach. In addition, the approach in [10] has been enhanced to allow modelling of square and circular air-vents for significant perforation depth and at higher frequencies, verified only on one artificial example of plane wave propagation through circular aperture array in a thick metal panel [12].

In this paper, the approach described in [12] is extended on air-vents with rectangular and hexagonal apertures, found on equipment boxes as often as square or circular apertures. The real usefulness of being able to model, for an example, rectangular perforations comes from the case of simulating a box full of complicated equipment. In that case, it is unknown what the dominant polarization will be; the polarization is off-axis or is different at different parts of the vent. Thus, this model will produce much more accurate results than the compact square air-vent model used sometimes to approximately describe an array of rectangular apertures. The modelling of air-vents with rectangular and hexagonal apertures is described in details in the paper.

All the models are incorporated into a three-dimensional (3D) SCN TLM mesh and implemented in 3D TLM*scn* solver, designed at the Microwave Lab at the Faculty of Electronic Engineering in Nis, Serbia. This TLM solver has been already successfully applied to many EM problems such as resonant cavity-based microwave applicators [13]. The ability of the presented models to accurately account for the EM presence of apertures, even in the case of significant perforation depth, and their run-time and memory efficiencies are successfully validated in several characteristic EMC environments. Obtained results of simulated transmission through an imperfectly shielded test enclosure with different air-vents are compared with the experimental and fine TLM SCN mesh results.

II. MODEL DESCRIPTION

Perforations on thin metal screens, for a normally incident plane wave excitation, can be treated as an inductive short on the TLM link lines used to represent a thin panel. This inductive susceptance is the simplest possible arrangement acting as a perfect short at DC and allowing transmission at higher frequencies [9]. In addition, a perforation on a metal screen may be regarded as an extremely short, highly cut-off waveguide, while in a lumped component model of such a waveguide, only shunt inductance would be significant. Therefore, current flowing down the edges of apertures on a thin metal panel can be successfully represented by this shunt inductance. However, at higher frequencies, there is a requirement to accurately capture an EM field distribution inside the aperture itself, especially if there is a significant perforation depth. An equivalent circuit containing an additional capacitive element connected in shunt with an inductive short is capable to model very deep apertures while allowing easy TLM implementation (Fig.1).

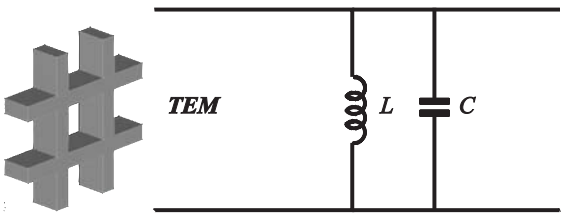

Fig. 1. Compact air-vent model based on *LC* network.

For a TEM line of characteristic impedance Z_0 with a shunt reactance X inserted at its midpoint, $X = \omega L_e$ where L_e is an equivalent inductance expressed as $L/(1- \omega^2 LC)$, the transmission coefficient is:

$$T = jX / (jX + Z_0 / 2), \qquad (1)$$

or for low frequency approximately proportional to the reactance X. It is reasonable to expect that the break frequency $f_{break}=(Z_0/2)/(2\pi L_e)$ would correspond to the cut-off frequency of the perforation and that the transmission would reduce

in proportion to the decreasing of a fractional area of the panel occupied by the perforations and increasing of panel thickness. This reduction in transmission of a perforated metal panel, being achieved by proportional reductions in L_e, obviously depends on the actual geometry of the perforations.

In order to empirically determine effective reactive parameters of a perforated panel containing rectangular or hexagonal apertures, the numerical procedure similar to the one in [12] is used. The conventional TLM method with a very fine computational mesh is applied to find the transmission coefficient of a perforated panel for a normally incident plane wave. However, in the case of rectangular apertures, as explained previously, this should be done separately for horizontal and vertical polarization. Symmetry conditions were exploited to model only one period of the perforation. The results for output of the far side of the panel, obtained for different dimensions of perforations and for different panel thicknesses (up to cross-sectional dimensions of the apertures) indicate that transmission increases slightly more than proportionally to the fractional coverage of the panel by the apertures. At the same time, transmission decreases almost exponentially with increasing the perforation depth. This can be seen from Fig. 2 and Fig. 3, taken at frequency $f = 0.2\, f_c$ where f_c is the cut-off frequency of the considered perforation.

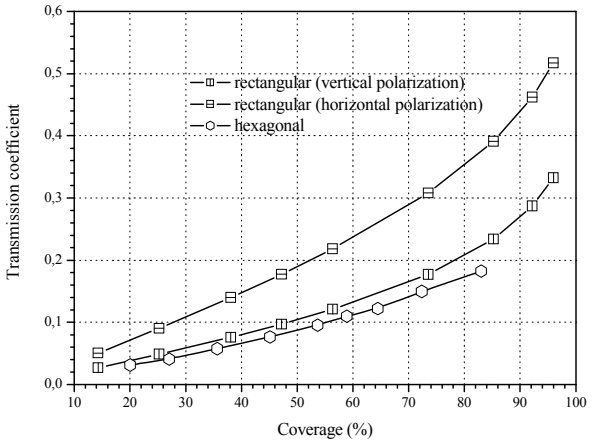

Fig. 2. Transmission versus coverage for rectangular (vertical and horizontal polarization) and hexagonal aperture.

In addition, the results for the transmission coefficient of a panel with hexagonal apertures show that this aperture can be successfully approximated with a circular aperture of equivalent radius r_e, obtained from the condition of the same coverage (Fig. 4):

$$\frac{r_e^2\pi}{p^2} = \frac{6\, l_{hex}^2 \sqrt{3}/4}{p^2} \Rightarrow r_e = l_{hex}\sqrt{\frac{3\sqrt{3}}{2\pi}}, \quad (2)$$

where: l_{hex} is an edge length of regular hexagonal aperture. In order to illustrate this, transmission coefficient, obtained for a perforated plate containing either hexagonal apertures with edge length of 1 mm or circular apertures with equivalent radius of 0.909 mm, is shown in Fig. 5. The thickness of a supporting metal panel was 10% of the edge length and total coverage was 53.679 %.

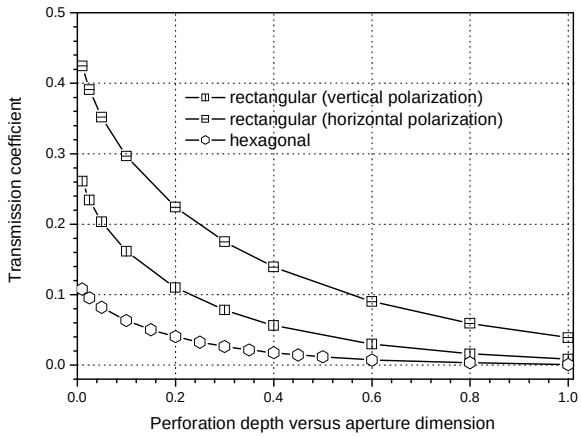

Fig. 3. Transmission versus perforation depth for rectangular (vertical and horizontal polarization) and hexagonal aperture.

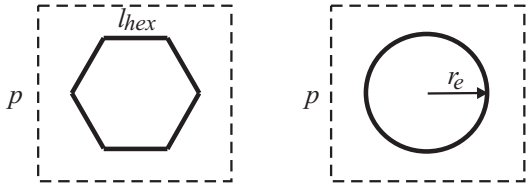

Fig. 4. a) Regular hexagonal aperture and b) its equivalent circular aperture.

Based on these results and using Eq. (1), the equivalent inductance L_e was calculated at two frequencies f_1 and f_2 chosen to bracket most of the band below perforation cut-off (e.g. $f_1 = 0.1\, f_c$ and

f_2=0.8 f_c). Then, the equivalent inductance of the panel was approximated as a product of several factors that include the shape, depth, and cut-off frequency of the perforation and the panel coverage:

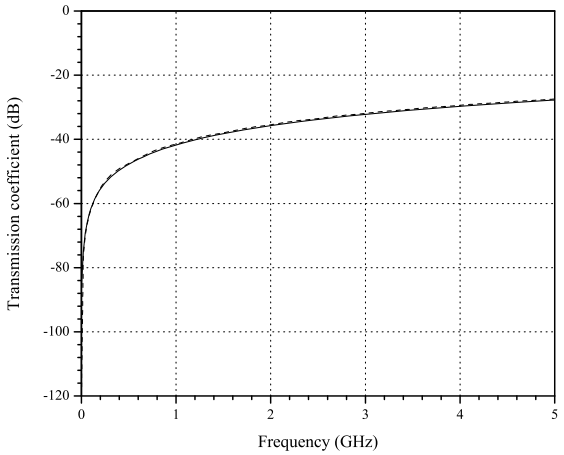

Fig. 5. Transmission coefficient of a perforated metal plate containing either hexagonal apertures of edge length l_{hex} (solid line) or circular apertures of equivalent radius r_e (dash line).

$$L_e = \text{form\_factor} * L\_\text{cutoff} * \text{coverage\_factor} * \text{depth\_factor} = A_0 * \left(\frac{Z_0/2}{2\pi f_c}\right) * \left(\sum_{i=1}^{3} A_i \text{cov}^i\right) * \text{Exp}\left(-A_4 \frac{t}{v/(2\pi f_c)}\right), \quad (3)$$

where: *cov* is the fractional area of the metal panel cut away; t is perforation depth and v is speed of light. Constants A_0, A_1, A_2, A_3, and A_4 are given in Table 1 for rectangular and hexagonal aperture shapes and for horizontal (H) and vertical (V) polarization. The previously empirically found coefficients for square and circular apertures are shown on the same table. Hexagonal and circular apertures have the same coefficients, but the value of equivalent inductance, obtained from Eq. (3), is different for these shapes due to different cut-off frequencies.

It should be said that the application of the proposed models for rectangular and hexagonal aperture shape is restricted to the range of aperture parameters that fulfill the conditions already mentioned in [12].

Table 1: Constants used in L_e approximation

	Aperture shape	A_0	A_1	A_2	A_3	A_4
L_e (f_1)	circular and hexagonal (H and V)	1.433	1.0	0.472	0	1.052
	square (H and V)	1.491	1.0	0.472	0	1.080
	rectangular (V)	4.692	0.523	-0.861	1	0.917
	rectangular (H)	4.697	0.593	-0.807	1	0.853
L_e (f_2)	circular and hexagonal (H and V)	1.741	1.946	-0.75	0	0.673
	square (H and V)	1.574	1.525	0.264	0	0.728
	rectangular (V)	5.694	0.6	-1.050	1	1.044
	rectangular (H)	8.385	0.718	-1.294	1	1.163

The model is implemented in a way that effective inductance and capacitance of the panel, L and C, are chosen so that their reactance in parallel is $2\pi fL_e$ at frequencies f_1 and f_2. For each polarization, they are implemented in traditional TLM mesh using additional short- and open-circuit stub lines, at the interface between two nodes (Fig. 6a). The scattering procedure for the aperture array can be then easily derived applying the Thevenin equivalent circuit (Fig. 6b).

Since, in general, apertures extend in two different directions, voltage pulses from both orthogonally polarized TLM link lines are coupling with the aperture. The total voltage at the interface, for a particular polarization, is:

$$V_{total} = 2\frac{V_l^i Y_l + V_r^i Y_r + V_s^i Y_s + V_o^i Y_o}{Y_l + Y_r + Y_s + Y_o}, \quad (4)$$

where: V_l^i and V_r^i are incident voltage pulses from the link lines of characteristic admittances Y_l

and Y_r, coupling with the aperture and V_s^i and V_o^i are incident voltage pulses on short and open stub lines of characteristic admittances Y_S and Y_O, respectively. Reflected voltage pulses are then:

$$\begin{aligned} V_l^r &= V_{total} - V_l^i; \quad V_r^r = V_{total} - V_r^i \\ V_s^r &= -V_{total} + V_s^i; \quad V_o^r = V_{total} - V_o^i \end{aligned} \tag{5}$$

III. NUMERICAL RESULTS

First, capability of the previously developed compact TLM air-vent model for square apertures to model perforated metal screen with significant thickness is illustrated in the characteristic EMC environment (rectangular test enclosure depicted in Fig. 7). The inside dimensions of the enclosure are: *a*=50 cm, *b*=20 cm, and *c*=40 cm. A thin (*t*=0 cm) or thick (*t*=1 cm) aluminium plate was used for the front face containing the array of square apertures, while five other enclosure pieces were with thickness 0.635 cm. The square aperture size was *l*=1 cm, with an edge-to-edge space of 0.5 cm. The number of apertures was 252. The model was excited by a long-wire feed at the back of the box which was modelled by a simple voltage source V=1 mV with 50 Ohm resistance incorporated into a single node at the feed point. The excitation had the centre conductor of the probe extended to span the width of the cavity with a 0.16 cm diameter wire, modelled using wire node [5], and terminated on the opposite cavity wall with termination of 47 Ohm. Choice of geometry, lossy material of thickness *d*=1 cm, excitation, and output was governed by experimental arrangements [14].

The compact model for square perforations was incorporated into a coarse TLM mesh (21*10*20 nodes used for enclosure modelling where Δy=Δz=2 cm, Δx=1 cm for lossy material, and 2.45 cm elsewhere). The same mesh size was used either for thin or thick front face as thickness of front wall was specified in the compact model. TLM simulation was performed, as for all other EMC examples considered in this section, on Intel Core 2 Duo PC machine with 2.66 GHz clock rate, 2 GB RAM, and 32-bits Windows XP OS. Numerical results for the electric field at point 3 m away from the box, for zero-thin and thick front face, have been compared to the experimental results given in [14] and an excellent agreement (Fig. 8) has been observed except at higher frequencies, probably due to neglecting the frequency dependant characteristics of the lossy material at the back of the box.

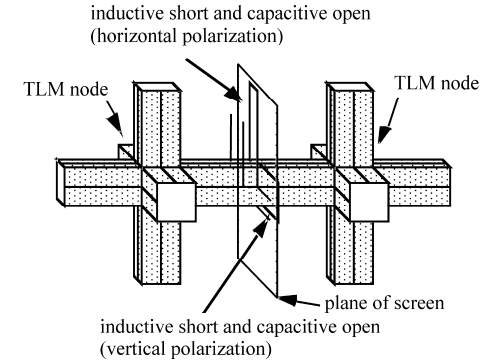

a)

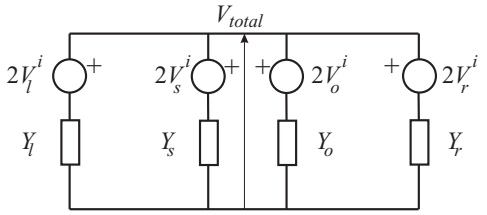

b)

Fig. 6. a) *LC* model at the interface between two TLM nodes, b) Thevenin equivalent circuit for a particular polarization.

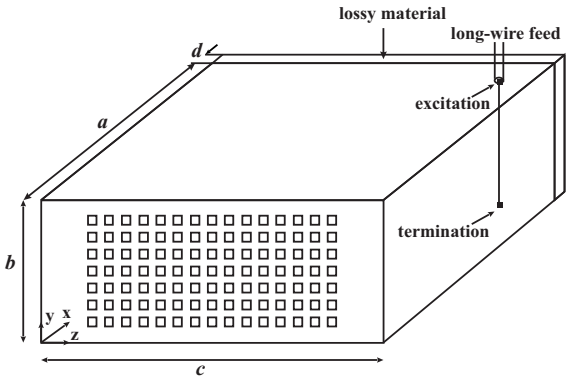

Fig. 7. Imperfectly shielded test enclosure with an array of square apertures on front face.

In reference [14], additional compensation factors, due to the insufficient number of nodes to describe the aperture, were found and applied to correct FD-TD numerical results. As compact TLM air-vent model allows for inherent modelling of the aperture shape and depth, much coarser mesh was used but no additional factors are required. Therefore, savings of two orders of magnitude in memory and run-time are achieved,

compared to the traditional fine mesh FD-TD simulation. It should be said that in the case of thick front face, where perforation depth was equal to square aperture size (t=l), experimental results were scaled according to formula $16\sqrt{\pi}(t/l)$ given in [14].

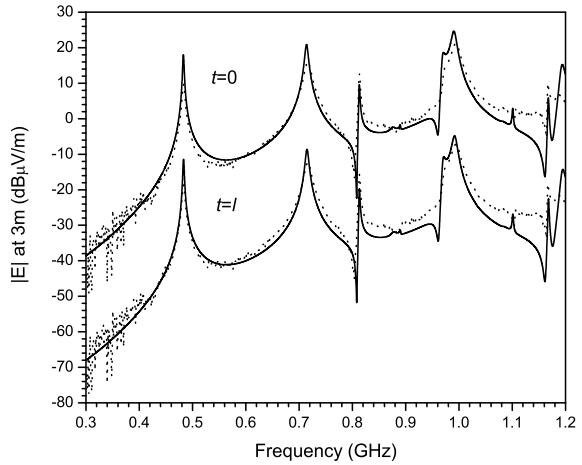

Fig. 8. Radiated electric field at 3m away from enclosure (solid line: compact air-vent model, dot line: measurements).

The developed compact TLM air-vent model for rectangular perforations has been verified simulating transmission out of an imperfectly shielded rectangular test enclosure. The dimensions of the box were: a=100 mm, b=80 mm, and c=15 mm (Fig. 9). A t=0.2 mm thin aluminium plate was used on two opposite faces of the box as a supporting panel for the array of rectangular apertures. The dimensions of rectangular perforation were 7.2 mm in x- and 4 mm in z-direction. Edge-to-edge aperture spacing was 1.8 mm in x- and 1 mm in z-direction. The number of apertures for each array was 33 giving a total coverage of 63.36%. The box was excited by a straight wire placed inside the box (position 1).

The compact model was applied on a relatively course mesh (61*44*10 nodes used for enclosure modelling where Δx=1.639 mm, Δy=1.818 mm, and Δz=1.5 mm). The total run-time was 1.5 min, while allocated memory was 33 Mb (see Table 2). Then, a fine mesh of 112*49*16 is applied to model enclosure with these airflow arrays using only conventional TLM routines. In order to model geometry of the apertures and accurately describe EM field distribution inside and around the apertures, 8 uniform grid lines

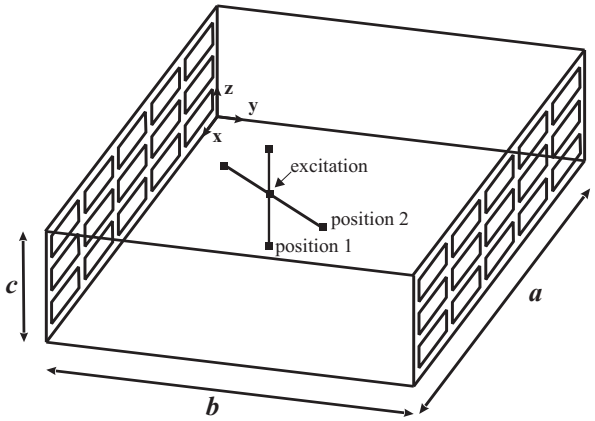

Fig. 9. Imperfectly shielded test enclosure with array of rectangular apertures on opposite faces.

along the bigger (Δx=0.9 mm), and 4 uniform grid lines along the smaller dimension of rectangular apertures (Δz=1 mm) were used to describe their cross-section. The same grid resolution in each direction was used to describe edge-to-edge spacing. Spacing from the first and last aperture to enclosure edges were represented by two nodes of 0.7 mm in x- and one node of 0.5 mm in z-direction. Perforation depth of 0.2 mm was represented by one node. As it can be seen from Table 2, the total run time was 60 min on the same PC machine with more than two times memory resources allocation than the compact model. Electric field in front of one airflow array, obtained by these two simulations is shown in Fig. 10.

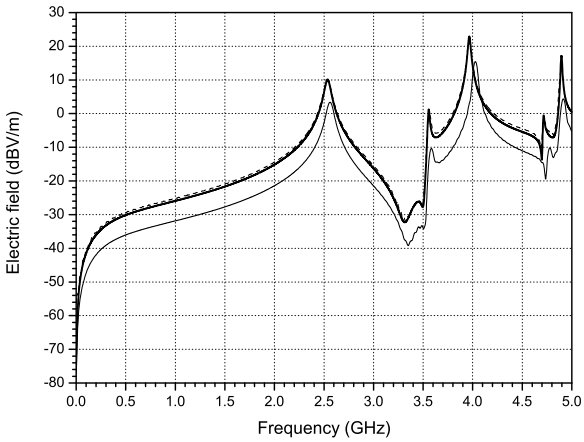

Fig. 10. Electric field in front of thin rectangular airflow array (bold solid line: compact air-vent rectangular model, thin solid line: compact air-vent square model, dash line: fine mesh).

Excellent agreement between the compact air-vent model and fine mesh results can be observed.

The result for electric field obtained by the compact square air-vent model and the same mesh size of 61*44*10 nodes for enclosure modelling is shown on the same figure. The number (60) and dimension of square apertures (4 mm) were defined in the compact model to represent the same coverage of imperfectly shielded faces as in the case of rectangular apertures. As it can be seen, these results are significantly below the fine mesh results. How for this particular case, electric field has a dominant z component, the compact square air-vent model might produce better results if we chose the dimension of square aperture equal to the bigger dimension of rectangular aperture. However, in many practical cases a box is full of complicated equipment and the dominant polarization of the EM wave at air-vents is often unknown. Also, the wave polarization might be off-axis or different at different parts of the airflow array. Thus, in cases when rectangular perforations are used for ventilation, the usefulness of being able to model them exactly is clearly obvious.

Table 2: Simulation cost of compact air vent model and fine-mesh TLM model generating numerical results shown in Figs. 10, 11, and 13

	Simulation cost	Fig.10	Fig.11	Fig.13
Compact model	run-time	1.5 min	2 min	20 sec
	allocated memory	33 Mb	35 Mb	6 Mb
Fine mesh	run-time	60 min	94 min	22 min (fm 1)
				220 min (fm 2)
	allocated memory	68 Mb	132 Mb	41 Mb (fm 1)
				154 Mb (fm 2)

To illustrate capability of describing perforations on a very thick supporting metal panel, the test enclosure from Fig. 9 was considered, but dimensions of each of the 16 rectangular perforations were 10.85 mm in x- and 5.08 mm in the z-direction with edge-to-edge spacing of 0.69 mm. Perforation depth of both air-vents was 5.2 mm. Wire feed was placed diagonally inside the box (position 2). In a fine TLM mesh with 156*49*24 nodes for enclosure modelling, 16 and 7 uniform grid lines along the bigger (Δx=0.678 mm) and along the smaller dimension of apertures (Δz=0.726 mm), respectively, were used to describe their cross-section. To capture EM field distribution inside the perforation more accurately, 26 uniform grid lines (Δx=0.2 mm) in y-direction were applied. A compact air-vent model was applied on a coarse TLM mesh of 51*41*15 nodes (Δx=1.96 mm, Δy=1.95 mm, and Δz=1 mm; mesh is slightly different than the coarse mesh for Fig. 9 due to modelling of a diagonal wire). Run-time and allocated memory for both meshes are shown in Table 2. The comparison of the results for the electric field in front of air-vents is presented in Fig. 11.

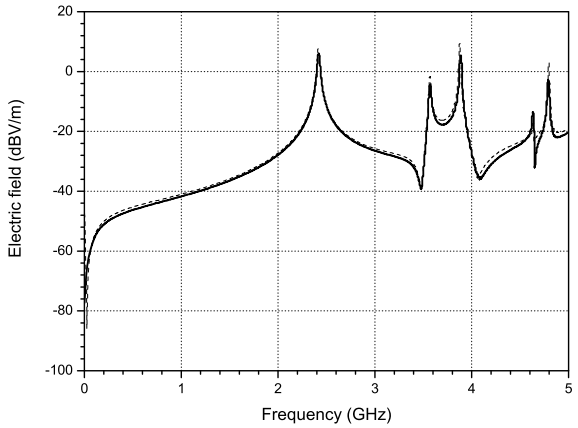

Fig. 11. Electric field in front of thick rectangular airflow array (solid line: compact air-vent rectangular model, dash line: fine mesh).

The calculation of shielding effectiveness (SE), for an aluminium enclosure with an array of hexagonal apertures covering one part of front face (Fig. 12, $a \times b \times c$=295×120×295 mm, $b_1 \times c_1$=60×190 mm), was used to verify a compact air-vent model for hexagonal apertures. The incident plane wave had an electric field polarised in y-direction. The edge length of hexagonal perforation was 6.6 mm and the number of

apertures was 20 giving a 20% total coverage of front face perforated area.

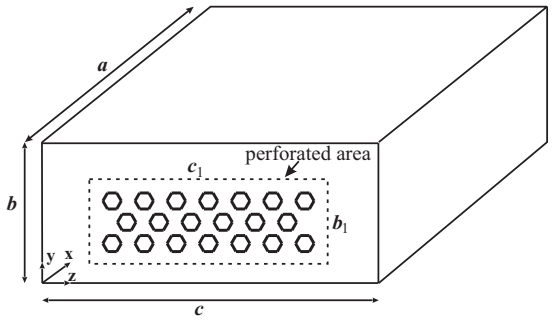

Fig. 12. Imperfectly shielded test enclosure with array of hexagonal apertures partially covering front face.

Two TLM fine meshes: fm 1 with 30*48*144 nodes and fm 2 with 39*94*244 nodes were used for enclosure modelling. Number of nodes used for each aperture cross-section dimension was 10 (fm 1) and 16 (fm 2). Also, a few more nodes in fm 2 are added in the x-direction (Δx=1.2 mm) around front face in order to more accurately account for plane wave coupling with aperture array. The compact model simulation used coarse mesh of 11*10*17 nodes to produce the similar results for SE up to 1 GHz (Fig. 13), either for front face with zero thickness (t=0 mm) or with thickness t=6 mm (described by 5 nodes in fm 2). Savings in memory and run-time, achieved by the compact model, in comparison with fine meshes for the case t=0 mm are shown in Table 2.

IV. CONCLUSION

This paper described an extension of the TLM method to allow for efficient computer modelling of EM field propagation through array of rectangular or hexagonal apertures in metal equipment boxes. It is based on insertion of equivalent circuit into otherwise coarse mesh, an approach that was often used in the area of computational electromagnetics to produce simple but accurate solutions to many EM problems. Here, this approach with empirically found elements of lumped circuit for some typical aperture shapes is applied to account for the strong variation of EM fields inside and around the apertures even in the case of significant depth of the supporting panel. Presented examples verify the efficiency of the developed equivalent circuit model with accuracy acceptable for most EMC applications. In addition, its implementation in comparison with other existing approaches requires very little modification of the existing traditional TLM code. The considered apertures are with regular shapes but it is clear that irregular apertures can be treated in a similar way with the same or more complicated circuits as well as long as the transmission coefficients are numerically available.

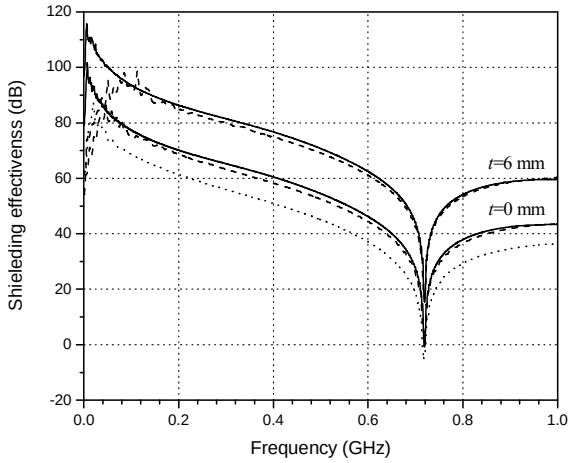

Fig. 13. SE of a metal enclosure in Fig. 12 (solid line: compact air-vent hexagonal model, dot line: fm 1, dash line: fm 2).

ACKNOWLEDGMENT

This work has been supported by the Serbian Ministry of Science under the project TR-32052.

REFERENCES

[1] K. S. Kunz and R. J. Luebbers, *The Finite Difference Time Domain Method for Electromagnetics*, CRC Press, Boca Raton, FL, 1993.

[2] C. Christopoulos, *The Transmission-Line Modelling (TLM) Method*, IEEE/OUP Series, Piscataway, NJ, 1995.

[3] F. Edelvik, "A New Technique for Accurate and Stable Modeling of Arbitrarily Oriented Thin Wires in the FDTD Method," *IEEE Trans. Electromagn. Compat.*, vol. 45, no. 2, pp. 416-423, 2003.

[4] F. Edelvik and T. Weiland, "Stable Modelling of Arbitrary Oriented Thin Slots in the FDTD

Method," *IEEE Trans. Electromagn. Compat.*, vol. 47, no. 3, pp. 440-446, 2005.

[5] A. J. Wlodarczyk, V. Trenkic, R. Scaramuzza, and C. Christopoulos, "A Fully Integrated Multiconductor Model for TLM," *IEEE Trans. Microwave Theory Tech.*, vol. 46, no. 12 pp. 2431-2437, 1998.

[6] J. Paul, C. Christopoulos, D. W. P. Thomas, and X. Liu, "Time-Domain Modeling of Electromagnetic Wave Interaction with Thin-Wires using TLM," *IEEE Trans. Electromagn. Compat.*, vol. 47, no. 3, pp. 447-455, 2005.

[7] V. Trenkic and R. Scaramuzza, "Modelling of Arbitrary Slot Structures using Transmission Line Matrix (TLM) Method," *Int. Symp. Electromagn. Compat.*, Zurich, Switzerland, pp. 393-396, 2001.

[8] J. A. Morente, J. A. Porti, H. Magan, and O. Torres, "Improved Modeling of Sharp Zones in Resonant Problems with the TLM Method," *Applied Computational Electromagnetic Society (ACES) Journal*, vol. 14, no. 2, pp. 67-71, 1999.

[9] T. Y. Otoshi, "A Study of Microwave Leakage through Perforated Flat Plates," *IEEE Trans. Microwave Theory Tech.*, vol. 20, no. 3, pp. 235-236, 1972.

[10] N. Doncov, A. J. Wlodarczyk, R. Scaramuzza, and V. Trenkic, "TLM Modelling of Perforated Metal Screens," *4th Int. Conf. Computational Electromagnetics*, Bournemouth, UK, 2002.

[11] J. Paul, V. Podlozny, and C. Christopoulos, "The Use of Digital Filtering Techniques for the Simulation of Fine Features in EMC Problems Solved in the Time Domain," *IEEE Trans. Electromagn. Compat.*, vol. 45, no. 2, pp. 238-244, 2003.

[12] N. Doncov, A. J. Wlodarczyk, R. Scaramuzza, and V. Trenkic, "Compact TLM Model of Air-Vents," *Electronics Letters*, vol. 38, no. 16, pp. 887-888, 2002.

[13] J. Jokovic, B. Milovanovic, and N. Doncov, "Numerical Model of Transmission Procedure in a Cylindrical Metallic Cavity Compared with Measured Results," *Int. Journal of RF and Microwave Computer-Aided Engineering*, vol. 18, no. 4, pp. 295-302, 2008.

[14] M. Li, J. Nuebel, J. L. Drewniak, R. E. DuBroff, T. H. Hubing, and T. P. Van Doren, "EMI from Airflow Aperture Arrays in Shielding Enclosures – Experiments, FDTD, and MoM Modelling," *IEEE Trans. Electromagn. Compat.*, vol. 42, no. 3, pp. 265-275, 2000.

Wideband Compact Antenna with Partially Radiating Coplanar Ground Plane

Ahmed Toaha Mobashsher[1], Mohammad Tariqul Islam[1], and Norbahiah Misran[2]

[1] Institute of Space Science (ANGKASA)
Universiti Kebangsaan Malaysia, Bangi, Selangor, Malaysia
i_toaha@yahoo.com, tariqul@ukm.my

[2] Dept. of Electrical, Electronic, and Systems Engineering
Universiti Kebangsaan Malaysia, Bangi, Selangor, Malaysia
bahiah@vlsi.eng.ukm.my

Abstract ─ Many of today's portable communication applications require antennas that are compact, broadband, and easily integrable in a big variety of terminal geometries. This paper presents a compact wideband antenna with partially radiating coplanar ground plane. The prototype of the antenna shows a wide bandwidth (VSWR ≤ 2) of 92% (from 3.53GHz to 9.5GHz). The antenna also exhibits maximum gain of 3.5*dBi* and stable radiation patterns over the whole bandwidth. Nevertheless, in this paper the significance of the ground planes on the operating bandwidth are examined with the help of current distribution and discussed in detail with supporting parametric analysis.

Index Terms ─ Coplanar waveguide feeding, radiating ground plane, wideband antenna.

I. INTRODUCTION

Over the past decade, extensive research on broadband antennas, with low-profile, lightweight, flush mounted, and single-feed to fit the limited equipment space of the portable wireless devices, has contributed to the development of modern communication technology [1]. Wideband antennas play a key role in the faithful operation of these evolving high data rate transceivers. While the bandwidth of antennas is desired to be increased drastically, the size has to be decreased correspondingly due to the demands of portable devices. Nevertheless, polarization, radiation patterns and gains are also important factors in the application of antennas in contemporary and future broadband wireless communication systems.

In order to recover these obstructions, development, and application of cutting-edge technologies are needed that can facilitate compact broadband antennas that can be manufactured and integrated into the portable devices to provide highly survivable, yet lightweight and reliable systems. Because of the attractive features of thickness, weight, efficiency, conformability and simplicity of manufacture, microstrip antennas are widely implemented in many applications, especially in wireless communication. However, narrow bandwidth is the main limitation that restricts the scope of microstrip patch antenna technology.

The new co planar waveguide structure, used for printed antennas to attain wide bandwidth has recently attracted huge attention. Numerous advantages have been obtained by feeding a radiating element with coplanar waveguide (CPW) feeds. When compared with other printed radiating elements, CPW-fed antennas possess advantages of not only a broad bandwidth, but also a smaller mutual coupling between adjacent lines [2]. Another advantage of coplanar fed antenna is lower radiation leakage and less dispersion than microstrip lines. Moreover, this feed design eliminates the competition for surface space between the antenna elements and the feed network. Owing to the uniplanar design, with coplanar waveguide the integration capability with

solid-state active and passive components is easier, since these components can be fabricated on one side of the planar substrate, eliminating the need for via hole connections. In response to the increasing demand for compact, broadband, and easily fabricated antennas for use in various wireless communication systems, several CPW-fed printed antennas have been developed over the past decade [3–9]. However, these antennas either have inconvenient shape or difficult to fabricate, which demands miniaturized simple antennas.

In this paper, a simple and compact antenna is introduced with a wideband characteristic impedance bandwidth. The antenna consists of a coplanar waveguide fed radiating patch and two coplanar ground planes. The ground planes partially radiate and responsible for achieving a wide bandwidth with a small structure. The effect of the ground planes on the operating bandwidth are investigated with the help of current distribution and discussed in detail with supporting parametric analysis. A prototype has been fabricated and the measured results are also presented.

II. ANTENNA CONFIGURATION

The geometry of the proposed CPW-fed planar antenna for wideband operations is shown in Fig. 1. For the design studied here, the antenna is etched on the same side of a low cost FR4 substrate with the dielectric constant, ε_r of 4.6 and the substrate thickness, h of 1.6mm, while the other side is without any metallization. A CPW transmission line, which consists of a metal strip thickness of W_{f1} and a gap distance of d between the single strip and the coplanar ground plane, is used for feeding the antenna. It is important to note that here W_{f1} corresponds to 50Ω CPW feed line.

The ground planes are unsymmetrical to each other. On the right side an inverted L-shaped ground plan is positioned, which comprises an overlapped vertical and horizontal sections with dimension of $W_{r1}\times L_{r1}$ and $t_{r1}\times L_{r2}$. These two parts are overlapped on an area of $t_{r1}\times L_{r1}$. However, on the left side a U-shaped ground plane is used to attain the lower frequencies of the broadband antenna. The U-shaped ground has a length of L_{l2} and the dimensions of upper and lower arm are $W_{l2}\times t_{l2}$ and $(W_{l1}-t_{l1})\times L_{l1}$, respectively.

The basis of the antenna structure is of vertical bow-tie shaped with unequal wings. The total length of the radiating element is L_{f2}. The tapered transition for the lower wing is L_{f3}, which is W_{f2} wide at that position. On the other hand, the length of upper wing is L_{f4} and final breadth is W_{f3}. The lower wing connected at the end of the L_{f2} long CPW feed line.

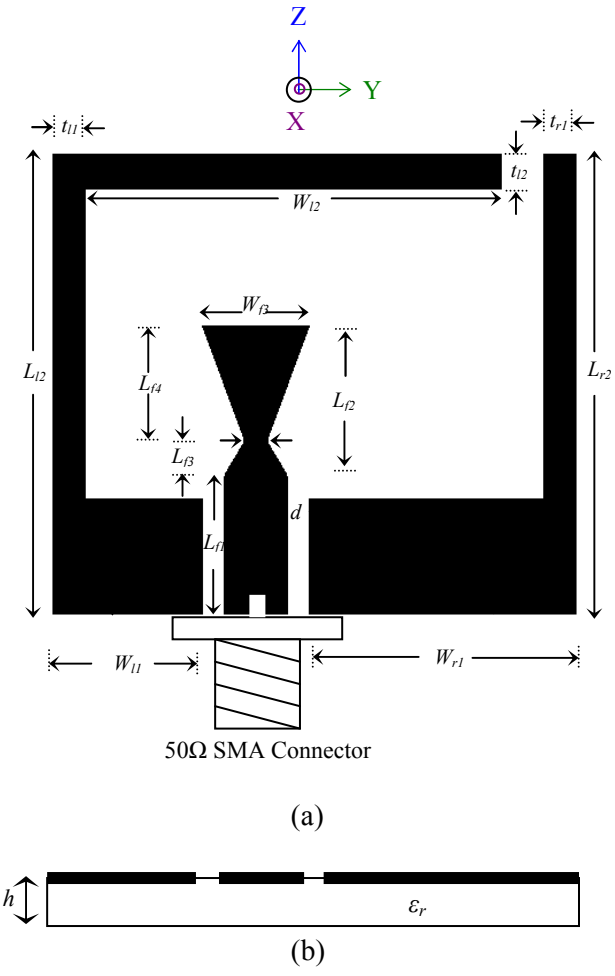

Fig. 1. Schematic diagram of the antenna a) top view, b) side view.

Table 1: Design geometrical parameters of the proposed antenna

Parameters	***Value in* mm**
{W_{f1}, L_{f1}}	*{3, 6}*
{ W_{f2}, W_{f3}, L_{f2}, L_{f3}, L_{f4}}	*{1, 5, 6.5, 1.5,5}*
{ W_{l1}, W_{l2}, L_{l1}, L_{l2}, t_{l1}, t_{l2}}	*{7, 19.5, 5, 20, 1.5, 1.5}*
{ W_{r1}, L_{r1}, L_{r2}, t_{r1},}	*{12.5, 5, 20, 1.5}*

To investigate the performance of the proposed antenna configurations in terms of

achieving the wideband operations a commercially available full-wave, method-of-moment code based electromagnetic simulator Zeland IE3D version 12 [10], was used for required numerical analysis and obtaining the proper geometry parameters in Fig. 1, and then the optimal dimensions were determined from experiments. The details of various parameters of the antenna printed on FR4 substrate are listed in Table 1 for better convenience.

III. INVESTIGATION & ANALYSIS

In this section, the effects of the proposed slot antenna parameters are discussed and analyzed using IE3D software, to facilitate more elaboration of the design and optimization processes for readers. Primarily, with the help of the current distribution, the analysis has been carried out to investigate the partial radiation of the antenna coplanar ground planes. At the same time, to derive some mathematical equations corresponding to the current paths of resonant frequencies within the wide bandwidth. The analysis covers the influences of varying the lengths and width of the arms of the inverted L-shaped right ground and U-shaped right ground plane on VSWR, the implication of choosing the shape of vertical-bow-tie patch for the design and selecting the size of the feeding line for achieving the best performance of wide bandwidth. For better convenience of the effect on the performance of the antenna upon changing the parameters, only one parameter is changed at a time, while keeping others unchanged.

A. Current distribution

The excited surface current distributions, obtained from the IE3D simulation, on the radiating edges of the proposed antenna at the four resonant frequencies, namely 3.59GHz, 4.35GHz, 6GHz, and 8.45GHz, respectively, are presented in Figs. 2 and 3. Arrows show the direction of the current direction and the darker color shows the current intensity on that area of the antenna, while the blue color region shows the null current at that portion. As expected, four dominating current paths have been found, which primarily cause of four resonant modes. These four resonances adding side by side with each other form the broad impedance bandwidth. The path equations at each resonance are tabulated in Table 2. These equations provide the some basic information about the dependencies of resonant frequencies upon various dimensions of the antenna.

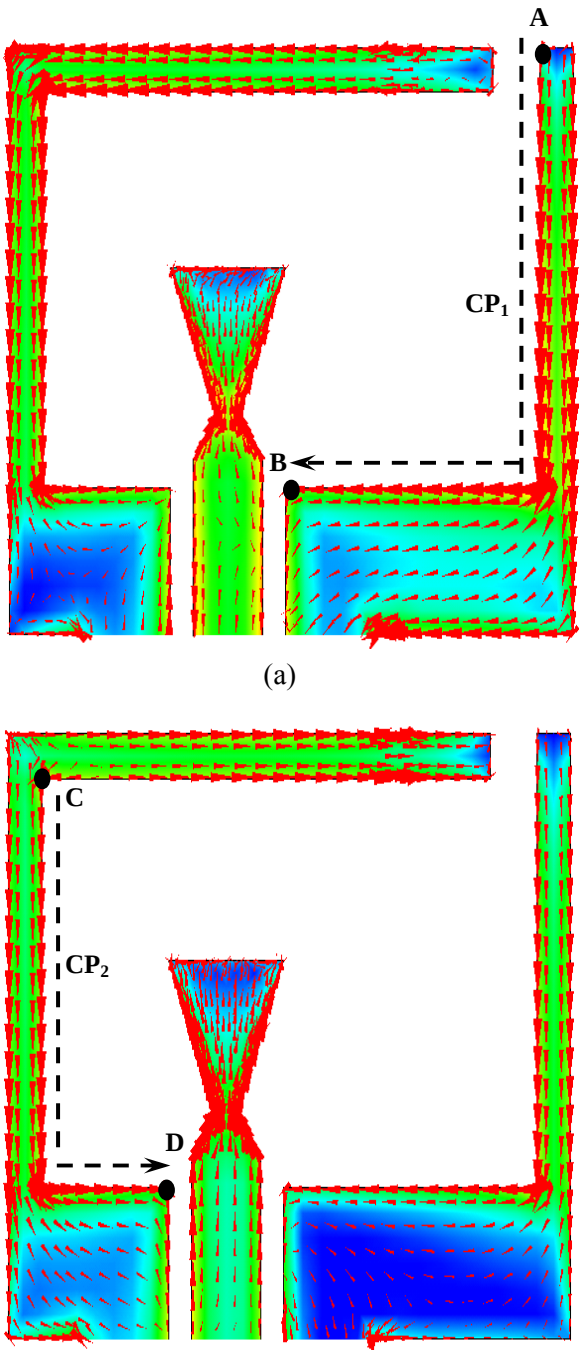

Fig. 2. Surface current distribution of the proposed antenna a) 3.59GHz, b) 4.35GHz.

At f = 3.59GHz, the current around inner edge of the right ground plane of the CPW antenna is stronger than other areas. But current direction at f

= 4.35GHz is more concentrated in the lower inner side of the left ground plane. The third resonance is particularly due to the monopole like behavior of the CPW-fed radiating element. The current path clearly observed by the intensity of current components and marked as CP_3 in Fig. 3(a). On the other hand, the forth resonance of the antenna is due to the dipole like behavior of the left U-shaped ground plan. The dominating current path is denoted by CP_3 and marked by a black dotted line in Fig. 3(b). It is noted from Table 3 that in both of the first two resonant points the current paths corresponds to a length which is slightly longer than one-quarter wavelength of the respective operating frequencies. And for the forth resonant it is also marginally longer than the one-half wavelength of the respective frequency. These deviations can be attributed to the additional effect of the loading of the particular resonant part by the remaining non-resonant part of the whole structure.

Table 2: Information derived from the current distribution analysis

Resonance Number	Path Equation
1	$CP_1 = L_{r2} - L_{r1} + W_{r1} - t_{r1}$
2	$CP_2 = L_{l2} - L_{l1} - t_{l2} + W_{l1} - t_{l1}$
3	$CP_3 = L_{f1} + \sqrt{L_{f3}^2 + \{(W_{f1} - W_{f2})/2\}^2} + \sqrt{L_{f4}^2 + \{(W_{f3} - W_{f2})/2\}^2} + W_{f3}/4$
4	$CP_4 = L_{l2} - L_{l1} + W_{l1} - t_{l1}$

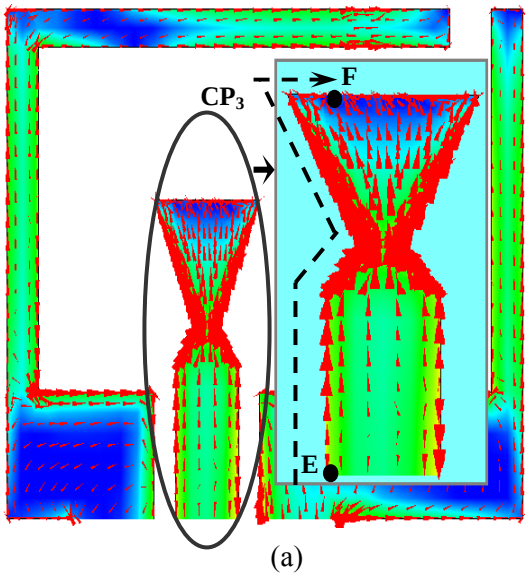

(a)

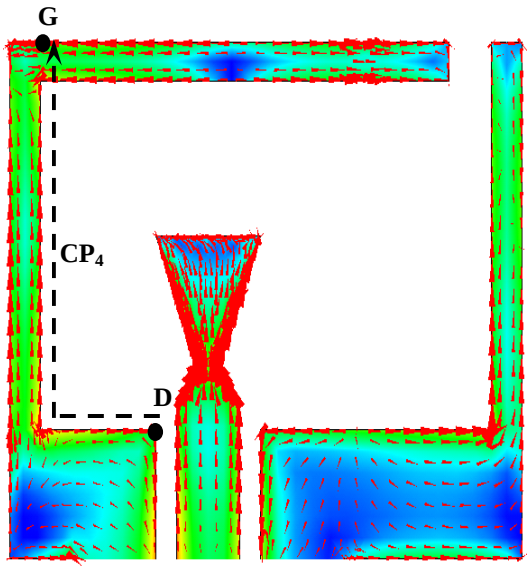

(b)

Fig. 3. Surface current distribution of the proposed antenna a) 6GHz, b) 8.45GHz.

Table 3: Current path relative to free space wavelength (λ_o)

Resonance Number	Resonant Point	Current Path	Relative to free space wavelength (λ_o) at respective resonance
1	3.59GHz	CP_1 (A-B)	0.311 λ_o
2	4.35GHz	CP_2 (C-D)	0.275 λ_o
3	6GHz	CP_3 (E-F)	0.244 λ_o
4	8.45GHz	CP_4 (D-G)	0.577 λ_o

B. Dependence on length of right ground plane L_{r2}

In order to examine the sensitivity of L_{r2} on the first resonance frequency pointed out in the preceding section, a parametric analysis has been done. The results are presented in Fig. 4. As predicted, the increment of L_{r2} decreases the first resonance, while have some effects on the impedance matching on other resonant point. It is important to observe that upto L_{r2}=15mm the first and second resonances coincided and could not be noted separately from each other. However, as L_{r2} increases to 20mm the current path increased and the first resonance is cleared out.

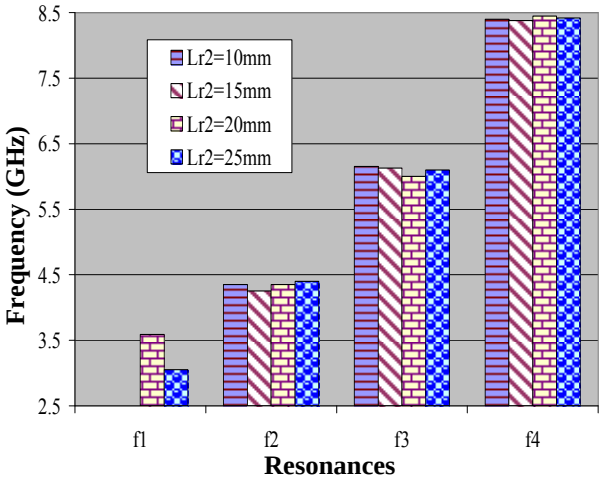

Fig. 4. Effect on resonant frequencies due to change of L_{r2}.

C. Dependence on lower arm length of left U-shaped ground plane L_{l1}

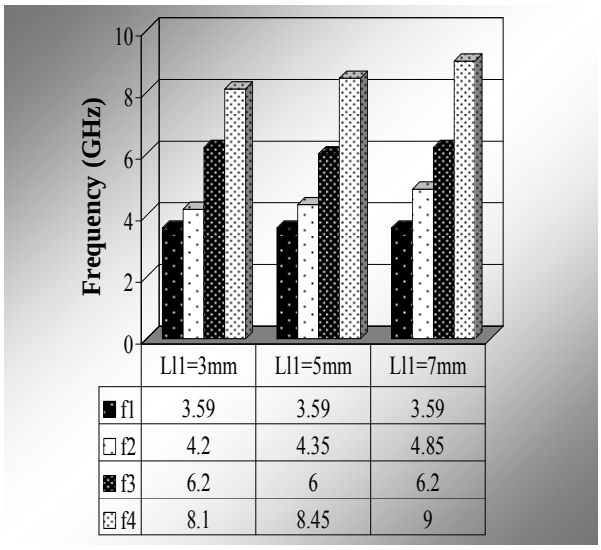

Fig. 5. Effect on resonant frequencies due to change of L_{l1}.

Figure 5 projects the effect of changing L_{l1} on the resonances. As discussed previously, the length of L_{l1} mainly influences the second (f2) and forth resonance (f4). As seen from the plot, both of the resonant frequencies tend to increase as L_{l1} is increased from 3 to 7mm. This is also justified by the mathematical expression of CP2 and CP4 mentioned in Table 2. This may be a way to increase the overall bandwidth of the antenna. Although the increment of resonances reduces the impedance matching, it makes discontinuity in the operating bandwidth.

D. Dependence on CPW-fed radiation element parameters W_{f2} & W_{f3}

The mathematical equation for the third current path, CP3 leads us to the effect of changing W_{f2} and W_{f3}, which is verified by the parametric study on both of these parameters shown in Fig. 6, keeping all others the same. The value of W_{f2} is increased from 0.5mm up to 5mm and the third resonant point increases from 5.85 to 6.43GHz. The contradictorily increment of W_{f3} decreases the third resonant point. However, the change of these parameters also has some additional effect on other resonances, but they are mainly due to the loading mismatch.

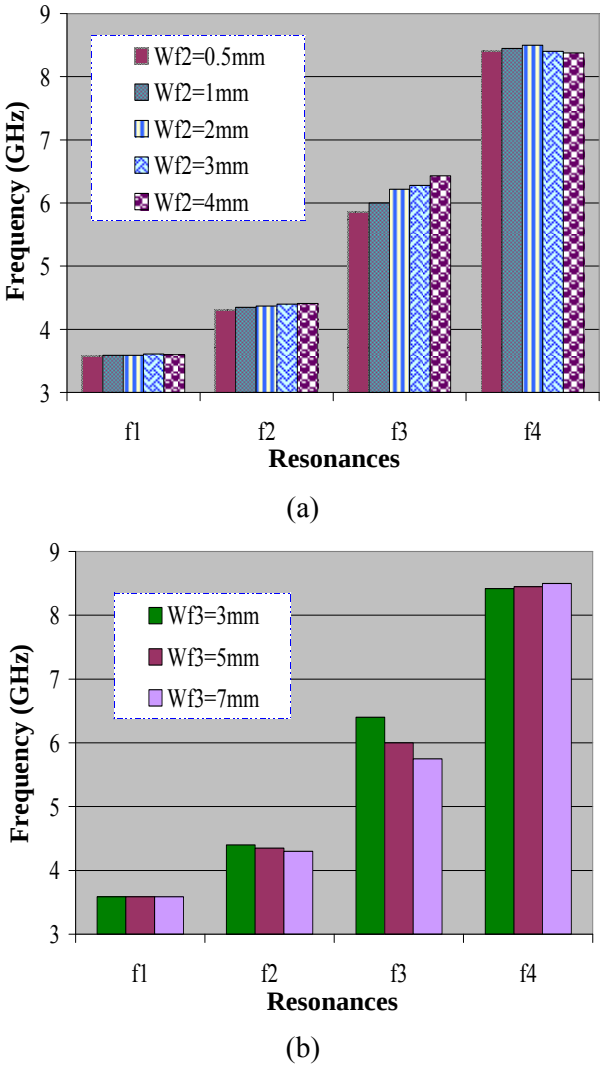

Fig. 6. Effect on resonant frequencies due to change of (a) W_{f2} and (b) W_{f3}.

E. Dependence on coupling gap d between the feed line and ground plane

Additionally, an important feature of the proposed antenna is the influence of impedance matching caused from the coupling effects between the feed line and the coplanar ground plane over the whole operating band, especially over the first and forth resonances. For this, the effect of the gap distance d on the performance of the proposed antenna was also studied and presented in Fig. 7. The obtained results indicate that the VSWR increases and consequently the bandwidth of the antenna are reduced with increasing distance of *d*. The first and forth antenna resonances tend to rise to higher frequencies with the increase in VSWR while the third resonance decreases to lower frequency. However, the second resonance seems to have no effect upon changing the coupling gap between the feed line and ground plane.

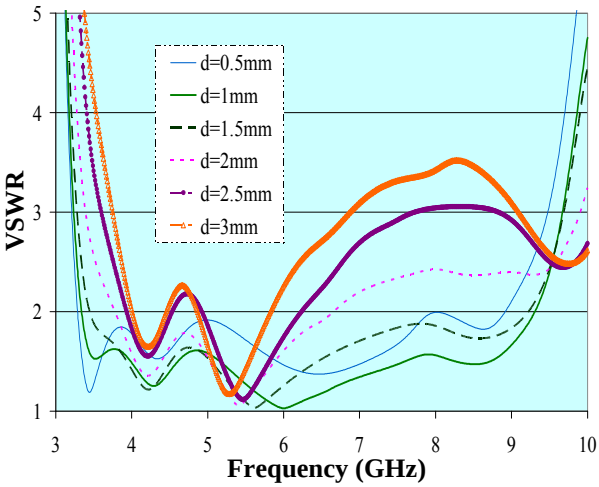

Fig. 7. Effect on resonant frequencies due to change of *d*.

IV. RESULTS AND DISCUSSIONS

The proposed coplanar fed broadband antenna has been prototyped for the verification and measured using Agilent E9362C network analyzer. It was seen that the measured results agrees the simulated results. The prototypes are shown in Fig. 8.

The measured and simulated voltage standing wave ratios (VSWR) of the proposed antenna (denoted by a solid and dashed line, respectively) are depicted in Fig. 9. The measured VSWR curve shows that the proposed antenna produces a total bandwidth of 5.97GHz ranging from 3.53GHz to 9.5GHz below VSWR $\leq$ 2, which is equivalent to 92% impedance bandwidth centered at 5.52GHz. Nevertheless, the simulated VSWR graph shows a bandwidth of 5.99GHz (94.5%, 2 $\geq$ VSWR) from 3.34GHz to 9.33GHz. The slight difference of the simulated and measured results can be attributed to the fabrication and measurement limitations.

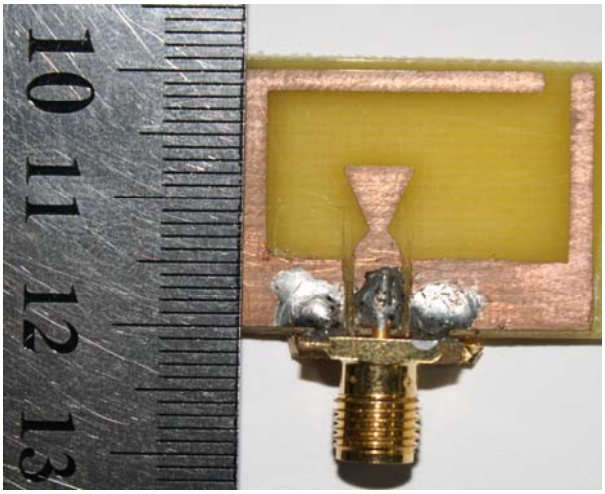

Fig. 8. Photograph of the fabricated prototype of the proposed wideband antenna.

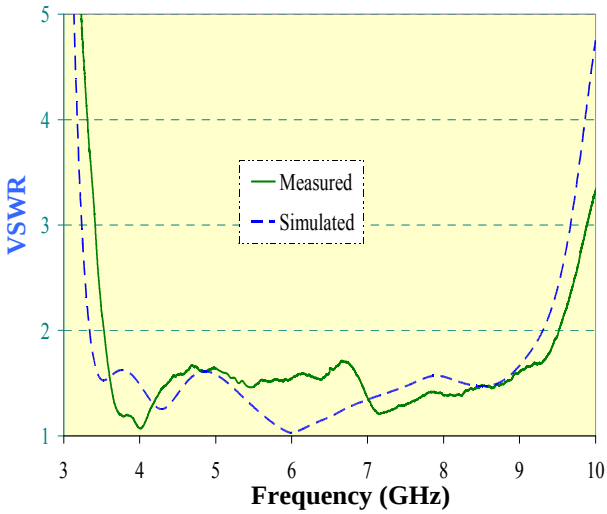

Fig. 9. Simulated and measured VSWR of the proposed wideband antenna.

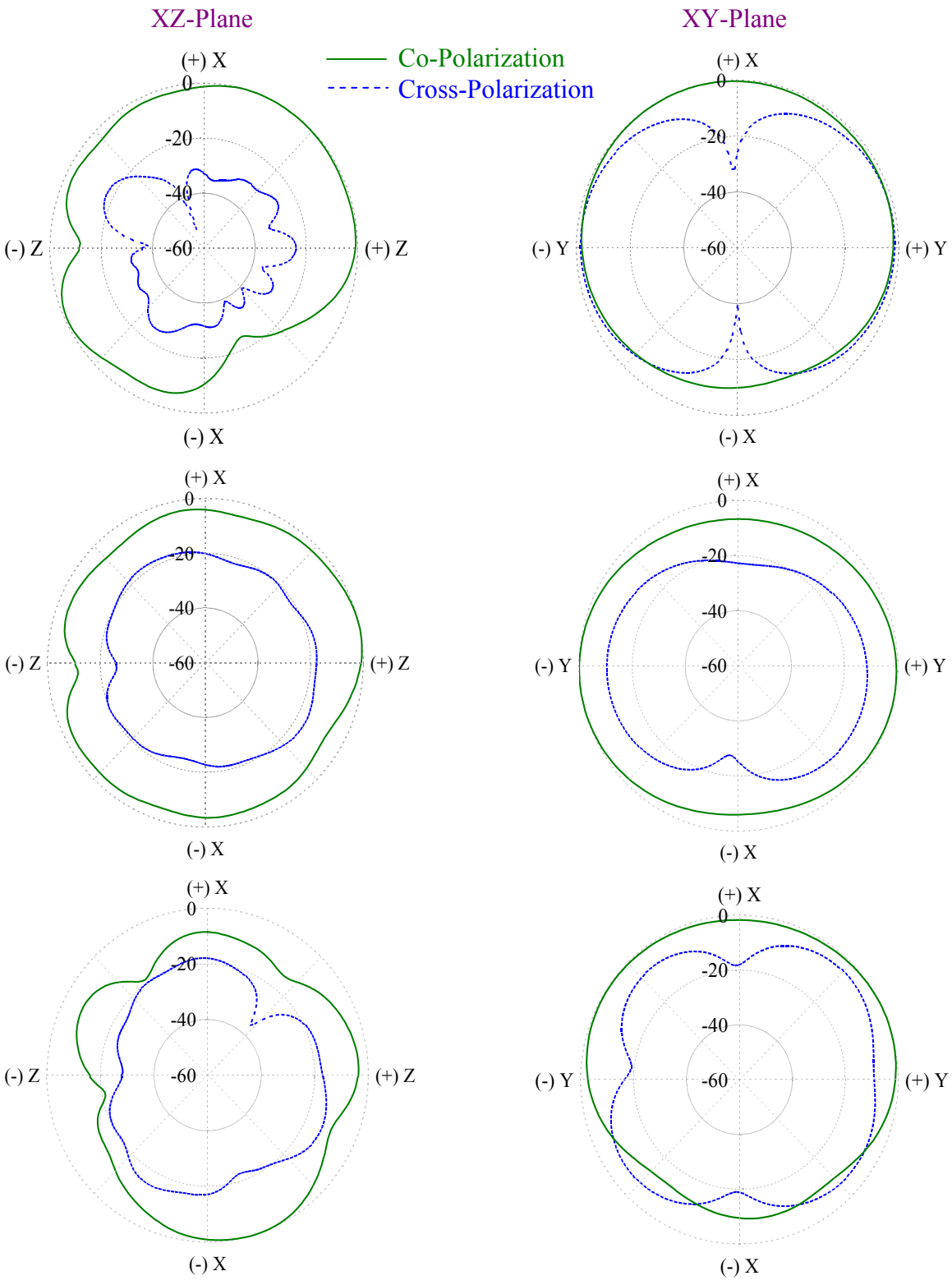

Fig. 10. Radiation pattern (XZ & XY-plane) of the proposed antenna at 4GHz, 6GHz, and 8.4GHz.

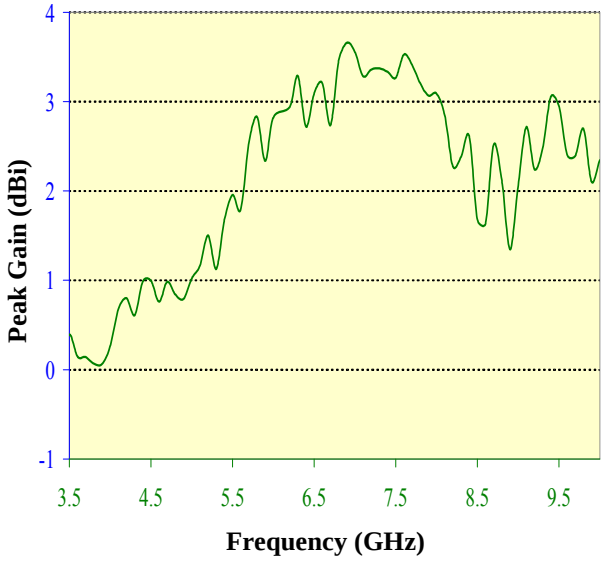

(a)

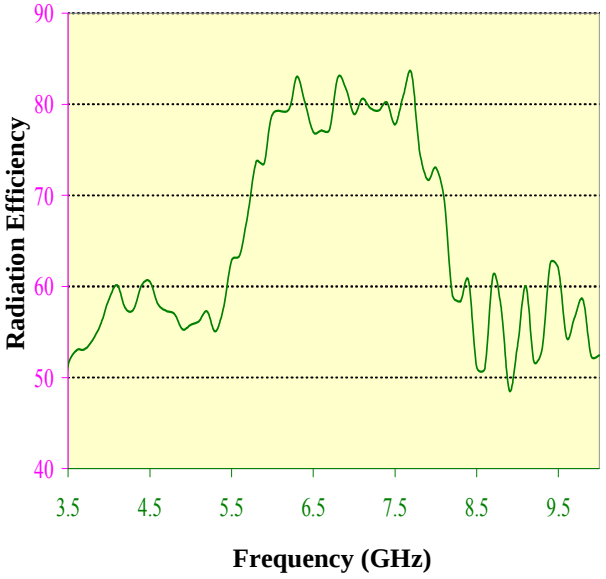

(b)

Fig. 11. Measured (a) gain and (b) radiation efficiency of the designed antenna.

The measured E (XZ) and H (XY) plane radiation patterns of the proposed antenna at 4GHz, 6GHz, and 8.4GHz have been shown in Fig. 10. It can be seen that the designed antenna produce a nearly omni directional radiation pattern. In spite of the slight unsymmetrical structure of the antenna, an almost symmetrical radiation pattern with no back lobe radiation has been observed. One of the significant advantages of a symmetrical radiation pattern is that the maximum power direction would always be at the broadside direction and would not shift to different directions at different frequencies. Consequently, the antenna shows a broad half power beam width (HPBW) of almost ± 80, ± 85, and ± 65 degrees in the E-plane as well as ± 140, ± 95, and ± 100 degrees in the H-plane at the frequencies of 4GHz, 6GHz, and 8.4GHz, respectively. However, it was realized that the cross polarization level for the antenna is higher at low frequency, 4GHz, which is also a degenerative effect of compact antennas. For compact antennas, the ratio of width and height increases, which results in a greater surface wave to produce diffraction at the dielectric's edge, thus contributing to higher cross-polarization levels [11]. However in the higher frequencies, the cross polarization goes lower, as the respective size of the antenna increases with the decrease in wavelength for higher frequencies.

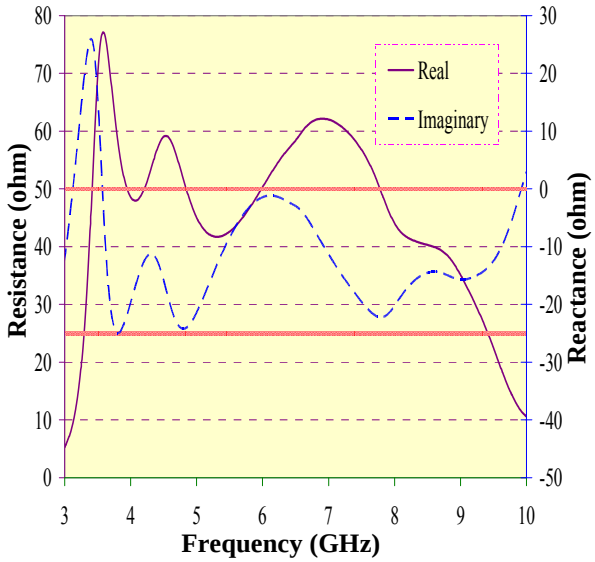

Fig. 12. Simulated input impedance of the proposed wideband antenna.

Figure 11(a) illustrates the measured maximum antenna gain for frequencies over the whole operating band. The antenna exhibits an overall gain of more than 0*dBi,* with a gain variation of about 3*dBi* within the entire bandwidth. The peak gain of 3.5*dBi* is attained at near 7GHz. The gain variation of the antenna can be attributed to the copper loss of the antenna

which was not taken into account in the simulation and also the loss due to the SMA connector of the antenna. The radiation efficiency of the antenna is depicted in Fig. 11(b). Regardless of the high loss ($\tan\delta = 0.02$) of the FR4 substrate, the antenna shows a minimum efficiency of 50%. It is suggested to use low loss Duroid substrate to increase the radiation efficiency and gain of the proposed antenna. But in that case, the cost of the antenna would increase. That's what this phenomenon in not premised.

The antenna input impedance plotted in Fig. 12 displays four good quality factor resonances within the frequency band of interest which allows a wide band impedance matching. The resonances are identified as local maxima of the impedance imaginary part. The antenna shows low matching in the first resonance, which can be caused by the inductive peak of the imaginary curve. However, this peak in the inductive region is also responsible for the good radiation efficiency at the first resonance point shown in Fig. 11(b). Other than the first resonance, the capacitive behavior of the antenna prevents the imaginary part from crossing zero, particularly for good quality factor resonances [12]. The real part of input impedance literally swings around the 50Ω line over the entire bandwidth of the antenna. It is interesting to note that when the real part of input impedance falls below 25Ω the antenna voltage standing wave ratio goes over 2. So in a way, the whole bandwidth (VSWR ≤ 2) can also be defined by the 25Ω line of the real input impedance curve.

IV. CONCLUSION

A printed 50Ω fed antenna for wireless communications has been presented. The proposed antenna with two unsymmetrical coplanar ground elements, namely inverted-L and U-shaped ground provides a wideband operation easily covering 5.97GHz from 3.53GHz to 9.5GHz. The effect of the partial radiating ground plane has been analyzed pointing out the mathematical expression of the current path from the simulated current distribution and was verified by means of the parametric analysis. Besides its wideband characteristics, the proposed antenna remains compact and possesses maximum 3.5*dBi* gain with good radiation patterns, making it a good candidate for wireless communication applications.

ACKNOWLEDGMENT

The authors would like to thank the Institute of Space Science (ANGKASA) of Universiti Kebangsaan Malaysia (National University of Malaysia).

REFERENCES

[1] W.-C. Liu and J.-K. Chen, "A Dual-Band CPW-Fed Monopole Antenna for IMT-2000/WLAN," *Microwave Journal*, vol. 53, no. 5, pp.124-134, 2010.

[2] R. B. Hwang, "A Broadband CPW-Fed T-Shaped Antenna for Wireless Communications," *IEE Proc. - Microwave Antennas Propagations*, vol. 151, no. 6, pp. 537-543, 2004.

[3] J. William and R. Nakkeeran, "A Novel Compact CPW-Fed Wideband Slot Antenna," *3rd European Conference on Antennas and Propagation*, pp. 147-1474, 2009.

[4] A. U. Bhobe, C. L. Holloway, M. Piket, and R. Hall, "Wide-Band Slot Antennas with CPW Feed Lines: Hybrid and Log-Periodic Designs," *IEEE Transactions on Antennas and Propagation*, vol. 52, no. 10, pp. 2545-2554, 2004.

[5] Nasimuddin and Z. N. Chen, "Wideband Multilayered Microstrip Antennas Fed by Coplanar Waveguide-Loop with and without Via Combinations," *IET Microwave Antennas Propagations*, vol. 3, no. 1, pp. 85-91, 2009.

[6] A. A. Eldek, A. Z. Elsherbeni, C. E. Smith, and K. F. Lee "Wideband Planar Slot Antennas," *Applied Computational Electromagnetic Society (ACES)* Newsletter, vol. 19, no. 1, pp. 35-48, 2004.

[7] R. H. Patnam, "Broadband CPW-Fed Planar Koch Fractal Loop Antenna," *IEEE Antennas and Wireless Propagation Letters*, vol. 7, pp. 429-431, 2008.

[8] K. Han, Y. Park, H. Choo, and I. Park, "Broadband CPS-Fed Yagi-Uda Antenna," *Electronics Letters*, vol. 45, no. 24, pp. 1207-1209, 2009.

[9] T. N. Chang and G. A. Tsai, "A Wideband Coplanar Waveguide-Fed Circularly Polarised Antenna," *IET Microwave Antennas Propagations*, vol. 2, no. 4, pp. 343-347, 2008.

[10] IE3D version 12, 2010. California: Zeland Software Inc.

[11] I-F. Chen and C.-M. Peng, "A Novel Reduced Size Edge-Shorted Patch Antenna for UHF Band Applications," *IEEE Antennas and Wireless Propagation Letters*, vol. 8, pp. 475-477, 2009.

[12] F. Demeestere, C. Delafield, and J. Keignart, "A Compact UWB Antenna with a Wide Band Circuit Model and a Time Domain Characterization," *IEEE International Conference on Ultra-Wideband*, pp. 345-350, 2006.

Planar Compact U-Shaped Patch Antenna with High-Gain Operation for Wi-Fi/WiMAX Application

Jui-Han Lu[1] and Hai-Ming Chin[2]

[1] Department of Electronic Communication Engineering

[2] Department of Marine Engineering
National Kaohsiung Marine University, Kaohsiung, Taiwan 811, R.O.C.
jhlu@mail.nkmu.edu.tw

Abstract ─ A planar inverted U-shaped patch antenna with high-gain operation applied for WLAN/WiMAX access point or base station has been proposed and investigated. It provides relatively wider impedance bandwidth of 180 MHz covering the operating bandwidth for WLAN/WiMAX system. The proposed planar patch antenna also provides the directional radiation patterns with maximum antenna peak gain and efficiency of 8.0 dBi and 80% across the operating band, respectively. Only with the antenna size of 44 × 35 × 4.0 mm^3, the proposed patch antenna has the compact operation with more than 13% antenna size reduction.

Index Terms ─ Patch antenna, WiMAX, WLAN.

I. INTRODUCTION

In the last few years, due to tremendous development in wireless local area network (WLAN), especially for the IEEE 802.11a/b/g WLAN standards in the 2.4 GHz (2400–2484 MHz), 5.2 GHz (5150–5350 MHz), and 5.8 GHz (5725–5825 MHz) bands, dual-band operations are becoming demanding in practical applications. However, with the consideration of both market and technology ready to mass production, single-band 2.4/2.6 GHz for WLAN/WiMAX system with high-gain operation for access point (AP) or base station (BS) can specifically meet the low-cost requirements for the users. The related antenna designs have been presented by using a microstrip antenna [1], an array antenna [2], the suspended patch antenna [3], the roll monopole antenna [4], and the H-shaped slot antenna [5]. But, there is the disadvantage of having a larger antenna size for the above presented designs unable to meet the dimension consideration of the product. Therefore, in this article, by introducing the standard printed circuit board (PCB) substrate and production technology, we propose a novel printed inverted U-shaped patch antenna inset with a pair of T-shaped strips parallel coupled along the feed microstrip line to obtain 2.4/2.6 GHz operation for WLAN/WiMAX communication system. From the related results, it is found that, by properly adjusting the length and width of the T-shaped strips, the operating bandwidth is 180 MHz, which is enough for 2.4/2.6 GHz for WLAN/WiMAX communication system. Also, compared with the regular rectangular patch antenna, this proposed monopole antenna has more than 13% antenna size reduction to obtain a compact operation. The proposed inverted U-shaped patch antenna also provides antenna peak gain of 8.0 dBi with compact antenna size, which is more than that of the presented antenna designs [1-5] under the same peak gain consideration. Details of the proposed compact patch antenna designs are described, and experimental results for the obtained high-gain performance operated at the 2.4 GHz band are presented and discussed.

II. ANTENNA DESIGN

To meet the low-profile requirement for the WLAN or WiMAX access point, a novel planar compact inverted U-shaped antenna with high-gain operation has been proposed. Figure 1 illustrates the geometry of the proposed compact inverted U-shaped patch antenna. A 50Ω mini coaxial cable line is fed at the end of the

microstrip line etched on the inexpensive FR-4 substrate with the volume of 44 × 35 × 0.4 mm^3, dielectric constant $\varepsilon_r = 4.7$, and loss tangent $\tan\delta = 0.0245$. A pair of T-shaped coupling strips are inset along the inside edge of the inverted U-shaped patch antenna, which is parallel to the microstrip line. The electromagnetic energy is transferred from the microstrip line to the proposed T-shaped coupling strips to excite the compact patch antenna. The iron plate is used as the ground plane with a volume of 58 × 37 × 0.1 mm^3, which has the air gap of 3.5 mm under the proposed patch antenna with the FR-4 substrate in this study. For achieving the resonant mode at 2.4 GHz band (IEEE 802.11 b/g or Bluetooth), a surface current route of the patch antenna starting from the point A to the end point B is chosen to be about 35 mm corresponding approximately to a quarter-wavelength for 2.4 GHz band, which is different from the regular rectangular patch antenna design with half-wavelength resonance. Therefore, in this article, the compact patch antenna design can be easily obtained. And, by properly adjusting the length and width of the T-shaped coupling strips, good impedance matching across the operating band can easily be achieved.

III. EXPERIMENTAL RESULTS AND DISCUSSIONS

To demonstrate the above deduction and guarantee the correctness of the simulated results, the electromagnetic simulator HFSS based on the finite element method [6] has been applied for the proposed compact patch antenna design. Figure 2 shows the related simulated and experimental results of the VSWR for the proposed compact patch antenna design of Fig. 1. The related results are listed in Table 1 as comparison. Probably due to the permittivity variation of the FR4 substrate, there are slight discrepancies between the simulated and the measured results. Results show the satisfactory agreement for the proposed compact patch antenna design operating at the 2.4 GHz band. From the experimental results, the measured impedance bandwidth (VSWR≦2) can reach 7.3 % (180 MHz) for 2.4 GHz band which provides much greater bandwidths than that (57 MHz, 2.3%) of the regular rectangular patch antenna (51 × 35 × 4.0 mm^3) to meet the 802.11 b/g specifications. To fully comprehend the excitation for WLAN band, the surface current distributions at 2.45 GHz are shown in Figure 3. It is clearly seen that the surface current path from point A to point B in this study is about 1/4 wavelength, not 1/2 wavelength distribution of the conventional rectangular patch antenna mode, which makes the proposed compact patch antenna need less material dimension to reduce the manufacture cost. Compared with the regular rectangular patch antenna of 51 × 35 × 4.0 mm^3, to operate at 2.45 GHz band, this proposed patch antenna has more than 13% antenna size reduction to obtain compact operation.

The measured VSWR with various gap widths between the T-shaped coupling strip and the inside edge of the proposed compact patch antenna are shown in Fig. 4. The related results are also listed in Table 2 as comparison. It is easily found that the operating frequency of the resonant mode significantly decreases with the gap width increased, which means the surface current route of the patch antenna starting from the point A to the end point B increased. Figure 5 shows the measured VSWR with various inside edge lengths of the inverted U-shaped patch antenna. The operating frequency of the resonant mode significantly decreases due to the surface current path of the compact patch antenna increasing with the inside edge length increased.

Table 1: Simulated and measured VSWR against frequency for the proposed patch antenna; L_{s1} = 16.7 mm, W_{s1} = 3 mm, L_{s2} = 21.7 mm, W_{s2} = 17 mm, W_{t1} = 1 mm, L_{t1} = 3 mm, W_{t2} = 1 mm, L_{t2} = 14 mm, W_{p1} = 35 mm, L_p = 44 mm, H = 4 mm

	f_1 (MHz)	BW (MHz, %)
The proposed patch antenna (Simulated)	2530	140, 5.5
The proposed patch antenna (Measured)	2469	180, 7.3
The regular rectangular patch antenna (Simulated)	2469	57, 2.3

The radiation measurement of the proposed compact inverted U-shaped patch antenna is carried out in anechoic chamber by introducing NSI 800F far-field system. Figure 6 shows the measured peak gain and efficiency across the operating band. The maximum measured peak

antenna gain and efficiency is 8.0 dBi and 80% at 2.45 GHz, respectively. The gain variation across the operating band is less than 1.0 dB. The measured 2D and 3D radiation patterns of the proposed compact patch antenna at 2.45 GHz are plotted in Fig. 7. Note that the radiation patterns are directional in the whole *x*-*z* plane and *y*-*z* plane.

Table 2: Performance for the proposed compact patch antenna with various gap widths; other antenna parameters are given in Table 1

W_{t1} (mm)	f (MHz)	BW (MHz, %)
1.0	2469	180, 7.3
2.0	2403	214, 8.9
3.0	2334	182, 7.8

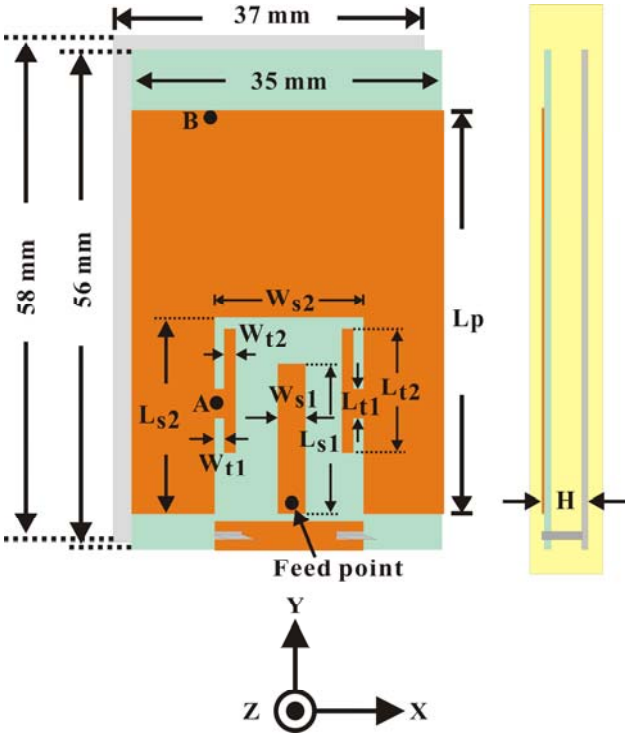

Fig. 1. Geometry of the proposed compact patch antenna with high-gain operation.

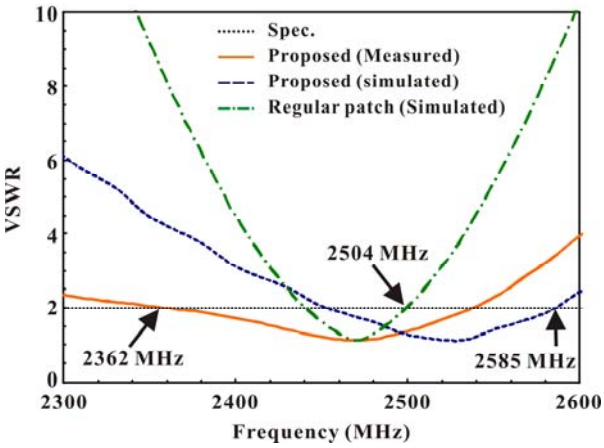

Fig. 2. Simulated and measured VSWR against frequency for the proposed compact patch antenna; antenna parameters are given in Table 1.

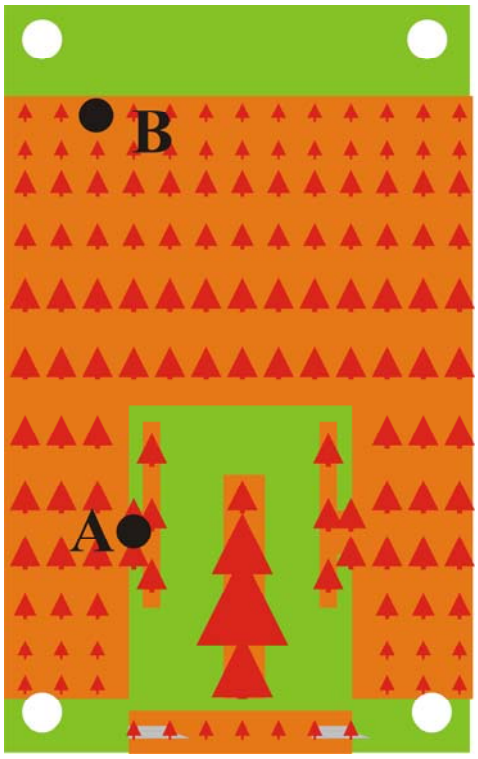

Fig. 3. Simulated surface current distribution for the proposed compact patch antenna at f = 2450 MHz.

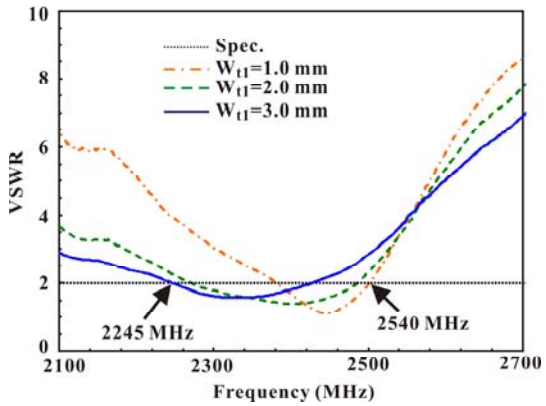

Fig. 4. Measured VSWR with various gap widths between the T-shaped coupling strip and the inside edge of the proposed patch antenna; other antenna parameters are given in Table 1.

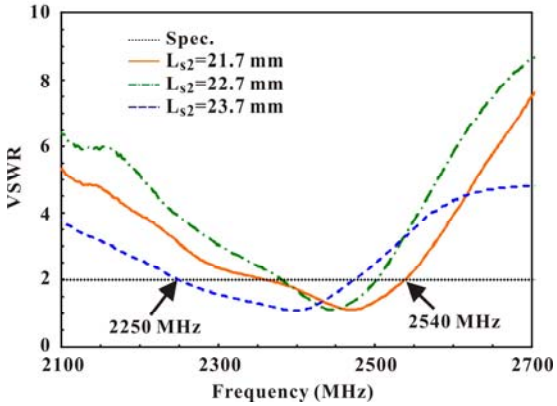

Fig. 5. Measured VSWR with various inside edge lengths of the inverted U-shaped patch antenna; other antenna parameters are given in Table 1.

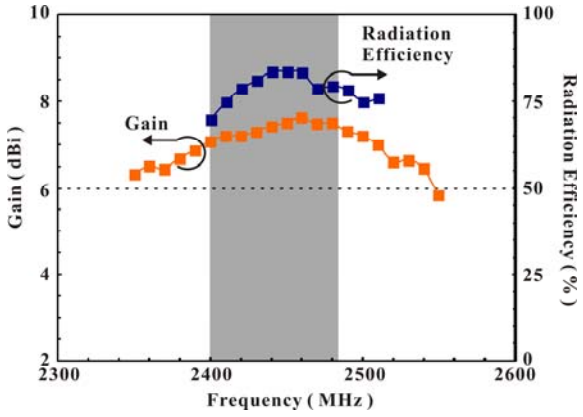

Fig. 6. Measured peak gain and efficiency across the operating frequency for the proposed compact patch antenna.

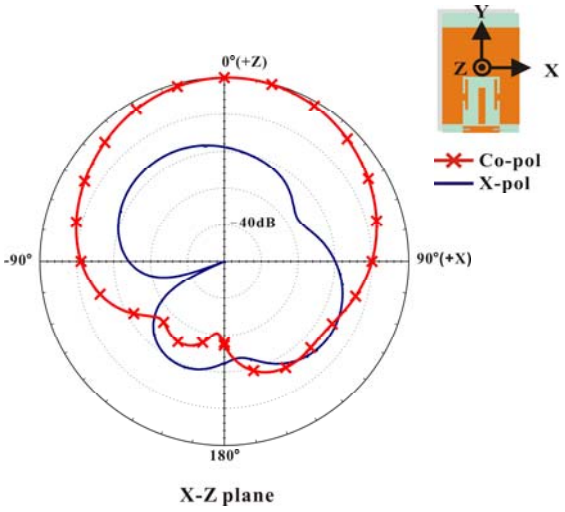

(a)

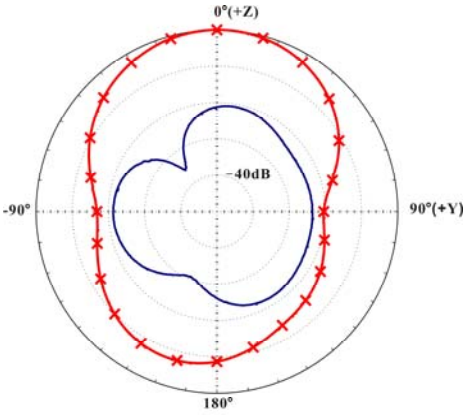

(b)

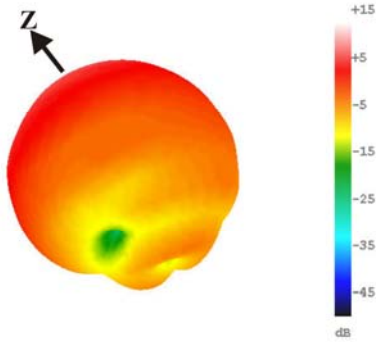

(c) 3D pattern

Fig. 7. 2D and 3D radiation patterns for the proposed compact patch antenna at f = 2450 MHz.

IV. CONCLUSIONS

A planar inverted U-shaped patch antenna with high-gain operation for Wi-Fi/WiMAX applications has been proposed and investigated. It provides relatively wider impedance bandwidth of 180 MHz covering the operating bandwidth for WLAN/WiMAX system. The proposed planar patch antenna also provides the directional radiation patterns with maximum antenna peak gain and efficiency of 8.0 dBi and 80% across the operating band, respectively. Only with the antenna size of 44 × 35 × 4.0 mm^3, the proposed patch antenna has the compact operation with more than 13% antenna size reduction.

ACKNOWLEDGMENT

This paper was supported by the National Science Council (NSC), Taiwan, R.O.C., under Grant NSC97-2221-E-022-005-MY3 and NSC94-2622-E-022-004-CC3.

REFERENCES

[1] K. L. Wong, F. S. Chang, and T. W. Chiou, "Low-Cost Broadband Circularly Polarized Probe-Fed Patch Antenna for WLAN Base Station," *IEEE AP-S Int. Symp. Dig.,* vol. 2, pp. 526-529, 2002.

[2] F. R. Hsiao, K. L. Wong, and T. W. Chiou, "Omni-Directional Planar Dipole Array Antenna for WLAN Access Point," *IEEE AP-S Int. Symp. Dig.,* vol. 2, pp. 2-5, 2003.

[3] R. Gardelli, G. Cono, and M. Albani, "A Low-Cost Suspended Patch Antenna for WLAN Access Points and Point-to-Point Links," *IEEE Antennas and Wireless Propagation Lett.*, vol. 3, pp. 90-93, 2004.

[4] Z. N. Chen, "Broadband Roll Monopole," *IEEE Trans. Antennas Propagat.*, vol. 51, pp. 3175-3177, Nov. 2003.

[5] Y. F. Lin, P. C. Liao, P. S. Cheng, H. M. Chen, C. T. P. Song, and P. S. Hall, "CPW-Fed Capacitive H-Shaped Narrow Slot Antenna," *IET Electron. Lett.,* vol. 41, pp. 940-942, Aug. 18, 2005.

[6] HFSS version 11.0, Ansoft Software Inc., 2008.

Jui-Han Lu has received the Ph.D. degree in Electrical Engineering from the National Sun Yat-Sen University, Kaohsiung, Taiwan in 1997. He received the ISI Citation Classic Award for "Honoring Excellence in Taiwanese Research" from the Institute for Scientific Information, ISI, and the Science and Technology Information Center (STIC) of the National Science Council, R.O.C. in 2001. Since 2003, he became a Full Professor and was elected as one of the "Ten Outstanding Young Persons" in Taiwan in 2005. His current research interests include antenna design, microwave circuit, and electromagnetic wave propagation.

Hai-Ming Chin joined the Department of Marine Engineering at National Kaohsiung Marine University, Kaohsiung, Taiwan in 1990. Since 2008, he became an Assistance Professor. His current research interests include antenna design and electromagnetic wave propagation.

2011 INSTITUTIONAL MEMBERS

DTIC-OCP LIBRARY
8725 John J. Kingman Rd, Ste 0944
Fort Belvoir, VA 22060-6218

AUSTRALIAN DEFENCE LIBRARY
Northcott Drive
Canberra, A.C.T. 2600 Australia

BEIJING BOOK CO, INC
701 E Linden Avenue
Linden, NJ 07036-2495

DARTMOUTH COLLEGE
6025 Baker/Berry Library
Hanover, NH 03755-3560

DSTO EDINBURGH
AU/33851-AP, PO Box 830470
Birmingham, AL 35283

SIMEON J. EARL – BAE SYSTEMS
W432A, Warton Aerodome
Preston, Lancs., UK PR4 1AX

ENGINEERING INFORMATION, INC
PO Box 543
Amsterdam, Netherlands 1000 Am

ETSE TELECOMUNICACION
Biblioteca, Campus Lagoas
Vigo, 36200 Spain

GA INSTITUTE OF TECHNOLOGY
EBS-Lib Mail code 0900
74 Cherry Street
Atlanta, GA 30332

TIMOTHY HOLZHEIMER
Raytheon
PO Box 1044
Rockwall, TX 75087

HRL LABS, RESEARCH LIBRARY
3011 Malibu Canyon
Malibu, CA 90265

IEE INSPEC
Michael Faraday House
6 Hills Way
Stevenage, Herts UK SG1 2AY

INSTITUTE FOR SCIENTIFIC INFO.
Publication Processing Dept.
3501 Market St.
Philadelphia, PA 19104-3302

LIBRARY – DRDC OTTAWA
3701 Carling Avenue
Ottawa, Ontario, Canada K1A OZ4

LIBRARY of CONGRESS
Reg. Of Copyrights
Attn: 407 Deposits
Washington DC, 20559

LINDA HALL LIBRARY
5109 Cherry Street
Kansas City, MO 64110-2498

MISSOURI S&T
400 W 14th Street
Rolla, MO 56409

MIT LINCOLN LABORATORY
Periodicals Library
244 Wood Street
Lexington, MA 02420

NATIONAL CHI NAN UNIVERSITY
Lily Journal & Book Co, Ltd
20920 Glenbrook Drive
Walnut, CA 91789-3809

JOHN NORGARD
UCCS
20340 Pine Shadow Drive
Colorado Springs, CO 80908

OSAMA MOHAMMED
Florida International University
10555 W Flagler Street
Miami, FL 33174

NAVAL POSTGRADUATE SCHOOL
Attn:J. Rozdal/411 Dyer Rd./ Rm 111
Monterey, CA 93943-5101

NDL KAGAKU
C/0 KWE-ACCESS
PO Box 300613 (JFK A/P)
Jamaica, NY 11430-0613

OVIEDO LIBRARY
PO BOX 830679
Birmingham, AL 35283

DAVID PAULSEN
E3Compliance
1523 North Joe Wilson Road
Cedr Hill, TX 75104-1437

PENN STATE UNIVERSITY
126 Paterno Library
University Park, PA 16802-1808

DAVID J. PINION
1122 E Pike Street #1217
SEATTLE, WA 98122

KATHERINE SIAKAVARA
Gymnasiou 8
Thessaloniki, Greece 55236

SWETS INFORMATION SERVICES
160 Ninth Avenue, Suite A
Runnemede, NJ 08078

YUTAKA TANGE
Maizuru Natl College of Technology
234 Shiroya
Maizuru, Kyoto, Japan 625-8511

TIB & UNIV. BIB. HANNOVER
DE/5100/G1/0001
Welfengarten 1B
Hannover, Germany 30167

UEKAE
PO Box 830470
Birmingham, AL 35283

UNIV OF CENTRAL FLORIDA
4000 Central Florida Boulevard
Orlando, FL 32816-8005

UNIVERSITY OF COLORADO
1720 Pleasant Street, 184 UCB
Boulder, CO 80309-0184

UNIVERSITY OF KANSAS – WATSON
1425 Jayhawk Blvd 210S
Lawrence, KS 66045-7594

UNIVERSITY OF MISSISSIPPI
JD Williams Library
University, MS 38677-1848

UNIVERSITY LIBRARY/HKUST
Clear Water Bay Road
Kowloon, Honk Kong

CHUAN CHENG WANG
8F, No. 31, Lane 546
MingCheng 2nd Road, Zuoying Dist
Kaoshiung City, Taiwan 813

THOMAS WEILAND
TU Darmstadt
Schlossgartenstrasse 8
Darmstadt, Hessen, Germany 64289

STEVEN WEISS
US Army Research Lab
2800 Powder Mill Road
Adelphi, MD 20783

YOSHIHIDE YAMADA
NATIONAL DEFENSE ACADEMY
1-10-20 Hashirimizu
Yokosuka, Kanagawa,
Japan 239-8686

APPLIED COMPUTATIONAL ELECTROMAGNETICS SOCIETY JOURNAL
http://aces.ee.olemiss.edu

INFORMATION FOR AUTHORS

PUBLICATION CRITERIA

Each paper is required to manifest some relation to applied computational electromagnetics. **Papers may address general issues in applied computational electromagnetics, or they may focus on specific applications, techniques, codes, or computational issues.** While the following list is not exhaustive, each paper will generally relate to at least one of these areas:

1. **Code validation.** This is done using internal checks or experimental, analytical or other computational data. Measured data of potential utility to code validation efforts will also be considered for publication.

2. **Code performance analysis.** This usually involves identification of numerical accuracy or other limitations, solution convergence, numerical and physical modeling error, and parameter tradeoffs. However, it is also permissible to address issues such as ease-of-use, set-up time, run time, special outputs, or other special features.

3. **Computational studies of basic physics.** This involves using a code, algorithm, or computational technique to simulate reality in such a way that better, or new physical insight or understanding, is achieved.

4. **New computational techniques** or new applications for existing computational techniques or codes.

5. **"Tricks of the trade"** in selecting and applying codes and techniques.

6. **New codes, algorithms, code enhancement, and code fixes.** This category is self-explanatory, but includes significant changes to existing codes, such as applicability extensions, algorithm optimization, problem correction, limitation removal, or other performance improvement. **Note: Code (or algorithm) capability descriptions are not acceptable, unless they contain sufficient technical material to justify consideration.**

7. **Code input/output issues.** This normally involves innovations in input (such as input geometry standardization, automatic mesh generation, or computer-aided design) or in output (whether it be tabular, graphical, statistical, Fourier-transformed, or otherwise signal-processed). Material dealing with input/output database management, output interpretation, or other input/output issues will also be considered for publication.

8. **Computer hardware issues.** This is the category for analysis of hardware capabilities and limitations of various types of electromagnetics computational requirements. Vector and parallel computational techniques and implementation are of particular interest.

Applications of interest include, but are not limited to, antennas (and their electromagnetic environments), networks, static fields, radar cross section, inverse scattering, shielding, radiation hazards, biological effects, biomedical applications, electromagnetic pulse (EMP), electromagnetic interference (EMI), electromagnetic compatibility (EMC), power transmission, charge transport, dielectric, magnetic and nonlinear materials, microwave components, MEMS, RFID, and MMIC technologies, remote sensing and geometrical and physical optics, radar and communications systems, sensors, fiber optics, plasmas, particle accelerators, generators and motors, electromagnetic wave propagation, non-destructive evaluation, eddy currents, and inverse scattering.

Techniques of interest include but not limited to frequency-domain and time-domain techniques, integral equation and differential equation techniques, diffraction theories, physical and geometrical optics, method of moments, finite differences and finite element techniques, transmission line method, modal expansions, perturbation methods, and hybrid methods.

Where possible and appropriate, authors are required to provide statements of quantitative accuracy for measured and/or computed data. This issue is discussed in "Accuracy & Publication: Requiring, quantitative accuracy statements to accompany data," by E. K. Miller, *ACES Newsletter*, Vol. 9, No. 3, pp. 23-29, 1994, ISBN 1056-9170.

SUBMITTAL PROCEDURE

All submissions should be uploaded to ACES server through ACES web site (http://aces.ee.olemiss.edu) by using the upload button, journal section. Only pdf files are accepted for submission. The file size should not be larger than 5MB, otherwise permission from the Editor-in-Chief should be obtained first. Automated acknowledgment of the electronic submission, after the upload process is successfully completed, will be sent to the corresponding author only. It is the responsibility of the corresponding author to keep the remaining authors, if applicable, informed. Email submission is not accepted and will not be processed.

EDITORIAL REVIEW

In order to ensure an appropriate level of quality control, papers are peer reviewed. They are reviewed both for technical correctness and for adherence to the listed guidelines regarding information content and format.

PAPER FORMAT

Only camera-ready electronic files are accepted for publication. The term **"camera-ready" means that the material is neat, legible, reproducible, and in accordance with the final version format listed below.**

The following requirements are in effect for the final version of an ACES Journal paper:

1. The paper title should not be placed on a separate page.

The title, author(s), abstract, and (space permitting) beginning of the paper itself should all be on the first page. The title, author(s), and author affiliations should be centered (center-justified) on the first page. The title should be of font size 16 and bolded, the author names should be of font size 12 and bolded, and the author affiliation should be of font size 12 (regular font, neither italic nor bolded).

2. An abstract is required. The abstract should be a brief summary of the work described in the paper. It should state the computer codes, computational techniques, and applications discussed in the paper (as applicable) and should otherwise be usable by technical abstracting and indexing services. The word "Abstract" has to be placed at the left margin of the paper, and should be bolded and italic. It also should be followed by a hyphen (—) with the main text of the abstract starting on the same line.

3. All section titles have to be centered and all the title letters should be written in caps. The section titles need to be numbered using roman numbering (I. II. ….)

4. Either British English or American English spellings may be used, provided that each word is spelled consistently throughout the paper.

5. Internal consistency of references format should be maintained. As a guideline for authors, we recommend that references be given using numerical numbering in the body of the paper (with numerical listing of all references at the end of the paper). The first letter of the authors' first name should be listed followed by a period, which in turn, followed by the authors' complete last name. Use a coma (,) to separate between the authors' names. Titles of papers or articles should be in quotation marks (" "), followed by the title of journal, which should be in italic font. The journal volume (vol.), issue number (no.), page numbering (pp.), month and year of publication should come after the journal title in the sequence listed here.

6. Internal consistency shall also be maintained for other elements of style, such as equation numbering. Equation numbers should be placed in parentheses at the right column margin. All symbols in any equation have to be defined before the equation appears or right immediately following the equation.

7. The use of SI units is strongly encouraged. English units may be used as secondary units (in parentheses).

8. Figures and tables should be formatted appropriately (centered within the column, side-by-side, etc.) on the page such that the presented data appears close to and after it is being referenced in the text. When including figures and tables, all care should be taken so that they will appear appropriately when printed in black and white. For better visibility of paper on computer screen, it is good to make color figures with different line styles for figures with multiple curves. Colors should also be tested to insure their ability to be distinguished after black and white printing. Avoid the use of large symbols with curves in a figure. It is always better to use different line styles such as solid, dotted, dashed, etc.

9. A figure caption should be located directly beneath the corresponding figure, and should be fully justified.

10. The intent and meaning of all text must be clear. For authors who are not masters of the English language, the ACES Editorial Staff will provide assistance with grammar (subject to clarity of intent and meaning). However, this may delay the scheduled publication date.

11. Unused space should be minimized. Sections and subsections should not normally begin on a new page.

ACES reserves the right to edit any uploaded material, however, this is not generally done. It is the author(s) responsibility to provide acceptable camera-ready files in pdf and MSWord formats. Incompatible or incomplete files will not be processed for publication, and authors will be requested to re-upload a revised acceptable version.

COPYRIGHTS AND RELEASES

Each primary author must execute the online copyright form and obtain a release from his/her organization vesting the copyright with ACES. Both the author(s) and affiliated organization(s) are allowed to use the copyrighted material freely for their own private purposes.

Permission is granted to quote short passages and reproduce figures and tables from and ACES Journal issue provided the source is cited. Copies of ACES Journal articles may be made in accordance with usage permitted by Sections 107 or 108 of the U.S. Copyright Law. This consent does not extend to other kinds of copying, such as for general distribution, for advertising or promotional purposes, for creating new collective works, or for resale. The reproduction of multiple copies and the use of articles or extracts for commercial purposes require the consent of the author and specific permission from ACES. Institutional members are allowed to copy any ACES Journal issue for their internal distribution only.

PUBLICATION CHARGES

All authors are allowed for 8 printed pages per paper without charge. Mandatory page charges of $75 a page apply to all pages in excess of 8 printed pages. Authors are entitled to one, free of charge, copy of the printed journal issue in which their paper was published. Additional reprints are available for $ 50. Requests for additional re-prints should be submitted to the managing editor or ACES Secretary.

Corresponding author is required to complete the online form for the over page charge payment right after the initial acceptance of the paper is conveyed to the corresponding author by email.

ACES Journal is abstracted in INSPEC, in Engineering Index, DTIC, Science Citation Index Expanded, the Research Alert, and to Current Contents/Engineering, Computing & Technology.